Thesis Title: Stirring and bubbling mechanisms in a closed system for microalgae cultivation

Name : Lau Zhi Lin
Supervisor : Dr. Yap Yee Jiun
Co-Supervisor : Prof. Ir. Ts. Dr. Show Pau Loke
Department : Chemical and Environmental Engineering

Table of Contents

Abstract

The increased demand for microalgae in various industries, from bio-based to healthcare products, has attracted interest in creating a new hybrid cultivation system. Current cultivation systems apply bubbling or waterflow to create fluid turbulence and improve microalgae growth. It is understood that a specific rate of stirring motion exerts stress on microalgal cells, increasing the reactive oxygen species (ROS) levels, which could damage cells. However, some positive hormetic responses due to microalgae's defensive mechanisms have promoted growth. Combining both mechanisms within a single cultivation system may help to double the growth-promoting effect on microalgae. Moreover, including stirring mechanisms within the cultivation system enhances the microalgae's growth. It is worthwhile to study the threshold value of the stirring speed and bubbling rate without damaging the microalgal cell. The biomass, protein, and carbohydrate contents are optimum (4.335 g/L, 0.575mg/mg, and 0.117 mg/mg, respectively) when the stirring speed is 360 rpm under a constant bubbling rate. On the other hand, the optimum bubbling rate was determined when the bubbling rate was 15 v/v% of the cultivation system (1L), which was 150 cc/min. The biomass, protein and carbohydrate content concentrations are 5.229 g/L, 0.577 mg/mg, and 0.087 mg/mg, respectively. A mathematical model is synthesised better to represent the relationship between both mechanisms and microalgae growth. SEM imaging of microalgal cells at different stirring speeds showed that increased stirring speed from 0 to 420 rpm contributed to cell disruption. The cell damage was most severe at a stirring speed of 420 rpm, indicating that a higher mechanical stress acted on the cell. The upscaling of the microalgae cultivation system from 1 L of a laboratory-scale photobioreactor to 5 L of an upscaled photobioreactor showed eminent success, where the biomass was able to reach approximately 5 times the biomass weight of a laboratory-scale photobioreactor (5.283 g/L to 27.860 g/L). The upscaled cultivation stirring and bubbling rates were set at a rounded value of 350 and 400 rpm, and 15 % of the total volume of the cultivation system, respectively, as determined from previous experiments. A study on the possible inclusion of machine learning (ML) was conducted using different methods to address high-level problems such as salinity, temperature, and nutrient concentrations. The usefulness and feasibility of ML in microalgae cultivation were discussed and elaborated on, along with its potential utilisation in the industry. A discussion on the use of the optimal stirring rate and bubbling rate in a closed system was presented, together with the importance of a closed system in an automated system with machine learning. The final goal of these experiments was to study the feasibility of a closed system with stirring and bubbling automated by machine learning.

CHAPTER 1

INTRODUCTION

1. Introduction

Microalgae are microscopic unicellular organisms that form the basis of the trophic chains in water. They can grow in various environments, such as open (open ponds) and closed systems, ranging from freshwater to seawater, including landfills. The ability of microalgae to grow in different environments reduces competition between them and other plants that require specific environments. It is estimated that more than 25,000 species of microalgae are currently isolated and identified (Vale *et al.*, 2020). Microalgae perform photosynthesis to convert carbon dioxide (CO_2) into oxygen (O_2) for the aquatic system in freshwater and seawater.

They can also accumulate and produce high-value compounds like lipids, carbohydrates, and proteins. Microalgae can accumulate high concentration of lipids, which favours biodiesel production. (Vale *et al.*, 2020). The fatty acids in microalgal biomass are extracted and converted into biodiesel. Microalgal biomass-based biodiesel are generally within the standard provided by most developed countries (Vale *et al.*, 2020). In addition, the residues from the extracted biomass could be further monetised by converting them into bio-oil, bio-fuel, ethanol and methane. In recent years, microalgae have also been considered vital food crops for humans, as the demand for terrestrial food crops is very high. They can excrete essential compounds such as vitamins, amino acids and polypeptides. The richness of essential vitamins and minerals such as vitamin A, B1, B2, B6, B12, C and E, potassium, iron, magnesium, calcium and iodine enables the use of microalgae in the health industry (Cheng et al., 2019; Koyande et al., 2019; Liu et al., 2020). In addition, these nutrients can be used together with bioactive compounds such as antioxidants and pigments, such as chlorophyll for the synthesis of nanoparticles (NPs) (Stephen *et al.*, 2019).

Both photosynthetic activities and efficiency generally determine the growth and content of essential compounds in microalgae. An increase in photosynthetic activities indicates that the alga can produce enough energy to synthesise essential compounds and promote growth. On the other hand, photosynthetic efficiency is understood as the "smoothness" of the photosynthetic process with fewer or no obstacles. An increase in efficiency would allow higher growth of microalgae. Both parameters are determined by the main components of the photosynthetic process, namely light absorption and carbon dioxide (CO_2). The currently existing cultivation systems usually use various mechanisms to create turbulence in the system so that more sunlight can penetrate. For example, in ponds with flow-through channels, a racetrack-like structure is used to generate turbulence through water flow, while the bubble-column photobioreactor (PBR) and air-lift PBR use bubble formation to create a similar phenomenon (Xu *et al.*, 2009). The high energy consumption to generate agitation in PBRs has meant that these systems can only be cultivated on a laboratory scale (Najjar and Abu-Shamleh, 2020). Incorporating agitation into the photobioreactor (PBR) would allow the microalgae suspension to be more uniformly dispersed, increasing exposure to the light source. Increasing the bubbling rate would also result in better retention of the microalgae in the system, which in turn creates better opportunities for mass transfer into the microalgae cells (Tao *et al.*, 2019). The stirred-tank PBR is one of the existing PBRs that involves both stirring and bubbling within a system. However, these PBRS are generally used on a lab scale with very low speed stirring between 100 and 700 revolutions per minute (rpm).

It is interesting and worthwhile to determine the possible threshold value for the upper limit of the stirring speed without damaging the microalgae cells and promoting them simultaneously. The interaction between the bubble and the stirring mechanisms was investigated to determine if there is a synergy between the two mechanisms. In addition, the possibility of combining the cultivation and extraction phases in a single system, where the stirring speed could be increased to produce similar mechanisms to the centrifugation process, was investigated.

CHAPTER 2

RESEARCH OBJECTIVES AND PLANNING

2. Research Objectives and Planning

Current existing systems do not apply both bubbling and stirring mechanisms in microalgae cultivation. The high energy consumption of stirring has limited the possibility of combining both mechanisms in commercial systems and can only be implemented in laboratory-scale systems. In laboratory-scale microalgae cultivation systems, the stirring mechanisms are generally set to a lower speed, which is sufficient to cause microalgae suspension dispersion. Therefore, the synergies between the bubbling rate and the stirring speed must be considered before commercialising the system. The overall aim of this research is to investigate the feasibility of involving bubbling and stirring mechanisms in the cultivation process of microalgae. The main objective of this study is to determine the optimal bubbling rate and stirring speed to promote microalgae growth. The study also aims to determine the potential flux of microalgae growth in a bubbling and stirring system.

The specific objectives of the research study include:

1. To determine the effect of both bubbling and stirring mechanisms on the microalgal growth
2. To identify the shear effects on microalgae cell disruption due to stirring mechanisms
3. To develop mathematical modelling for microalgal growth, focusing on both bubbling and stirring mechanisms
4. To develop and design an upscaled photobioreactor (PBR) for microalgae cultivation
5. To optimise both bubbling and stirring mechanisms and to validate the mathematical modelling developed.

CHAPTER 3
LITERATURE REVIEW

3. Literature Review

3.1 Bubbling mechanism in microalgae cultivation

Photosynthesis is a process that requires carbon dioxide (CO_2) and light energy, converting them into oxygen (O_2) and chemical energy for microalgal metabolisms. In other words, microalgae growth would be almost impossible without the additional supply of CO_2. CO_2 gas is usually fed into the PBR in the form of gas bubbles through air diffusers or openings (Ding *et al.*, 2016). Mass transfer between bubbles and microalgal cells occurs when they are in contact. Thus, the interaction between bubbles and microalgae determines the mass transfer between them and indirectly affects the growth of microalgae. Several factors influence the intensity of the interaction between CO_2 gas bubbles and microalgae.

3.1.1 Superficial bubble velocity and gas hold-up

The superficial gas velocity is defined as the speed at which a fluid moves through a medium, where CO_2 and air are the fluid and the microalgae solution is the medium. The superficial gas velocity, U_g can be determined by dividing the volumetric flow rate of the supplied gas by the diameter. A different degree of gas retention of the bubble within the column means that the possibility of mass transfer between CO_2 in the bubbles and the microalgae cell is greater. However, several studies have shown that the bubbles react differently at specific superficial bubble velocity ranges. Ojha (2016) reports that the bubbles have a higher tendency to detach at the top of the column when the superficial gas velocities drop below 1.0 cm/s. Once the superficial gas velocities are above 1.0 cm/s, the velocity of the liquid circulation reaches its threshold value, allowing them to trap the bubble in the system. This leads to higher gas retention and thus to better mass transfer between the CO_2 in the bubbles and the microalgae cells. In addition, Mubarak et al. (2019) reported that when the superficial gas velocity increases, the gas retention for the bubbles also increases. The increased superficial gas velocity intensifies fluid turbulence and creates a balance between bubble coalescence and breakup while keeping the bubbles in smaller and uniform sizes (Tao *et al.*, 2019). This increases the surface area that comes into contact with the microalgae cells and promotes mass transfer. This increases the CO_2 intake by the microalgal cell for photosynthetic activities, promoting its growth.

3.2 Centrifugation mechanism in microalgae cultivation

Centrifugation is the application of centrifugal force or centripetal force to separate solutes from the solution inwards or outwards. Centrifugation could therefore be considered stirring as it applies similar principles, but only at high revolutions per minute (rpm). Low speed stirring is generally used in some PBRs to allow even distribution of light, nutrients and microalgae during the cultivation phase. Centrifugation or high-speed stirring is commonly used in other phases, such as microalgae extraction.

3.2.1 Low speed stirring on microalgae cultivation

In PBRs, stirring is carried out at low speed, usually between 100-700 rpm. The stirring mechanisms allow a better distribution of nutrients within the microalgae culture. The stirring mechanisms allow for better dispersion of the nutrient solution. This enables a longer contact time between the microalgae cells and the nutrient compounds, which increases the uptake of the nutrients by the microalgae. This promotes the growth of the microalgae through increased photosynthetic activity. In addition, low-speed stirring creates a vortex that leads to the circulation of microalgae within the PBR (de la Noüe *et al.*, 1984; Dolganyuk *et al.*, 2020; Isiya and Sani, 2020). The light-dark cycle of microalgae includes the periods when they are exposed to light and when they are protected from light. Since most of the energy for microalgae metabolism is based on photosynthesis, light energy is essential for microalgae growth. The circulation of microalgae allows them to be better exposed to light emitted either from natural sources (sunlight) or from artificial sources (LED light, etc.). The light-dark cycle would be altered so that the microalgae are exposed to light longer within a fixed cycle.

Furthermore, the inclusion of stirring mechanisms would exert a certain degree of mechanical stress on the microalgae cell. This would then lead to an increased secretion of reactive oxygen species (ROS), which would cause irreversible damage to the intracellular organelles. Finally, the microalgae defence mechanism triggers an increased production of superoxide dismutase (SOD) and catalase (CAT) to alleviate the stress caused by ROS (Liu *et al.*, 2011; Hashemi *et al.*, 2014). However, some studies show that a certain level of ROS stress would trigger a hormetic response in microalgae that promotes cell growth (Kim, Agca and Agca, 2013; Agathokleous *et al.*, 2019). This hormetic response generally shows positive effects at low ROS levels, where the impact of defence mechanisms is minimal.

3.2.2 High speed stirring/centrifugation on microalgae cultivation

Apart from what was mentioned in section 3.2.1, it is worth determining the upper limit or threshold of agitation speed at which the microalgae cells are not damaged. Centrifugation is commonly used in the extraction phase, where high speed stirring would break the cell wall and release the essential compounds in the microalgae. The centrifugal force pulls the cell wall outwards, exerting physical pressure on the cell wall. Damage to the cell wall would cause the cell wall to loosen and rupture, releasing the inner contents of the microalgae. The maximum limit for centrifuge speed is mainly unknown, although its effects on promoting microalgae growth are known, even with possible cell loosening. Currently, no research suggests that centrifugation or high speed stirring would eventually promote microalgae growth. However, more detailed studies can be carried out on a laboratory scale before potential commercialisation.

3.3 Combination of both bubbling and stirring in a single microalgae cultivation system

Most of the commercially used systems for the cultivation of microalgae include open field cultivation systems and closed cultivation systems. The most common open-air cultivation systems are the raceway and circular ponds. These systems generally use water currents to create a turbulent flow, allow better sunlight exposure and control the temperature. On the other hand, closed cultivation systems consist of tubular PBRs, flat plate PBRs, airlift PBRs and bubble column PBRs. Tubular PBRs are usually long and have a small diameter, while flat plate PBRs consist of thin and flat plates, with both types of PBRs achieving better solar irradiation by increasing the surface area to volume ratio. Both airlift PBRs and bubble column PBRs use bubble mechanisms to create turbulence to achieve a similar goal in open-air cultivation systems. It is evident that the currently existing cultivation systems usually achieve greater light exposure either through a high surface-to-volume ratio, bubbling and water flow-induced turbulence. The high energy consumption of agitation mechanisms has stalled interest in their use in existing cultivation systems (Najjar and Abu-Shamleh, 2020). It is believed that including a stirrer or centrifuge that can operate at both high and low speeds is useful, as both the cultivation and extraction phases can be combined in a single system. However, if both stages can be performed at a lower stirring speed, the feasibility of combining bubbling and stirring in a single system, such as a stirred tank reactor, can be further investigated. Based on the previous studies by Tao (2019) on the bubbling mechanism and Lamm's equation on the stirring/centrifugation mechanism, a mathematical model can be established.

3.4. Interaction between nanomaterial-microalgae

The following is a paper published under same project; thus, it is quoted under Lau et al. (2022a). It is understood that different types of nanomaterial such as carbon-based nanomaterials (CNMs), Metal oxide-based nanomaterials (MONMs) and noble metal-based nanomaterials (NMNMs) show different interactions with microalgae. These interactions include internalisation of nanomaterials (NMs) through direct penetration and membrane permeability alteration, NMs binding on microalgae leading to agglomerate formation and subsequent shading effect. These interactions would both directly and indirectly impose irreversible effect on microalgae itself. In general, the invasion of NMs into microalgae would trigger the defense mechanisms to counter the impact.

3.4.1 Positive impact by nanomaterial-microalgae interaction

Microalgae growth

The microalgae-NM interactions would cause oxidation stress upon the microalgae cell, increasing the ROS level. Thus, microalgae will then trigger its defense mechanism by secreting more antioxidant enzymes such as SOD and CAT to relieve the oxidation stress. Moreover, due to the interactions, microalgae cell tends to secrete more natural organic matter (NOM) in the form of extracellular polymeric substance (EPS) to form a protective layer from further microalgae-NM interactions (Chen *et al.*, 2019a). These phenomena are similar to 'fight-or-flight' mechanisms, where antioxidant enzymes and EPS secretions serve as the 'adrenaline rush' for microalgae cell which cause hormetic impact on microalgae growth. Microalgae-NM interactions is known to assist in increasing the chlorophyll content which in return provide increased photosynthetic activities, promoting microalgae growth. Even though there is insufficient literature which supports the possibility of hormetic response by microalgae, however, the hormetic responses are only valid when microalgae are exposed to low NM concentration. Thus, there is always a threshold value for different types of NM. For example, titanium dioxide (TiO_2-NM), silver (AgNM) and platinum (PtNM) would stimulate microalgal growth through hormetic responses at concentration of 1-10 mg/L, 1 mg/L and 1-15 mg/L respectively (Książyk *et al.*, 2015; Xia *et al.*, 2015). Interactions between NMs and microalgae generally cause a hormesis effect resulting in possible positive stimulation at low NM concentration (< 50 mg/L) (Agathokleous *et al.*, 2019). It is understood that the growth is stimulated at low NM concentration and growth inhibition starts as the concentration of the NM increases. Both studies have proven that carbon-based NMs improve microalgae growth by increasing the light absorption spectrum, thereby promoting photosynthesis (Giraldo *et al.*, 2014a; Zhang *et al.*, 2018). Besides, CNT-microalgae interaction show virtually no effect on cell growth as growth inhibition only occurs at a high CNT concentration (i.e. above 1 mg/L) (Rhiem *et al.*, 2015). It is reported that a low concentration of TiO_2-NM (1-10 mg/L) could stimulate microalgae growth through the promotion of total antioxidant capacity, generating higher photosynthesis rate (Xia *et al.*, 2015). Based on (Agathokleous *et al.*, 2019), these cases are due to hormesis effect by the cell defensive mechanisms against MONMs exposed on them, which in turn stimulates growth. For NMNMs case, (Książyk *et al.*, 2015) reported that not all NMNMs promotes microalgae growth. Figure 1A and B shows the cell density of microalgae when exposed to NMNMs over a period of 72 h. It is observed that PtNMs do promote microalgae growth under 5 mg/L where cell density increases beyond control set with approximately similar starting cell density. However, AgNMs do not show similar properties where its exposure to microalgae only lead to reduced cell density, indicating reduced growth.

Photosynthetic activity and efficiency

The secretion of SOD and CAT reduces the oxidation stress that were imposed on the organelles. Even though the internalisation of NMs would lead to their binding on photosynthetic organelle, inactivating their metabolisms, the effects are minimal when microalgae are exposed to low NM concentration. The EPS layer formed prevents the agglomeration of microalgae-NM complex and direct binding of NMs onto the cell membrane. This reduces the impact by the shading effect by allowing light to penetrate into microalgae allowing photosynthetic activities to be performed. The 'adrenaline rush' by the cell defense mechanisms is able to provide slight increase in the photosynthetic capability and efficiency. The hormetic response by microalgae itself oversees an increase in chlorophyll content at low NM concentration. For example, (Du *et al.*, 2016) reported that even at low reduced graphene oxide (rGO) concentration, the reduction of *chlorophyll a* (*chl a*) and *chlorophyll b* (*chl b*) which are vital for light absorption in microalgae photosynthetic pigments do occur, indicating a decrease in photosynthetic efficiency. *Chl a* acts as the electron donor within the microalgae which supports photosynthesis while *chl b* expands the light absorption spectrum. Reduction of *chl a* with the increased rGO concentration will greatly impact the photosynthetic activities. Table 1 shows the change in chlorophyll content of microalgae after exposed to rGO.

Table 1. Chlorophyll content in microalgae when exposed to different rGO concentration (Du *et al.*, 2016)

rGO concentration (mg/L)	0	10	20	50	100
Chl a (µg 10^{-5} cell)	1.7494	1.3351	1.4153	1.0920	0.2514
Chl b (µg 10^{-5} cell)	0.5329	0.4404	0.5043	0.6289	0.1732

The interaction between MONM and microalgae shows different degrees of alteration on the photosynthetic efficiency of microalgae. Microalgae-TiO_2-NM and microalgae-CuO-NM interactions have induced the formation of *chl a* and phycobiliprotein (PBP) in photosynthetic pigments by the stimulated enhanced ROS (Melegari *et al.*, 2013a; Middepogu *et al.*, 2018a). Chlorophyll pigments in microalgae increases when exposed to low concentrations of CuO-NM and TiO_2-NM. These pigments are used for the light absorption during photosynthetic activities. Subsequently, an increase in *chl a* and PBP helps to reduce the impact by shading effect on microalgal photosynthesis. Increase in *chl a* content and PBP would greatly improve the light energy conversion into chemical energy and light absorption for the photosynthesis activities, respectively.

As reported by (Książyk *et al.*, 2015), the exposure of AgNM and PtNM on microalgae have induced the formation of *chl a* and *chl b* in photosynthetic pigments. The increase in *chl a* and *chl b* promote photosynthetic activities and subsequently microalgae growth. This improves the light absorption for photosynthesis, promoting photosynthetic activity as well as photosynthetic efficiency. However, this is only valid for low NMNM concentration exposure to microalgae, for example 1-15 mg/L for PtNM and 1 mg/L for AgNM. This is mainly due to the hormetic response by microalgae where their defensive mechanisms induced cell growth. Figure 1C and D shows the effect of microalgae-NMNM interactions on the chlorophyll content.

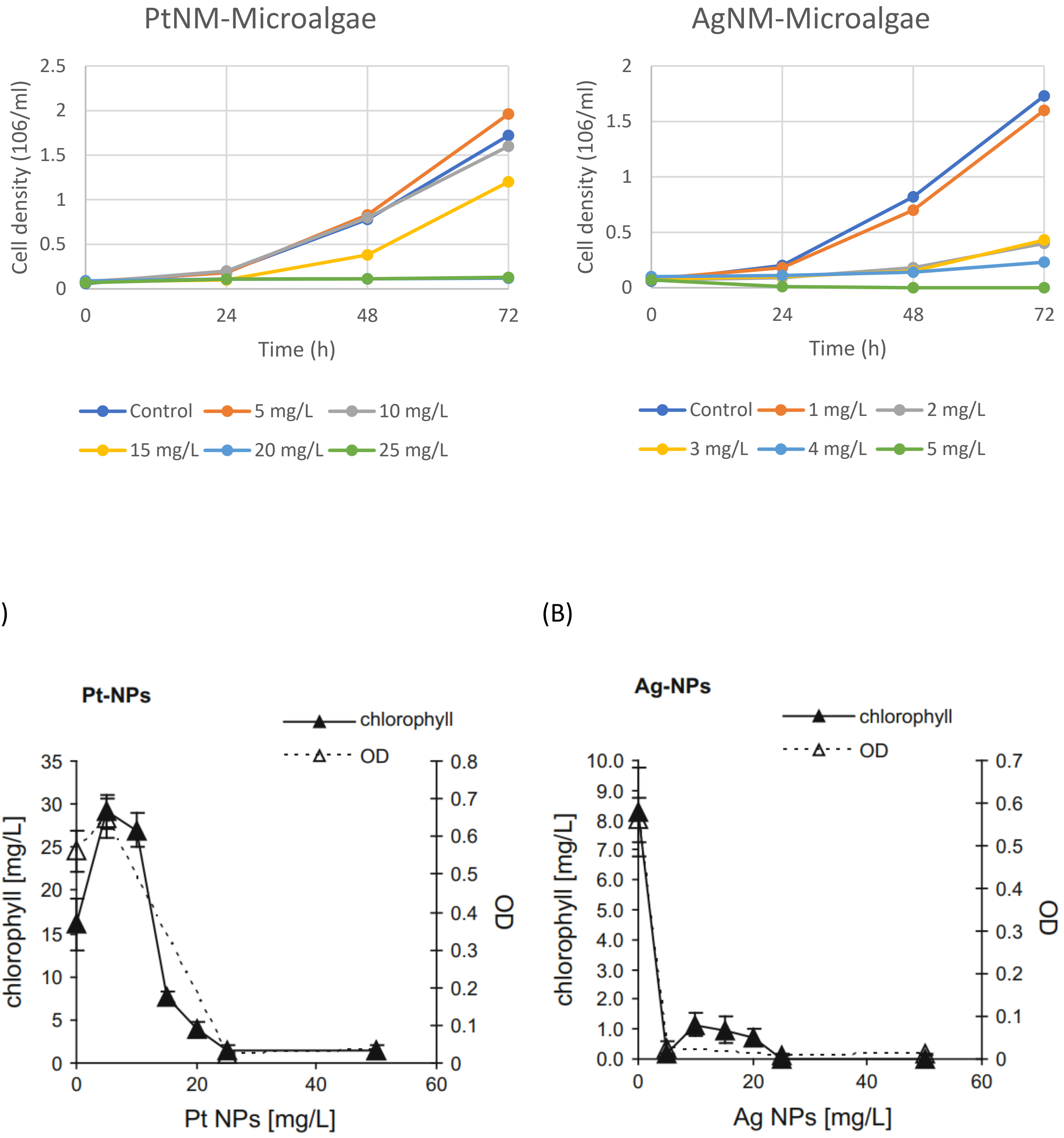

(A)

(B)

(C)

(D)

Figure 1. Microalgae cell density exposed to different (A) PtNM and (B) AgNM concentration. Effect of interaction between (C) PtNM and (D) AgNM with microalgae on chlorophyll content. Reproduced with permission from (Książyk *et al.*, 2015) from Springer Nature

However, (Li *et al.*, 2020) reported that gold nanomaterial (AuNM) binding on *Chlorella zofingiensis* at concentration of 24-26 mg/L does not impair existing photosystem compare to control system where chlorophyll pigments are still intact. This indicates that AuNM concentration below the threshold value would never inhibit nor promotes the photosynthetic ability of microalgae. Furthermore, this explanation is further proven to be in agreement with earlier works (Torres, Diz and Lagorio, 2018) involving the microalgae-AuNM interactions with no apparent increase in photosynthetic activities at low concentration of AuNM.

3.4.2 Negative impact by nanomaterial-microalgae interaction

Microalgae growth

As the NM concentration exposed to microalgae increases, the hormetic response is slowly overcome by the NM toxicity. Over-accumulation of ROS within the cell causes irreversible damage on the photosynthetic organelles. Internalised NMs would attach themselves on the photosynthetic protein and inactivating them, halting the homeostasis within the cell. This would prevent the routine metabolisms within the cell, lowering the microalgae growth rate, or in severe cases, cell death. The down-regulation of electron transport chain and reaction center protein within photosystem II (PSII) would lead to slowed and reduced synthesis of adenosine triphosphate (ATP) which is the main source of energy for cell metabolisms (Chen *et al.*, 2019b). This would reduce the possibility of accumulation of carbon dioxide (CO_2) and conversion of light energy to photosynthetic electrons. For instance, the gene transcription for cell division would also been down-regulated, preventing the cell growth. Furthermore, several studies reported that the NMs do bind on microalgae cell membrane, altering the permeability, allowing them to enter the cell. The alterations do have irreversible effects as certain nutrients are forbidden to enter the cell. This would lead to possible nutrients depletion and eventually cell death. Based on previous studies, all CNMs showed different degrees of growth inhibition under different conditions of NMs (Schwab *et al.*, 2011). Agglomerated CNT (3 day old) causes growth inhibition on *C. vulgaris* up to 61 ± 7 % at a concentration of 50 mg/L, and 75 ± 21 % for well-dispersed CNT (freshly prepared) at a concentration of 5.5 mg/L. On the other hand, oxidised CNT shows 50 % reduction in growth inhibition. This is mainly due to the direct interaction between CNT and microalgae which causes possible membrane damage through direct penetration and indirect alteration of membrane wall leading to growth inhibition (Zhao *et al.*, 2017). Besides, graphitised nanodiamond (GND) shows a large decrease in cell number of *C. pyrenoidosa,*72 % with the increase of GND from 0 to 50 mg/L, indicating significant growth inhibitory effect (Zhang *et al.*, 2020). Based on findings, it can be seen that growth inhibition on microalgae with CNT is caused by the combination between agglomeration of microalgae-CNT and shading effect (Wei *et al.*, 2010; Schwab *et al.*, 2011). Agglomeration of microalgae-CNT results in minimal light exposure, subsequently inhibiting the cell growth. Microalgae growth is shown as a function of factors such as the light attenuation and turbidity (Cheah *et al.*, 2020), including the criteria for continued increase in microalgae growth based on these factors. Moreover, internalisation of CNT NPs in microalgae have not induced any growth inhibitory effect which are in agreement with previous studies (Kwok *et al.*, 2010; Wei *et al.*, 2010; Schwab *et al.*, 2011). Furthermore, it was reported that growth inhibition on *C. Pyrenoidosa* for graphene oxide (GO) NM, rGO NM and multilayer graphene (MG) NM are mainly due to graphene family based NM (GFNM) agglomeration with microalgae, microalgae membrane damage and nutrient depletion inducing indirect toxicity upon the microalgae (Zhao *et al.*, 2017). Figure 2 shows reduction in suspended algae in rGO and MG, indicating formation of larger aggregates.

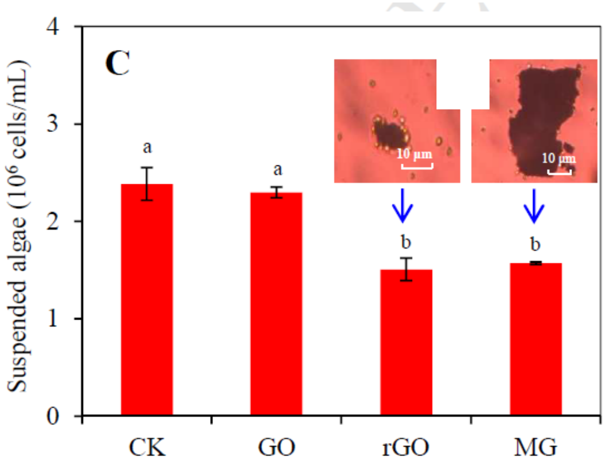

Figure 2. Quantity of suspended algae after exposed to carbon-based NM. Reproduced with permission from (Zhao *et al.*, 2017) from Elsevier.

In addition to these factors, the shading effect on microalgae with GO also serves to inhibit the microalgae growth. The stronger hydrophobicity of rGO and MG than GO proved to be playing a vital role as the microalgae-GFNM agglomerates tend to form larger agglomerates, causing them to settle at the bottom and resulting in a weaker shading effect on the microalgae. On the other hand, microalgae-GO agglomeration has a low tendency to form larger agglomeration resulting in more significant shading impact, leading to a greater growth inhibition, which is further supported by (Schwab *et al.*, 2011). All three GFNMs cause microalgae membrane damage through direct membrane damage and oxidation stress-induced lipid peroxidation. Results from (Zhao *et al.*, 2017) showed that there is direct penetration by all three GFNMs resulting in physical damage on the microalgae membranes. Figure 3 shows SEM results of penetration by rGO and MG on the microalgae membrane and flow cytometry of membrane damage for carbon-based NMs.

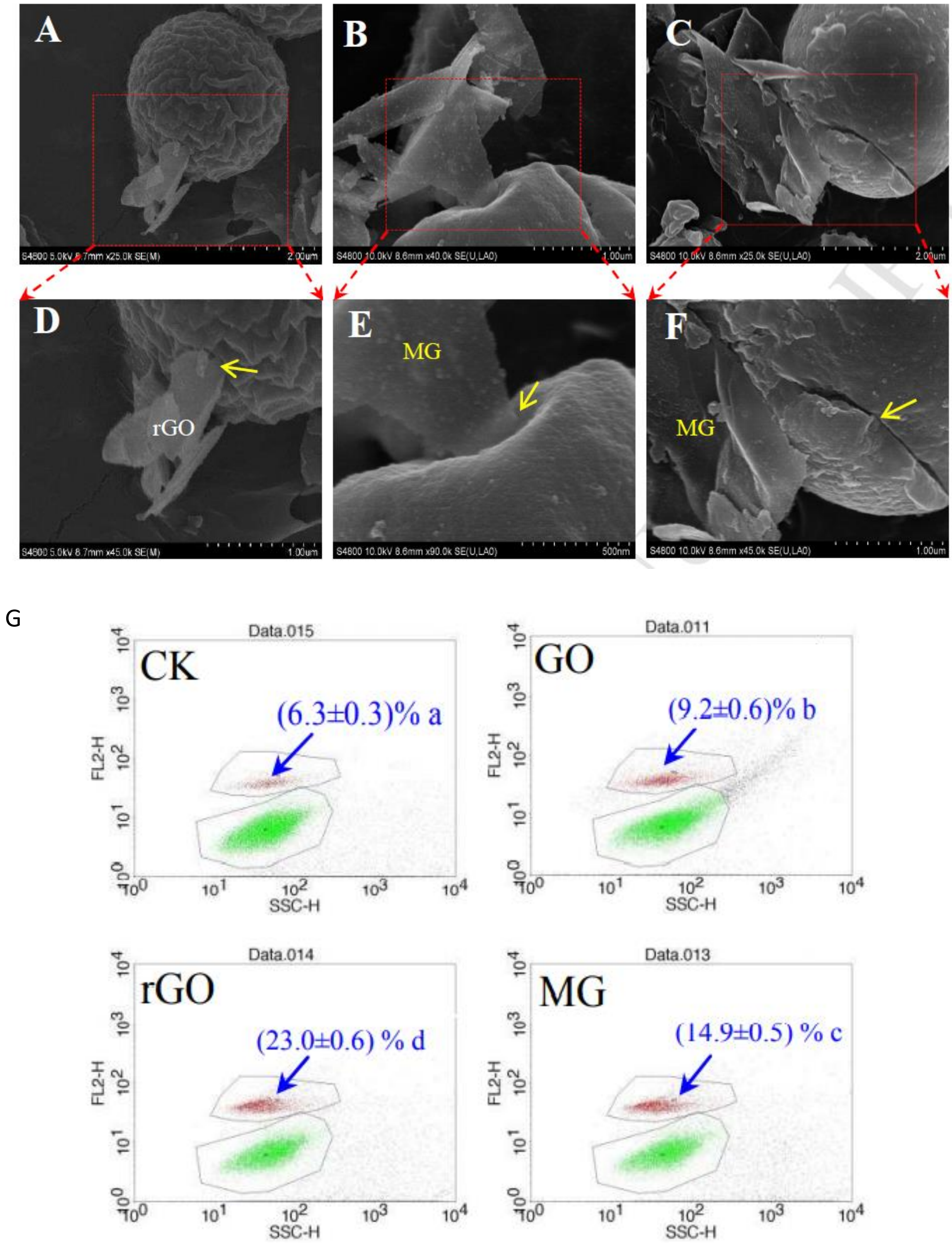

Figure 3. SEM images of (A) rGO, (B) & (C) MG penetration on algae cell. (D), (E) & (F) is the enlarged image for (A), (B) & (C), respectively. (G) Flow cytometry results of microalgae membrane damage after exposed to carbon-based NM where green areas referred to intact

cells and red areas referred as impaired cells. (CK refers to CNT). Reproduced with permission from (Zhao *et al.*, 2017) from Elsevier.

These results are supported by previous studies by (Li *et al.*, 2013) which suggest possible physical penetration by sharp edge of MG on cell membranes. Besides, the exposure of the GFNMs to microalgae plays a role in increasing the intercellular ROS level, which are consistent with findings by (Liu *et al.*, 2011; Hashemi *et al.*, 2014) where carbon-based NMs tend to interact with membranes including animal cell, bacteria and microalgae altering the permeability and hence inducing ROS (Chan *et al.*, 2022). Malondialdehye (MDA) secreted by microalgae for lipid peroxidation in response to GFNMs exposure, resulting in an increase in membrane pores through oxidation of polyunsaturated fatty acid. This will then damage the cell membrane and subsequently inhibiting microalgae growth. GO, rGO and MG are capable to adsorb both nitrogen (N) in the form of nitrate ions and phosphorus (P) in the form of hydrogen phosphate ions which are vital for the synthesis of lipid, protein and carbohydrates for microalgae growth. This will cause nutrient depletion for microalgae leading to growth inhibition.

On the other hand, the exposure of ZnO-NM and Fe_2O_3-NM on microalgae did not promote any microalgae growth and will only cause growth inhibitory effect. The high reactivity of Zn and Fe ions coupled with the higher tendency of metallic ions internalisation within the cell through membrane alteration lead to growth inhibition even at low concentration, making any growth promotion insignificant. For example, no inhibitory effect was detected on *O. tauri* and *Nannochloris* by both ZnO-NMs and Fe_2O_3-NMs whereas *M. commoda* showed a growth inhibitory effect (Genevière *et al.*, 2020). This is mainly due to concentration of extracellular polymeric substances secreted by microalgae where both *O.*

tauri and *Nannochloris* produced are sufficient to enhance the aggregation of NPs, reducing the interaction between them and microalgae, thereby nullifying the inhibitory effect. However, this is only valid for ZnO-NM and Fe_2O_3-NM, whereas, for TiO_2-NM and CuO-NM cases, low NMs concentration would promote microalgae growth (Melegari *et al.*, 2013b; Middepogu *et al.*, 2018b). It is mentioned that when the MONM concentration increase, its toxicity towards microalgae would increase leading to growth inhibition. For example, the exposure of TiO_2-NM to microalgae would lead to growth inhibition due to membrane damages, plasmolysis and internalisation of TiO_2-NM in microalgae (Middepogu *et al.*, 2018a). Figure 4 shows interaction between microalgae and different concentration of TiO_2-NMs by using scanning electron microscopy (SEM) and transmission electron microscopy (TEM) images.

The adsorption of TiO_2-NMs on the cell membrane caused the formation of large agglomerate between TiO_2-NMs and microalgae. The shading effect will then take place where light transmittance into the cell is reduced, resulting in lower photosynthetic activity and subsequently inhibiting cell growth. However, this effect is insignificant on growth inhibition for microalgae-TiO_2-NM, microalgae-CuO-NM and microalgae-Fe_2O_3-NM interactions (Lee and An, 2013; Melegari *et al.*, 2013a; Hazeem *et al.*, 2015a). Moreover, microalgae-TiO_2-NM interaction would induce ROS and subsequently causes membrane damage and plasmolysis. This effect, coupled with internalisation of TiO_2-NM, will result in the impairment of the photosynthetic electron transport system, reducing photosynthetic activity and hence inhibiting cell growth. On the other hand, increasing in concentration of ZnO-NMs exposed to microalgae would also induce growth inhibition for microalgae (Lee and An, 2013; Hou *et al.*, 2018). Similar to TiO_2-NM, microalgae-ZnO-NM, microalgae-CuO-NM and microalgae-Fe_2O_3-NM interactions do induce ROS, subsequently causing membrane damage leading to growth inhibition when ROS level exceeds the capacity of the stimulated cell defensive mechanism (eg. Inducing SOD and CAT to counter ROS) (Lee and An, 2013; Melegari *et al.*, 2013a; Saxena, Sangela and Harish, 2020). In extreme cases, this consequence would also result in cell death. The leaching of zinc ions (Zn^{2+}) from the ZnO-NM causes excessive Zn^{2+} ions to compete with manganese ions (Mn^{2+}) uptake by microalgae (Lee and An, 2013). Since Mn^{2+} ions serve as vital nutrient for microalgae, the induced deficiency causes nutrient depletion for intercellular activities before resulting in growth inhibition. Unlike other microalgae-MONM, internalisation of copper ions (Cu^{2+}) from CuO-NM and iron ions (Fe^{2+}) from Fe_2O_3-NM into microalgae through the endocytosis process would lead to these ions binding on intracelluar organelles, affecting the cell metabolism activities (Melegari *et al.*, 2013a; Hazeem *et al.*, 2015b). This would then induce toxicity on microalgae and causing growth inhibition.

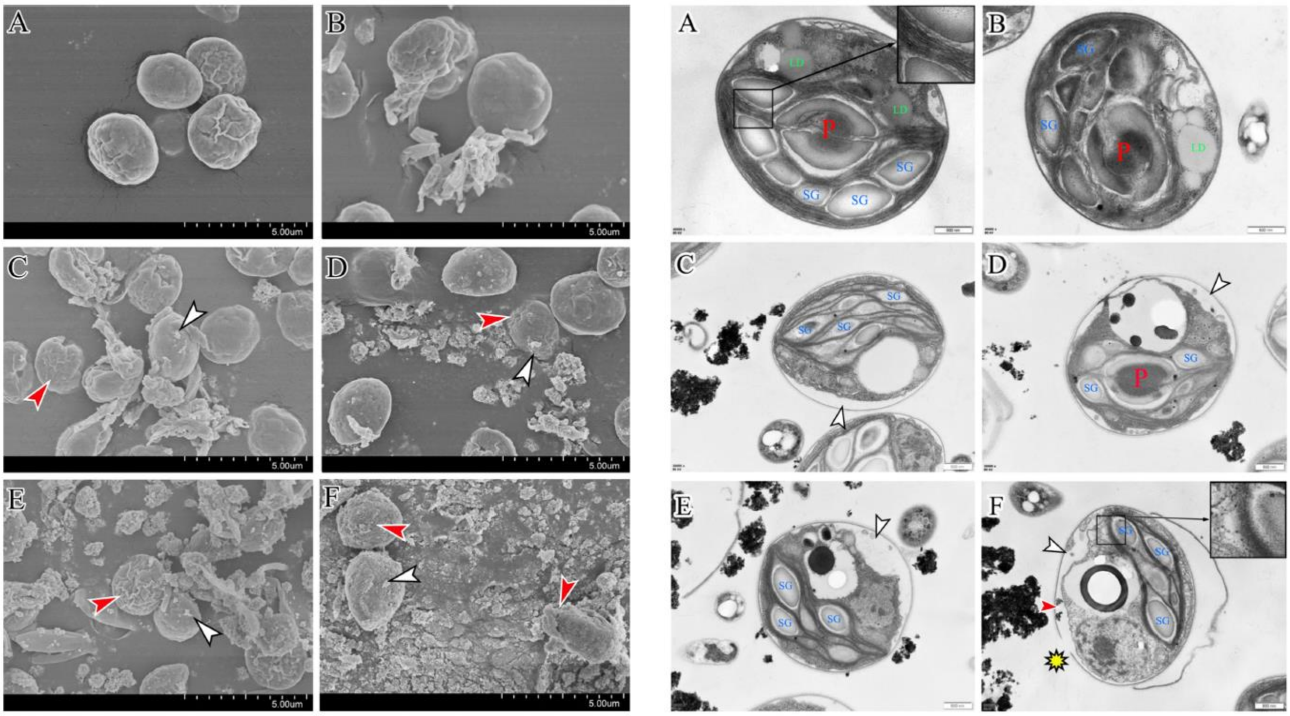

(I) (II)

Figure 4. (I) SEM & (II) TEM images of microalgae exposed to different concentration of TiO_2-NM. (A) 0, (B) 0.1, (C) 1, (D) 5, (E) 10 & (F) 20 mg/L. (I) White arrows indicate TiO_2-NP attachment on cell wall whereas red arrows indicate membrane alteration such as surface disruption, shrinkage and irregularity; (II) Yellow star shows the cell wall breakage location, white arrows indicate plasmolysis and membranolysis whereas red arrow indicates internalisation of TiO_2 in microalgae. Reproduced with permission from (Middepogu *et al.*, 2018a) from Elsevier.

Similar to carbon-based NMs and MONMs, a higher concentration of NMNMs will inhibit microalgae growth. As reported by (Moreno-Garrido, Pérez and Blasco, 2015), the main interactions between NMNM are generally due to direct binding onto the membrane surface of microalgae. They reported that both AgNM and AuNM will be bound onto the microalgae outer membrane, altering the membrane properties and shifting the permeability, allowing more ions transport in and out of the cell. This could possibly lead to nutrient depletion, inhibiting the cell growth. Moreover, alteration of membrane permeability through binding of AgNM onto microalgae will allow more internalisation of highly toxic silver ions (Ag^+) (Książyk *et al.*, 2015; Moreno-Garrido, Pérez and Blasco, 2015; Pham, 2019). These Ag^+ ions are mainly leached from AgNM, and will cause DNA inhibition and damage. Besides, Ag^+ ions bind onto the active sites for photosynthetic enzymes and proteins, leading to impairment in photosynthetic system and subsequently growth inhibition. For example, interaction between AgNM, AuNM and PtNM and microalgae lead to the stimulation of defensive mechanisms within the cell, synthesizing SOD and CAT as antioxidant to counter the increase in ROS due to lipid peroxidation. As soon as the ROS level exceeds the limitation control by the antioxidant, the cell membrane will be damaged and plasmolysis will occur, possibly followed by cell death. Furthermore, the microalgae-AuNM interaction would lead to the aggregation of microalgae-AuNM resulting in shading effect, reducing the photosynthetic activities (Książyk *et al.*, 2015; Moreno-Garrido, Pérez and Blasco, 2015). Direct binding of both AuNM and PtNM on microalgae are also seen to be one of the factors for growth inhibition. The formation of the agglomerates would clog microalgae within the agglomerate resulting in shading effect, reducing photosynthetic activities and cell growth. Besides, silver nanomaterials (AgNM) were reported to be only adsorbed onto the external surface of microalgae but there is a lack of inhibition effect which may be due to the minimal interaction between AgNM and microalgae or the masked effect by de-novo synthesis of the enzyme by microalgae (Yue *et al.*, 2017).

Photosynthetic activity and efficiency

Photosynthetic efficiency is described as the fraction of the light source which is converted to chemical energy through photosynthesis by microalgae. Based on reports by

(Wei *et al.*, 2010; Schwab *et al.*, 2011), microalgae-CNT interactions do alter the photosynthetic activity of microalgae. The relationship between microalgae growth and photosynthesis are mathematically modelled (6) by (Cheah *et al.*, 2020).

$$A(t) = \frac{\alpha - \beta k_{bg}}{\beta k} + \left[A(0) - \frac{\alpha - \beta k_{bg}}{\beta k}\right] e^{-\beta t} \qquad (1)$$

Equation (1) is valid under zero turbidity, where A(t) is the density of microalgae at time, t, k is specific light attenuation and k_{bg} is the background turbidity. Both α and β are the factors affecting the rate of microalgae growth.

$$\alpha = \frac{\mu_{max}}{z_{max}} ln \left(\frac{H_p + I_{in}}{H_p + I_{out}}\right) (2)$$

$$\beta = h_r + D_r \quad (3)$$

where μ_{max} is maximum specific growth rate of microalgae, z_{max} is mixing depth, H_p is half-saturation photosynthesis, I_{in} is incoming light, I_{out} is outgoing light, h_r is dilution/outflow and D_r is specific maintenance (death rate). A(t) is assumed to increase with time if

$$\frac{\alpha}{\beta} > \left[A(0)k - k_{bg}\right] \quad (4)$$

whereas, A(t) decreases with time when

$$\frac{\alpha}{\beta} < \left[A(0)k - k_{bg}\right] \quad (5)$$

but saturates as $t \rightarrow \infty$.

Equation (1) proves to be important as it validates the relationship between light absorbed by chlorophyll for photosynthetic activities within the microalgae. Higher I_{out} indicates less light absorbed for photosynthetic activities, which is due to possible interruption through shading effect and agglomeration of NMs-microalgae. This would reduce light absorbance and subsequently cell growth, resulting in reduced microalgae density.

Even though the secretion of EPS around the microalgae membrane helps to reduce the NM internalisation, however, the protective effect by EPS would be overcome by the increase in NM concentration exposed to microalgae, allowing NMs penetrating through the cell wall/membrane layers. This allows them to bind on photosynthetic organelles, inhibiting them from functioning, thus lowering the photosynthetic capabilities and activities. Moreover, EPS production is a light dependent process (Babiak and Krzemińska, 2021). Thus, it means that the increase in light attenuation and absorption by microalgae would increase the EPS production. Microalgae and NMs tend to form complexes where NMs bind on the cell membrane layer. In addition, these complexes would then form larger agglomerate between them. Even though as mentioned in Section 3.3.1 that low NM concentration could induce EPS secretion as protective layer to NM invasion, however, as the NM concentration exposed to microalgae is increased, the snowballing effects of both NM binding on membrane layer and internalisation of NMs, inactivation of photosynthetic organelles, would hinder further EPS secretion making microalgae more vulnerable to NMs toxicity. Figure 6 displays *D. tertiolecta* CNT aggregation. The shading effect by microalgae-rGO interaction coupled with direct penetration of rGO into microalgae is the main reason for the reduction in photosynthetic efficiency. On the other hand, low concentration of CNTs improves microalgae photosynthetic efficiency (Giraldo *et al.*, 2014b). The internalisation of CNTs in microalgae allows wide ranges of light spectrum absorption, promoting photosynthetic activities. However, further increase in the CNT concentration causes an adverse effect on the microalgae photosynthetic system. Higher possibility for CNTs in direct contact with *D. tertiolecta* cell surface causes both membrane alteration and shading effect, which leads to photosystem II (PSII) functional cross-section reduction and increased oxidation stress, resulting in decreased microalgae photosynthetic ability (Wei *et al.*, 2010).

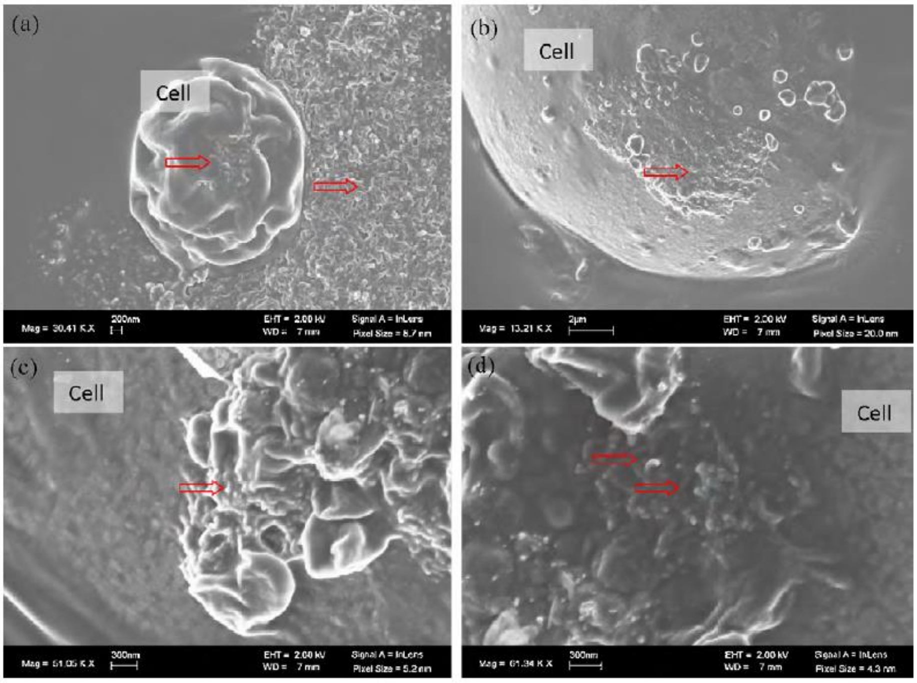

Figure 5. SEM image of formation of D. tertiolecta-CNT aggregates (a) after 2 h exposure to CNT, (b) after 28 days exposure to CNT, (c) & (d) are enlarged images for (a) & (b) respectively. Reproduced with permission from (Wei *et al.*, 2010) from Elsevier.

Table 2. Negative impacts on photosynthetic efficiency of different NMs after exposed to microalgae

Types of NM	**Impact towards photosynthetic activities**
Carbon based NM (CNM)	-Lead to possible nutrient depletion for photosynthetic organelles
Metal oxide-based NM (MONM)	-Impairs photosynthetic electron transport system
Noble metal-based NM (NMNM)	-Bind onto photosynthetic organelles, inactivating them irreversibly -Increased shading effect, lowering light attenuation.

Table 2 shows the summarised negative impact by each type of NM on photosynthetic efficiency. The photosynthetic activity of microalgae is mainly affected by the shading effect of microalgae-CNT as well as the cell wall alteration by CNT through direct contact (Schwab *et al.*, 2011). Based on (Zhao *et al.*, 2017), the superior adsorption capability of carbon-based NM such as CNT and GFNM is also one of the causes for the reduction in photosynthetic activity. Essential nutrients such as magnesium (Mg^{2+}) and calcium ions (Ca^{2+}) tend to be adsorbed onto the CNT and GFNM, leading to nutrient depletion in microalgae. Mg^{2+} ions are vital for photosynthesis and several enzymatic activities such as protein kinase and RNA polymerase whereas Ca^{2+} ions play an important role in chlorophyll synthesis. Depletion of these nutrients within microalgae would lead to reduction in photosynthesis activity and capability, resulting in reduced photosynthetic efficiency.

For MONM cases, especially for CuO-NM and TiO_2-NM, the internalisation of Cu^{2+} ions and titanium ions into microalgae would lead to the impairment of the photosynthetic electron transport system, suppressing and reducing the photosynthetic activity, resulting in reduced photosynthetic efficiency. Moreover, the high affinity of microalgae to uptake Cu^{2+} ions and Zn^{2+} ions as they serve as essential nutrients for microalgae would oversee these ions taking advantage in binding onto metalloprotein such as chlorophyll-containing protein, triggering cell defensive mechanism to counteract (Miller *et al.*, 2017). Once the mechanism reaches its limits, further binding by these ions would then reduce the availability of the active sites of these metalloprotein, especially chlorophyll-containing protein, and directly affecting the photosynthetic activities, which in turn reduces its photosynthetic efficiency.

The further increase in NMNM concentration would then be observed to drop in photosynthetic efficiency. For example, greater microalgae-AgNM would occur where the membrane permeability will be altered, allowing leached Ag^{+} ions to diffuse into the cell. Subsequently, these ions will then bind onto the active sites of photosynthetic enzymes and protein, resulting in photosynthetic system impairment (Moreno-Garrido, Pérez and Blasco, 2015). Unlike AgNM, for both AuNM and PtNM, the decrease in photosynthetic efficiency is due to the aggregation of these NM with microalgae as well as their interaction with cell wall. The aggregation of microalgae-AuNM and microalgae-PtNM would block the light transmittance into the cell, thereby lowering the photosynthetic activities (Książyk *et al.*, 2015; Moreno-Garrido, Pérez and Blasco, 2015). On the other hand, excessive ROS levels triggered by a high concentration of AuNM and PtNM would cause adverse effect when the cell defensive mechanisms could not compensate with the effect. This would subsequently cause membrane damage, nutrient depletion, followed by a reduction in photosynthetic activities and efficiency.

3.4.3 Toxicity of Nanomaterial on microalgae

Different type of NM will cause different degree of toxicity upon the microalgae. For example, toxicity of carbon-based NM are typically due to three main reasons which are shading effect, agglomeration of microalgae-NM and direct penetration on microalgae through sharp edge of NM. Compared to other types of NMs, internalisation of carbon-based NM within microalgae does not occur. This prevents direct adsorption and poisoning of NM upon the vital photosynthetic organelles within microalgae, inhibiting cell growth by halting photosynthetic activities. This reduces the toxicity of carbon-based NM compared to other types of NM.

The toxicity of NM is generally induced by an interaction between NMs and microalgae. Interactions between NMs and microalgae are commonly involving the adsorption of NM onto the membrane surface of the microalgae or direct intake and accumulation of metal ions from NM by the microalgae. The adsorption of NMs onto the membrane surface causes distorted membrane integrity and in severe cases membrane damage. Moreover, NMs adsorption causes an increase in ROS upon microalgae, triggering defensive mechanism by microalgae by inducing more antioxidant enzymes to relieve ROS. When the ROS exceeds the scavenging capacity of these antioxidant enzymes, membrane damage occurs (Genevière *et al.*, 2020). (Zhang *et al.*, 2018) reported that formation of large agglomerations between NM adsorbed microalgae cells would also lead to possible reduction in interaction between NM and microalgae. Besides, larger agglomerate of microalgae-NM would also cause reduction in photosynthetic activity of microalgae as the light transmittance to microalgae is lowered. This is because the NM surrounding the microalgae causes shading effect, thereby blocking light transmittance to the microalgae. Internalisation of accumulated ions from NM could lead to possible cytopathogenic damage and cell death (Yin *et al.*, 2020). This may negatively impact the biosynthesis of NM by microalgae reported in other works (Li *et al.*, 2011; Rahman, Kumar and Nawaz, 2019). Accumulation of NPs synthesised within the microalgae will in return inhibit microalgae growth by causing direct toxicity on intracellular organelles.

Figure 6A shows all of the possible interactions between NMs and microalgae, while Figure 5B shows that increased concentration in carbon-based NMs will lead to the increase of microalgae growth inhibition. These results are obtained by (Zhao *et al.*, 2017) under low turbidity condition and constant light attenuation. Median effective maximum concentration (EC_{50}) is the concentration of the carbon-based NM at which there is a 50 % reduction in microalgae growth. EC_{50} can be used as the indicator for the ecotoxicity of the carbon-based NM.

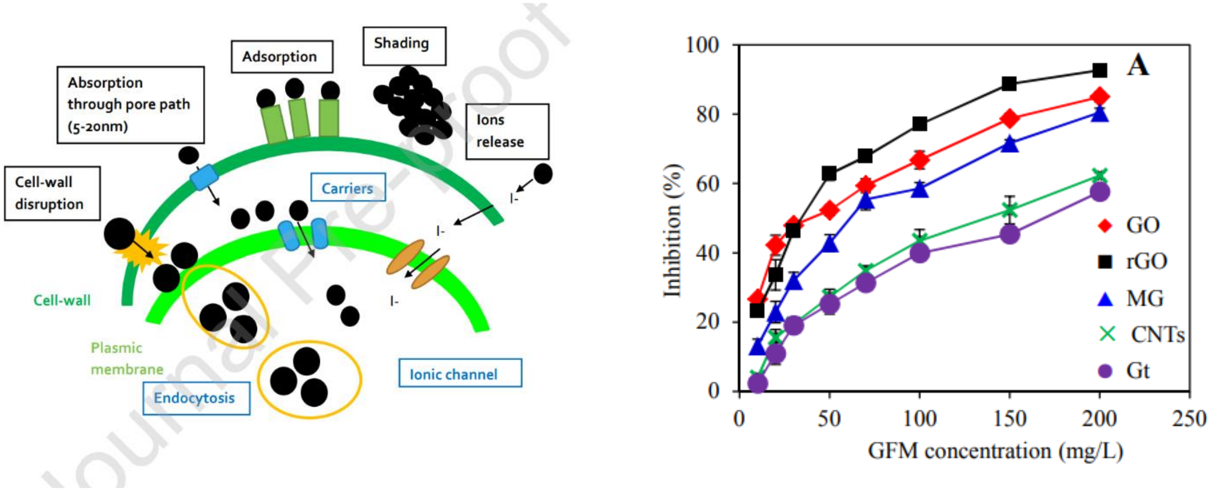

(A) (B)

Figure 6. (A) Interactions between NMs and microalgae, (B) Inhibition percentage and the corresponding carbon-based NMs concentration, Reproduced with permission from (Zhao *et al.*, 2017) and (Déniel *et al.*, 2019) from Elsevier.

Table 3. EC_{50} value of different NM after exposed to microalgae.

Type of NM	**Microalgae type**	**NM particle size (nm)**	**NM dosage (mg/L)**	**EC_{50} (mg/L)**	**Reference**
CNT	*C. pyrenoidesa*	40-60	50	137.00	(Zhao *et al.*, 2017)
	C. vulgaris	70	5.5	1.80-26.00	(Schwab *et al.*, 2011)
	P. subcapitata			20.00-36.00	
GO	*C. pyrenoidesa*	2.1	50	37.30	(Zhao *et al.*, 2017)
rGO	*C.*	1.5	50	34.00	(Zhao *et al.*,

	pyrenoidesa				2017)
MG	*C. pyrenoidesa*	5	50	62.20	(Zhao *et al.*, 2017)
CuO	*N. oculata*	10-40	5-200	116.98	(Fazelian, Yousefzadi and Movafeghi, 2020)
	C. reinhardtii	30-40	0.1-1000	150.45	(Melegari *et al.*, 2013a)
	C. pyrenoidesa	30-50	10	45.70	(Zhao *et al.*, 2016)
Fe_2O_3	*N. oculata*	20-40	5-200	202.92	(Fazelian, Yousefzadi and Movafeghi, 2020)
TiO_2	*P. subcapitata*	20-35	30-150	10-26	(Hund-Rinke and Simon, 2006; Lin, Tseng and Huang, 2015)
	D. suspicatus				
ZnO	*N. oculata*	10-30	5-200	153.72	(Fazelian, Yousefzadi

					and Movafeghi, 2020)
	P. subcapitata	20-30	0.25-1	0.5-1.5	(Bhuvaneshwari *et al.*, 2015; Fazelian, Yousefzadi and Movafeghi, 2020)
	S. *obliquus*				
AuNM	*C. reinhardtii*	10	1-2	No significant effect	(Tang *et al.*, 2017)
	S. subspicatus			1.91	
AgNM	*C. reinhardtii*	25	0-2.0	0.112	(Wang and Wang, 2014; Wang, Lv and Zhang, 2016)
	C. vulgaris	60		1	
	P. subcapitata	29-42		9.9×10^{-3}	
		10-40	1-5	1.63	(Książyk *et al.*, 2015)

PtNM	*C. reinhardtii*	1-10	10-390	173-235	(Wang and Wang, 2014)
	P. subcapitata			13-16	
		10-40	5-25	16.9	(Książyk *et al.*, 2015)

Table 3 illustrates the EC_{50} value for each type of NM. Table 3 shows that GFMs generally possess higher toxicity compared to CNTs. Lower EC_{50} values indicates that a lower concentration of NM is required to achieve 50 % growth inhibition of microalgae. It is suggested that GO possesses higher toxicity than rGO in the first 24 hours, however rGO shows increasing toxicity with time (Zhao *et al.*, 2017). The relation between exposure time and toxicity is further proven by previous research study (Liu *et al.*, 2011).

The main toxicity by MONMs is due to the capability of these NMs to enter the cell through membrane alteration where the metallic ions tend to bind onto photosynthetic organelles, preventing the normal metabolisms routines, inhibiting the cell growth. The toxicity of each MONM depends on the microalgae involved and the level of interaction. From Table 3, ZnO-NM possesses a higher toxicity when compared to other MONM as lower NM concentrations are required to achieve 50 % growth inhibition, followed by TiO_2-NM, CuO-NM and Fe_2O_3-NM. However, CuO-NM possesses higher toxicity than ZnO-NM and

Fe_2O_3-NM for *N. oculata.* This shows that NMs have different degrees of toxicity on different microalgae species. Generally, these toxicity results are in agreement with the previous studies (Fazelian, Yousefzadi and Movafeghi, 2020).The toxicity of ZnO-NM is caused by the growth inhibition through the destruction of cell antioxidant capacity, allowing a further increase in ROS level and subsequently cell plasmolysis and death. Moreover, TiO_2-NM generally induce toxicity through the decrease of *chl a* and soluble protein content where photosynthetic activities are lowered. The toxicity of TiO_2-NM is also a result of the accumulation of lipid peroxide which increases the ROS level and possible cell damage. Based on (Wang *et al.*, 2019), CuO-NM would induce toxicity through direct DNA damage of the organelle within microalgae, resulting in growth inhibition.

Based on Table 3, it is observed that AgNM is the most potent NM followed by PtNM and AuNM. (Książyk *et al.*, 2015) reported that Ag^+ ions from AgNM are the main reason for its high toxicity. Unlike Ag, Au and Pt are less reactive in their ionic form where leaching of Au and Pt ions into microalgae are not seen in recent studies (Książyk *et al.*, 2015; Moreno-Garrido, Pérez and Blasco, 2015; Torres, Diz and Lagorio, 2018). Leached Ag^+ ions tend to diffuse into microalgae and bind to the active sites of the organelle such as photosynthetic enzymes, inhibiting their activities and subsequently cell growth. For AuNM and PtNM, the toxicity are only seen to have incurred due to the aggregation with microalgae and cell wall interaction (Moreno-Garrido, Pérez and Blasco, 2015). Shading effect and alteration of membrane occur where photosynthetic capability and metabolism activities are negatively affected. In general, MONMs tend to incur highest toxicity on microalgae followed by NMNMs and CNMs.

3.4.4 Nanobionics

Nanobionics is the combination of the word ‘nano’ from nanotechnology and bionics. Bionics in general terms means the study of both functional and structural properties of biological systems serving as the model for the design of engineering systems. Therefore, nanobionics is referred as the integration of nanotechnologies into biological system for the design of highly functional material and machine. Various studies have been conducted, allowing for successful incorporation of nanobionics in plant (Ghorbanpour and Fahimirad, 2017). For example, (Giraldo *et al.*, 2014b) reported the incorporation of NM into a plant to enhance light absorption for better photosynthetic efficiency. Chloroplast photosystem within the plant cell tends to capture more photon, converting them into electron flow as energy for photosynthetic activities under bright sunlight. To produce similar photosynthetic capability under low sunlight conditions, absorption of solar light from a broader range of different electromagnetic wavelengths such as UV-light and near-infrared (NIR) light which are usually not absorbed by chloroplast pigment are required. The unique optical and electronic properties of CNT help to enhance light absorption at dim light conditions. Embedment of CNT onto chloroplast alters its photosynthetic profiles, allowing for light absorption of both UV light and NIR light spectrum (Giraldo *et al.*, 2014b). This CNT allows them to convert more light from different wavelength into exciton, transferring electron for photosynthetic activities and improving photosynthetic efficiency. Moreover, NMs such as CNT are also embedded in plants, modifying them into biosensor (Wong *et al.*, 2017; Lew *et al.*, 2021). Normal analyte detection method requires extensive and a complicated series of processes such as sampling collection and pre-treatment as well as involving expensive and bulky analytical equipment. This method generally does not provide real-time detection reflecting the concentration of the analyte and merely rely on the slow phenotypic changes such as significant reduction in chlorophyll concentration. On the other hand, CNT-based NIR fluorescence nanosensors can be tailored specifically for a single target analyte. These nanosensors are usually embedded into the plant leaf mesophyll via syringe infiltration. The target analyte would be absorbed through the roots, moving up towards the leaf. These analytes would be accumulated in contact with the nanosensors and the NIR fluoresence for the nanosensor complexes will be detected by InGaAs detector, showing real-time concentration of the target analyte. One of the common analyte detections that use nanosensor is arsenic. To further improve the detection efficiency of nanosensors, a specific type of plant is used where nanosensors are integrated into cretan brake fern (*Pteris cretica*). This plant possesses the capability of hyperaccumulating a high level of arsenic, allowing detection range up to ppb ranges (Lew *et al.*, 2021). Furthermore, nanobionic light-emitting plant are synthesised to possibly provide light during night time. Administration of firefly-luciferase as the catalysts alongside with luciferin are performed through leaf mesophyll and stomata where they are to be localised near organelles with high ATP generation such as chloroplast and mitochondria. ATP is the energy molecules for all organelle activities. Luciferin in the presence of firefly-luciferase as catalyst as well as magnesium ions (Mg^{2+}) would be oxidised for generation of yellow-green photoemission (Kwak *et al.*, 2017).

3.4.5 Applicability of nanobionics in microalgae

Recent research by (Giraldo *et al.*, 2014b; Książyk *et al.*, 2015; Xia *et al.*, 2015) on enhancement of microalgae by NMs have proven that NMs do promote microalgal growth by improving photosynthetic activities and efficiency. However, these scenarios are only proven at low exposure of NM on microalgae. Taking advantage on these impacts of NMs on microalgae, it is possible to apply nanobionics on microalgae to enhance cell growth. For example, studies have been conducted by (Lambreva *et al.*, 2015) where integration of CNTs into algae shows promising results where photosynthetic efficiency is improved. CNTs are introduced into microalgae through passive mechanisms such as membrane diffusion and spontaneous surface reaction (Giraldo *et al.*, 2014b). Embedment of CNTs onto chloroplasts would allow greater range of light spectrum between NIR and UV to be absorbed and converted into exciton which deliver electrons for photosynthetic activities. This is generally owed to the exceptional optical and electronic properties of CNTs which allow the absorptions of a wider range of light spectrum for photosynthetic activities. However, there is an issue posed to the incorporation of CNTs in microalgae, which is the toxicity of CNT itself. High concentrations of CNTs exposure on microalgae tend to show toxicity halting the cell growth. Thus, cerium oxide NM (CeO_2-NM) or nanoceria can be utilised to counteract the toxicity produced by CNTs. Nanoceria is widely known as one of the best reactive oxygen scavengers which can reduce CNT toxicity generated through induced ROS (Giraldo *et al.*, 2014b). High ROS level is one of the main reasons for the growth inhibition of microalgae at high concentration of CNT. Nanoceria usually interchanges between Ce^{3+} and Ce^{4+} ions forming oxygen vacancies, reducing hydroxyl and superoxide radicals which are vital for ROS generation. However, growth inhibition starts to occur when nanoceria concentration increased above 5 mg/L (Pulido-Reyes *et al.*, 2015). Localisation of CNT in chloroplast photosynthetic machinery and nanoceria at chloroplast envelope could possibly create an intercellular environment of potentially low ROS level which are suitable in enhancing the photosynthetic activities and efficiency, promoting microalgae growth.

3.4.6 Future perspectives & challenges

Enhancement of NMs on microalgae have been proven to have only worked within limited range of NM concentration (Książyk *et al.*, 2015; Xia *et al.*, 2015; Wong *et al.*, 2017). The incorporation of low concentration NM in microalgae promotes growth by inducing photosynthetic activities as well as improving photosynthetic efficiency, which will then reduce CO_2 content in the aquatic environment where CO_2 is converted into oxygen (O_2) for aquatic organisms. However, incorporation of NMs in microalgae are only conducted under lab-scales and pilot plants which NMs concentration are easier to be managed within permitted range for hormetic response. In these studies, small quantity of microalgae are generally soaked within the NMs solutions allowing interactions between them, triggering hormetic responses, promoting cell growth. In larger microalgae cultivation system such as open ponds, it would be difficult to ensure homogeneity of NM concentration throughout the ponds. Regions with high NM concentration would inhibit microalgal growth, whereas low NM concentration regions would promote growth. The imbalanced microalgal growth across the pond will require additional separation process between dead microalgae with the remaining before any extraction of biomass, lipids and protein as high NM concentration may inhibit cell growth, resulting in cell death. Thus, further studies should be performed to counter the issue.

3.4.7 Conclusion

The interaction between NMs and microalgae is proven to have both positive and negative effects on the microalgae. Higher chlorophyll level improves photosynthetic activity by stimulating ROS levels at low NM concentrations. Damaged photosynthetic machinery would eventually lead to cell death at high NMs concentration. Combination of nanoceria and CNTs within microalgae is a possible solution to enhance the microalgal growth. Nanoceria serves as oxygen scavenger to induce ROS by CNTs promotes microalgal growth. However, the feasibility of the system requires comprehensive studies such as alternative to CNTs, dosage optimisation, possible recovery and reuse of NMs.

CHAPTER 4
METHODOLOGY

4 Methodology

4.1 Setup of microalgae cultivation system

The PBR consisted of a 1 L Schott bottle with two plastic tubings inserted into it, one for gas supply (0.1 v/v culture medium) and the other for sample collection. A 45 mm long magnetic stirrer was placed at the bottom of the PBR to induce stirring mechanisms. The gas supply consisted of (2 v/v %) CO_2 and air. The experiment was conducted at a room temperature of (23-25 ^oC).

4.2 Preparation of microalgae culture

The Chlorella vulgaris (FSP-E) microalgae strain, which was obtained from the University of Nottingham Malaysia, was used in this investigation. The strain selection was mainly due to the fast-growing and high protein content of FSP-E. The microalgae were cultivated within the proposed PBR, which comprises a 1 L PBR with CO_2 and air supply. In addition, the mixture is pre-mixed with BG11 nutrient solution and 2.5 mL of silicone. Table 4 shows the composition of the BG11 nutrient solution. Pre-culture of microalgae was completed for at least a week within a 500 mL Schott bottle PBR with BG11 solution and 1.25 mL of silicone under continuous supply of CO_2.

Table 4. Composition of BG11 nutrient solution

Chemical compound		Concentration (g/L)
Main	$NaNO_3$	1.500
	K_2HPO_4	0.030

	$MgSO_4.7H_2O$	0.075
	$C_6H_8O_7$	0.006
Stock 1	Na_2CO_3	2.000
Stock 2	$CaCl_2.2H_2O$	3.600
Stock 3	$C_6H_8FeNO_7$	0.600
	ETDA	0.100
Stock 4	H_2BO_4	2.860
	$MnCl_2.4H_2O$	1.810
	$ZnSO_4.7H_2O$	0.222
	$Na_2MoO_4.2H_2O$	0.300
	$CuSO_4.5H_2O$	0.070
	$Co(NO_3)_2.6H_2O$	0.040

4.3 Effect of stirring on microalgal growth

The experiment was conducted by altering the stirring speed of the magnetic stirred plate. The 1 L PBR was placed on top of the magnetic stirrer plate (FAVORIT Magnetic Stirrer) where the stirring speeds were set from 360 to 450 rpm with an interval of 30 rpm. Samples were taken every two days, and the samples' absorbance was determined using the UV-vis spectrometer (UV-1800, SHIMADZU). The wavelength used for FSP-E samples was 680 nm. The absorbance was used as an indicator of microalgal growth. The experiment was stopped when the absorbance values reached three consecutive stagnant values, indicating that the microalgae have reached maturity. The microalgal biomass was then harvested by centrifuging at 6000 rpm for 5 min. The supernatant liquid was removed, and the biomass at the bottom was collected. The biomass was then sent to freeze-drying for 48 hours. The experiments were then repeated three times.

4.4 Effect of bubbling on microalgal growth

The experiment was conducted by altering the bubbling rate. The gas mixture supply to the 1 L PBR was varied between 50 and 200 cc/min. Samples were taken every two days, and the samples' absorbance was determined using the UV-vis spectrometer (UV-1800, SHIMADZU). The wavelength used for FSP-E samples is 680 nm. The absorbance was used as an indicator of microalgal growth. The experiment was stopped when the absorbance values reached three consecutive stagnant values, indicating that the microalgae reached maturity. The microalgal biomass was harvested by centrifuging at 6000 rpm for 5 min. The supernatant liquid was removed, and the biomass at the bottom was collected. The biomass was then sent to freeze-drying for 48 hours. The experiments were then repeated three times.

4.5 Protein and carbohydrate analysis

4.5.1 Protein

The protein content within the microalgae biomass was extracted based on the research method conducted by Phong et al. (2018). 0.1 g of microalgae sample was mixed with 10 mL of water and 0.5 N KOH. The mixture was then vortexed for 60 s, followed by ultrasonication at 35 kHz for 20 min in an ultrasonic water bath (Elmasonic P 30 H). After that, the mixture was centrifuged at 7000 rpm for 5 min to destroy the cell wall, releasing the protein contents. The supernatant was collected while the remaining pellets were removed. The supernatant containing the protein content was analysed using the Bradford method. 0.25 mL of the supernatant sample was mixed with 2.5 mL of Bradford reagent, and the mixture was then measured using a UV-Vis spectrometer at a wavelength of 595 nm.

4.5.2 Carbohydrates

Carbohydrate compounds within the microalgae biomass were extracted by using the modified method of Pleissner (2013). For 50-100 mg of lyophilised biomass, 0.5 mL of 18 M H2SO4 and 4.5 mL of deionised water were added to the biomass. The mixture was then autoclaved at 121 ^oC for 30 min, followed by centrifugation for 10 min. Carbohydrate quantification was conducted based on the phenol-sulphuric acid method by Dubois et al. (1956). For 1 mL of supernatant, 5 mL of concentrated sulphuric acid (H_2SO_4) and 1 mL of 5 % phenol solution were added, and the mixture was shaken thoroughly. After 10 min, the absorption was measured with a UV-vis spectrophotometer at 490 nm. The starch of known mass was used as a sample for the standard.

4.6 Cell disruption studies

Samples taken after the microalgae culture in 1 L PBR reaches maturity were collected and centrifuged at a lower speed of 2000 rpm for 10 min to remove excessive water from the microalgae. The supernatant liquid was removed, and the biomass at the bottom was collected. The biomass samples were then sent to field emission scanning electron microscopy (FE-SEM, Fei Quanta 400F) imaging to determine the cell structures.

4.7 Mathematical modelling for the proposed system

From Zhang et al (2021),

$$f(\varepsilon) = ce^{\frac{-(\varepsilon-a)^2}{b}} \qquad (6)$$

where f is the growth rate of microalgae, c is the turbulence coefficient at the optimal turbulence, ε is the energy dissipation rate due to centrifugation, a is the optimal centrifugation speed for maximum microalgae growth, and b is the adjustment coefficient of turbulence on microalgae growth. From Hondzo et al (1998),

$$\frac{df}{dt} = Af \qquad (7)$$

$$f = f_0 e^{At} \qquad (8)$$

where f_0 is the initial microalgae growth rate, t is time, and A is the growth rate constant.

In our mathematical model, we considered equation (6) and assumed that it follows a growth rate similar to equation (7), giving

$$\frac{df}{dt} = \frac{-(\varepsilon(t)-a)^2}{b} f \qquad (9)$$

where $\varepsilon(t)$ is dependent on time, so that

$$f(t) = f_0 e^{\frac{-(\varepsilon(t)-a)^2}{b}} \qquad (10)$$

which gives us equation (6) at any particular time t.

Taking $\alpha = \frac{-b}{(\varepsilon-a)^2}$, we have

$$\alpha \frac{df}{dt} = f \qquad (11)$$

In equation (11), it was assumed that the magnitude of the shear force from centrifugation has no impact on the death rate of the microalgae. If we assume that the death rate $g(\varepsilon)$ of microalgae due to the damage by the shear force from centrifugation, equation (11) can be rewritten as

$$\alpha \frac{df}{dt} - g(\varepsilon(t)) = f \qquad (12)$$

The first term of (12) is the growth rate of microalgae due to centrifugation, and the second term corresponds to the death rate of microalgae due to cell membrane damage from centrifugation, and hence the negative sign. Rearranging (12) gives

$$\alpha \frac{df}{dt} - f = g(\varepsilon(t)) \qquad (13)$$

From Warnaars et al (2006), since the angular centrifugation speed ω is proportional to ε, equation (13) can be rewritten as

$$\alpha \frac{df}{dt} - f = g(\omega(t)) \qquad (14)$$

We had determined $g(\omega(t))$ from experiments, and hence solved equation (14) to give a relationship between the growth rate of microalgae and the angular centrifugation speed.

4.8 Statistical analysis

The total lipid, protein and carbohydrate content data were subjected to one-way ANOVA with two tailed *t*-test (with significance $p \leq 0.05$) data analysis using Microsoft Excel 2016. The data were inputted in Anova: Two-Factor With Replication using Data Analysis Toolpak in Excel. The significance of the data was determined using the p-value obtained, the results were shown in Table S36. The data presented was the average of three replicates.

CHAPTER 5

RESULTS AND DISCUSSIONS

5. Results and Discussion

5.1 Effect of stirring on the bubbling mechanism

The effect of stirring motion on the bubbling mechanisms were observed at different rotational speeds. Instead of testing the study on a microalgae culture, it was performed with distilled water in the same PBR used for the microalgae culture. The bubbling rate was kept constant at 500 cc/min, similar to experimental settings. The stirring speeds were then varied from no stirring (0 rpm) to 700 rpm. It was observed that the bubbles tend to be larger at low stirring speeds. As the stirring speed increases, the bubbles were further broken down into smaller bubbles. In addition, the bubbles were generally drawn towards the rotating blade located in the centre of the PBR. Figures 7 and 8 showed the changes in the movement and size of the bubbles at different stirring speeds.

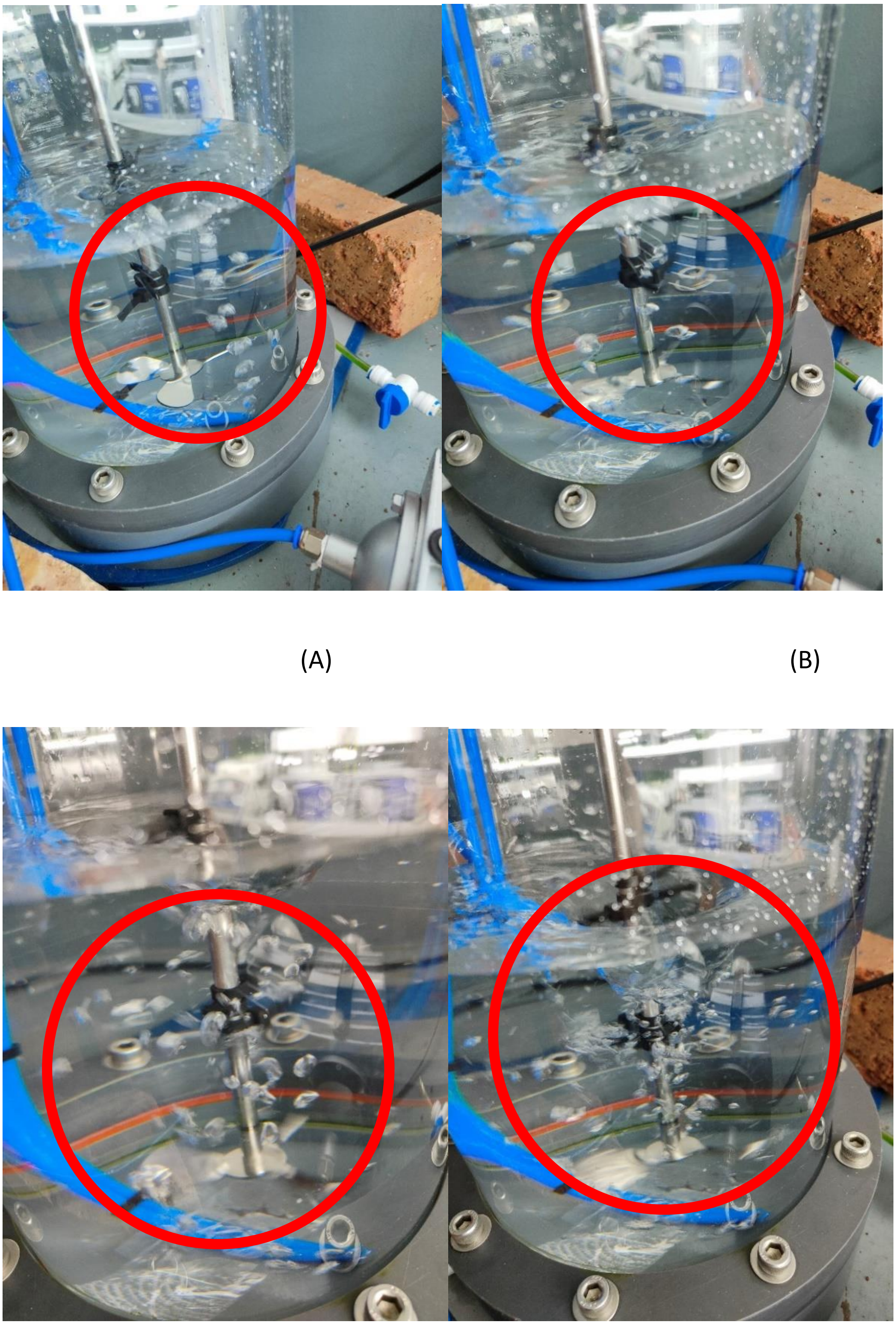

(A) (B)

(C) (D)

Figure 7. The effect of stirring on the bubbling mechanism. (A)No stirring,0 rpm; (B) 100 rpm; (C) 200 rpm; (D) 300 rpm

(E)

(F)

(G)

Figure 8. The effect of stirring on the bubbling mechanism. (E) 500 rpm; (F) 600 rpm; (G) 700 rpm (continued)

Duan (2018) has reported that according to Euler's model, the interfacial momentum transfer between the fluid and bubbles, F_q, is represented by the equation below:

$$F_q = F_G + F_B + F_D + F_L + F_{VM} + F_P \qquad (15)$$

F_G is the gravitational force acting upon bubbles, F_B is the buoyancy force, F_D is the drag force, F_L is the lift force, F_{VM} is the virtual mass force, and F_P is the pressure gradient force. The equations for each type of force are as follows:

$$F_G + F_B = \frac{\rho_b - \rho_l}{\rho_b} g \qquad (16)$$

$$F_D = \frac{18 \mu_l C_D \Re}{24 d_b^2 \rho_b} (u_l - u_b) \qquad (17)$$

$$F_L = C_L \frac{\rho_l}{\rho_b} (u_l - u_b) \times \nabla \times u_l \qquad (18)$$

where ρ_b is the bubble density, ρ_l is the fluid density, g is the gravitational acceleration, C_D is the drag coefficient, C_L is the lift coefficient, u_l is the fluid velocity, u_b is the bubble velocity, Re is the Reynolds number for bubbles, and d_b is the average bubble size. F_{VM} and F_P were negligible because of the low bubble velocity gradient and the relatively large density ratio between the bubbles and fluid. It was observed that when the stirring speed increases, the bubbles tend to move horizontally along the vortex formed and moved more slowly vertically. This was in line with equation 17, where the increase in the stirring speed indirectly caused turbulence within the system, resulting in a higher Re number, followed by increased F_D. Hence, when F_D increases at a higher rate than F_L, this hindered the bubbles from moving up to the top of the column.

Moreover, the increase in the stirring speed resulted in a visible reduction in the size of the bubbles moving up the column. The increased stirring speed created a more turbulent fluid system, inducing the deformation of fluid particles by fluctuations in the eddies. The fluctuating velocity of the particles produces the kinetic energy that increased the surface energy of the fluid particles up to a point at which the energy is sufficient to break down the bubbles. The centripetal force played a role in moving the bubbles towards the centre of the PBR, where the rotating impeller is placed. Newton's 2nd law of motion states that the acceleration of a body is directly proportional to the force exerted upon the body. In this case, the force exerted on the bubbles is the centripetal force, which is represented by the following equation:

$$F = \frac{mv^2}{r} \qquad (19)$$

where r is the radius of the bubble motion with respect to the rotating impeller, and v is the velocity of the fluid.

The rotating blade acted as the centre of the centripetal forces, while the fluid acted as the 'string' that connects both the centre and the bubbles. It can be observed that as the stirring speed increases, the bubbles tend to move closer towards the centre. This can be related to equation 19, where the increase in the velocity of the fluid surrounding the bubbles is stronger than the centripetal forces acting upon the bubbles, pulling them closer to the centre. In general, an increase in stirring speed has led to a few scenarios:

1. The bubbles tended to move more slowly up the vertical direction, indicating a more extended holdup period.

2. More bubble breakages/fragmentations occur, resulting in smaller bubbles.

3. The bubbles are pulled horizontally closer towards the centre of the rotating impeller.

5.2 Effect of stirring motion on microalgae growth

5.2.1 Biomass for FSP-E cultivated under different stirring speeds

Increasing the stirring speed within a fluid led to a constant motion of the fluid particles, which induced turbulence between them, allowing increased mass transfer between the particles. The stirring speed was set based on the stirring level on the magnetic stirring plate (i.e. Level 0, 0 rpm; Level 1, 360 rpm; Level 2, 390 rpm; Level 3, 420 rpm). FSP-E cultivation under no stirring conditions yielded 4.4019 g biomass/L FSP-E. Increased stirring speed up to 360 rpm did not significantly change biomass yield (4.335 g biomass/L FSP-E). However, when the stirring speed reached 390 rpm, the biomass yield reached the highest point at 6.157 g biomass/L FSP-E before decreasing to 5.229 g biomass/L FSP-E. Figure 1 plotted the average biomass concentration against the corresponding stirring speeds.

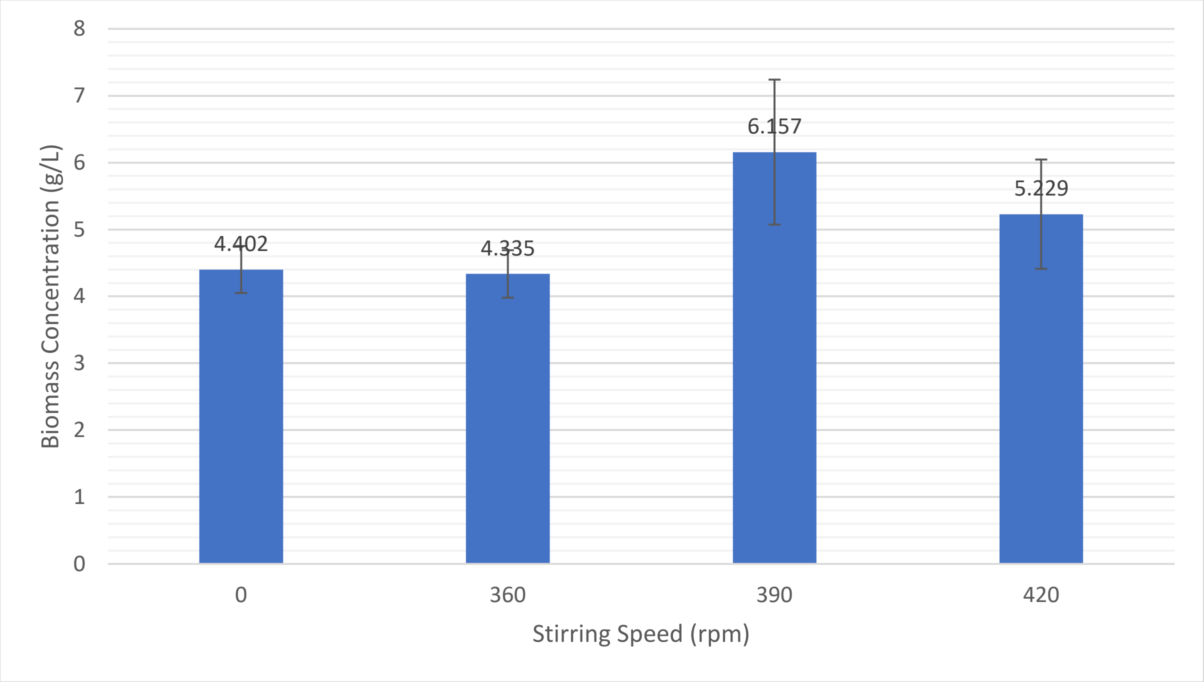

Figure 9. Biomass concentrations at different stirring speeds

Based on Figure 9, it was noticed that the biomass concentration remained relatively constant at low stirring speeds from 0 to 360 rpm and increased to its highest point at 390 rpm before decreasing when the stirring speed reached 420 rpm. This was further supported by data on the absorbance recorded by the UV-vis spectrometer. The absorbance for FSP-E cultivation under a stirring speed of 390 rpm recorded the highest absorbance (~4.2) upon reaching maturity compared with other stirring speeds (0 rpm, ~3.0; 360 rpm, ~3.5; 420 rpm, ~3.6) (see Figure 10). Raw data for the absorbance curves were list in Table S1-S12.

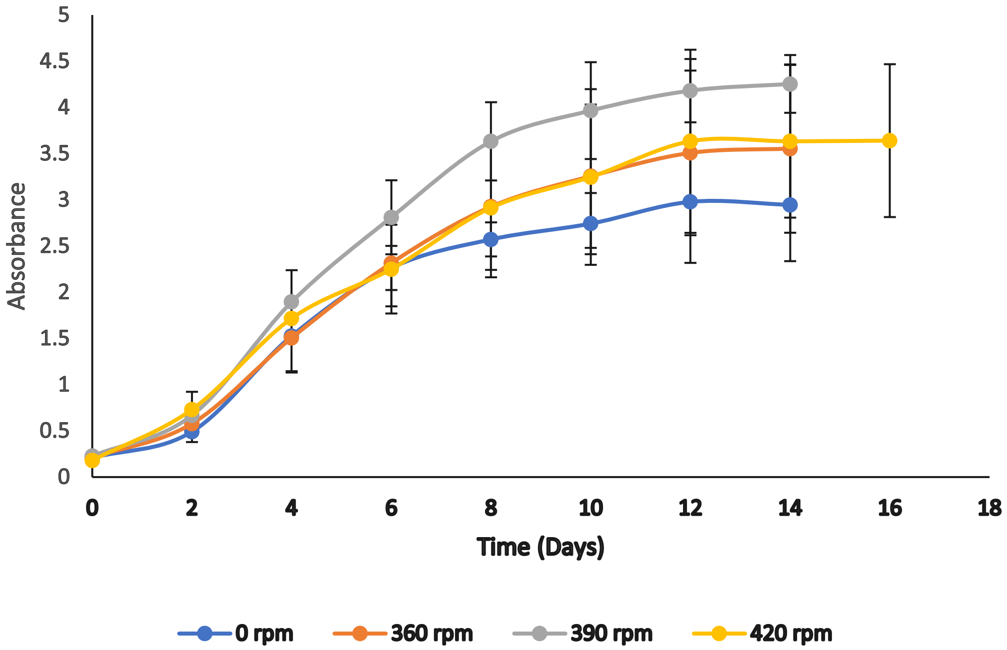

Figure 10. Microalgae absorbance over 14 days

Figure 10 showed the experimental results for the absorbance at various rpm rates. Based on these experimental results, this work proposes that $g(\omega(t)) = e^{\omega^2 t}$. Hence, equation (14) becomes

$$\alpha \frac{df}{dt} - f = e^{\beta t} \qquad (20)$$

where $\beta = \omega^2$. By applying the Laplace transform on both sides of equation (20), equation (20) becomes

$$L\left\{\alpha \frac{df}{dt} - f\right\} = L\{e^{\beta t}\} \qquad (21)$$

$$\alpha L\left\{\frac{df}{dt}\right\} - \bar{f}(s) = \frac{1}{s-\beta} \qquad (22)$$

$$\alpha[s\bar{f}(s) - f(0)] = \frac{1}{s-\beta}. \qquad (23)$$

For $\lim_{t\to 0} f(t) = 0$, equation (23) becomes

$$\alpha\left[s\bar{f}(s)\right] = \frac{1}{s-\beta} \qquad (24)$$

which leads to

$$\bar{f}(s) = \frac{1}{\alpha\beta}\left[\frac{-1}{s} + \frac{1}{s-\beta}\right]. \qquad (25)$$

Applying inverse Laplace transform to equation (25) gives

$$L^{-1}\{\bar{f}(s)\} = f(t) = \frac{1}{\alpha\beta}\left(e^{\beta t} - 1\right). \qquad (26)$$

This work assumes a homogeneous differential equation for a control setup with no stirring.

$$\alpha_0 \frac{df}{dt} - f = 0. \qquad (27)$$

Solving equation (27) gives

$$f(t) = e^{\alpha_0 t} + c \qquad (28)$$

where c is a constant of integration corresponding to the system's initial condition. Equation (26) is used to fit the experimental results presented in Figure 10, and the results are shown in Figure 11.

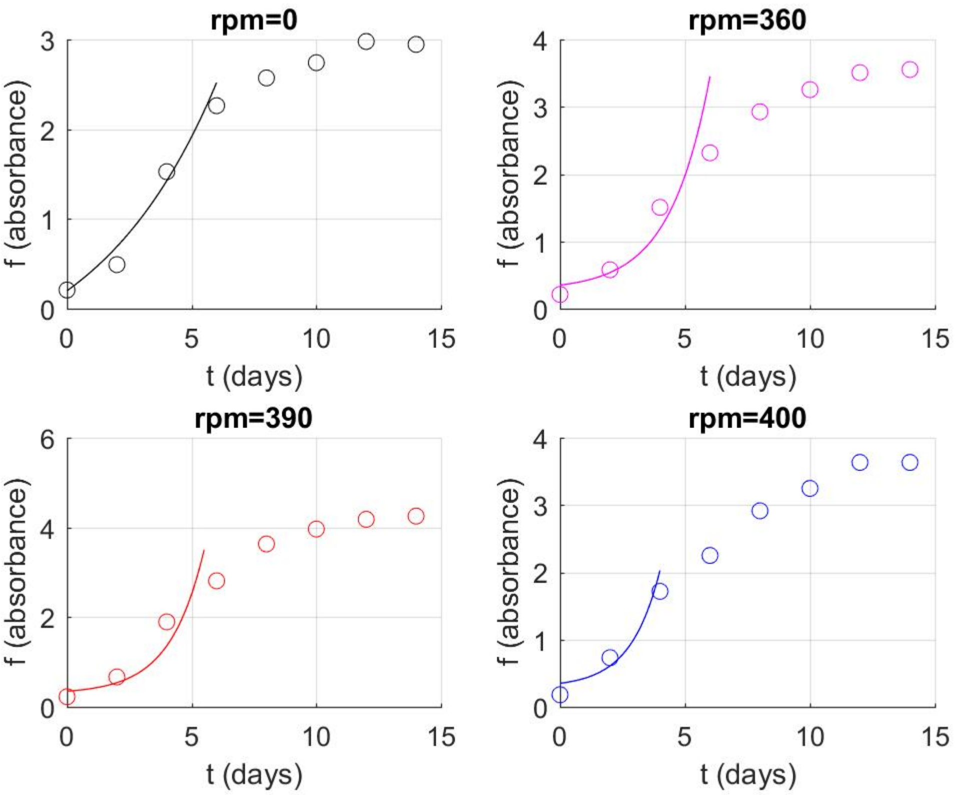

Figure 11. Fitting of the theoretical results to the experimental results. The Scatter plots and line plots correspond to the experimental and theoretical results.

Figure 11 showed that the theoretical results agree with the experimental results for the accelerated growth regions of the graphs. The theoretical result did not capture the drop in the growth rate, as it did not assume growth inhibition when the biomass reached a critical point at which the amount of light reaching the microalgae was reduced due to the blocking of light. Generally, a constant deceleration was observed between the 5th and 10th days of the 15 days.

To account for growth inhibition due to light blocking, the equation was rewritten as follows:

$$\frac{df}{dt} - \frac{1}{\alpha} \cdot f = \frac{1}{\alpha} \cdot e^{\beta t}. \qquad (29)$$

By taking a general form $\alpha = 2\beta(t-\mu)$ where μ is a constant, equation (29) is then modified to

$$\frac{df}{dt} - \frac{1}{\alpha} \cdot f = \frac{c}{\alpha} e^{\beta t} + c\beta e^{\beta t} \qquad (30)$$

where c is a general constant and the second term on the right-hand side corresponds to the growth inhibition due to light blocking. Equation (30) is solved similarly to give

$$f(t) = ce^{\beta t} + \gamma e^{-\beta(t-\mu)^2} \qquad (31)$$

where γ is a constant. Figure 12 shows a plot of the theoretical function (continuous line) and the experimental data with a stirring rate of 390 rpm.

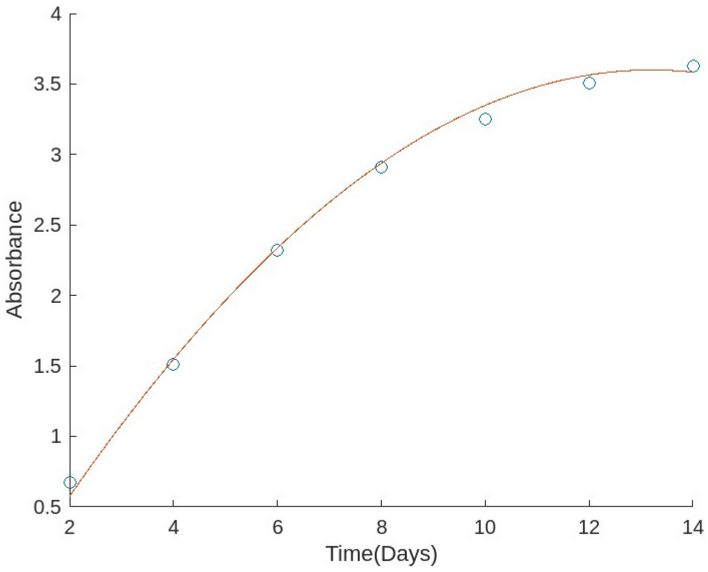

Figure 12. Fitting of the theoretical result to the experimental results for a stirring rate of 390 rpm. The Scatter plots and line plots correspond to the experimental and theoretical results respectively.

The theoretical model fitted well with the experimental data over the entire time range. Values of parameters obtained from graph: $c = -81.1, \beta = 0.00025, \gamma = 85, \mu = 14.4$. c and γ are dimensionless constants to balance the choice of units, β is in rad^2/s^2, and μ is in seconds. This theoretical model can be incorporated into an artificial intelligence database as a starting point for machine learning to cultivate other microalgae strains.

The increase in biomass concentrations from 360 to 390 rpm was due to an increased mass transfer rate between the nutrient media and FSP-E cells. A higher stirring speed induced greater turbulence within the cultivation medium, creating more contact between nutrient particles and FSP-E cells, thereby increasing the nutrient intake rate of FSP-E. Furthermore, increased stirring speed exerted a certain degree of mechanical stress on FSP-E cells. This stress induced hormetic responses in FSP-E cells, forcing them to engage in its ‘fight and flight’ mode. Lau (2022b) reported that a certain degree of these responses indirectly promoted intracellular metabolism, promoting cell growth. However, it was observed that microalgae concentrations dropped with a further increase in the stirring speed from 390 rpm to 420 rpm. One of the reasons for this was likely due to the mass transfer limitation, whereby the nutrient intake by FSP-E cells reaches saturation, as excessive nutrient supplies cannot be absorbed by FSP-E cells for growth. Moreover, although the hormetic responses of FSP-E cells due to mechanical stress through stirring motions could promote cell growth, there was still a limit to the mechanism's effectiveness in this aspect. In particular, higher stirring motions led to increased centripetal forces acting on FSP-E cells, which could damage the cell wall over a prolonged period. This led to cell wall breakdown and the release of inner cell content, leading to cell death. Figure 20 showed microalgal cell disruption at different stirring speeds.

5.2.2 Total protein content in microalgae

The total protein concentration was determined using Phong et al. (2018) ’s method, followed by the Bradford method. A known concentration of bovine serum albumin (BSA) protein standard was plotted against its absorbance at wavelengths of 595 nm using a UV-vis spectrometer. The standard curve for the absorbance vs. protein curve is

$$y = 0.3282x \qquad (32)$$

where y is the absorbance value, whereas x is the protein concentration (mg/mL). The protein concentration standard curve was listed as Figure S1.

The total protein concentration of FSP-E exhibited an increasing trend. For instance, the protein concentration increased slightly from 0.559 mg/mg biomass in the control to 0.575 mg/mg biomass when the stirring speed was increased to 360 rpm. A slump in protein concentration occured when the stirring speed is increased from 360 rpm (0.575 mg/mg biomass) to 390 rpm (0.475 mg/mg biomass). Furthermore, there was an increase in the protein concentration when the speed was increased from 390 rpm (0.475 mg/mg biomass) to 420 rpm (0.577 mg/mg biomass). Protein precipitation contributed to the increasing trend in total protein concentrations with increasing stirring speed. Similar trends were observed, where increased mechanical stress on the cells promoted protein precipitation, allowing more protein content to be extracted, thereby increasing the total protein concentration. Raw data for the protein absorbance and fractions were list in Table S28-S29.

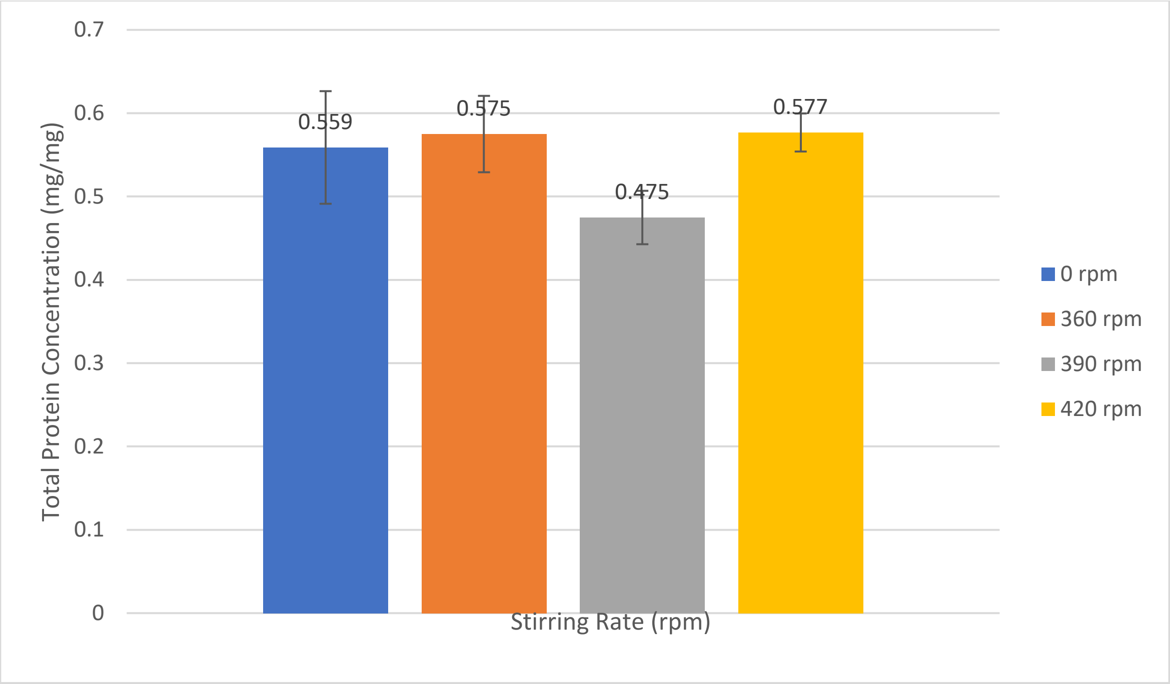

Figure 13. Total protein concentration at different stirring speeds

The total protein content at different speeds did not exhibit a similar trend to the microalgal growth and biomass concentration graphs (Figure 9). The increased stirring speed disrupted the cell structure, damaging the cell wall. The ‘flight and fight’ responses induced by mechanical stress through the stirring motion likely occurred when the stirring speed is increased from 0 to 360 rpm, increasing both the growth rate and total protein content. Even though the further increase in stirring speed up to 420 rpm caused greater damage to the cell wall, as shown in Figure 20, possibly leading to the breakdown of the cell wall and causing cell rupture, it was noted that the damage had less effect on the protein content. Since the protein content in microalgal cells was generally stored within the vacuoles, it was safe to assume that the impact of the damage on the vacuoles is different from that on the cell wall; vacuoles were still intact, preventing any leakage of the protein content. The total protein concentration in mass fraction (w/w) at 390 rpm (0.475 mg/mg biomass) had a considerable difference compared with that of 360 rpm and 420 rpm (0.575 mg/mg biomass and 0.577 mg/mg biomass); however, the actual protein concentrations were still increasing trend (360 rpm – 2.493 mg, 390 rpm – 2.923 mg, and 420 rpm – 3.016 mg).

5.2.3 Total carbohydrate concentration in microalgae

Carbohydrate compounds within the microalgae biomass were extracted using the modified Pleissner method (2013). Known concentrations of the starch standard are plotted against their absorbance at wavelengths of 490 nm using a UV-vis spectrometer. The standard curve for the absorbance vs. carbohydrate curve is

$$y = 8.8961x \qquad (33)$$

where y is the absorbance value, whereas x is the carbohydrate concentration (mg/mL). The carbohydrates concentration standard curve was listed as Figure S2.

The total carbohydrate concentration graph showed similar trends to the microalgal growth and biomass concentration graphs (Figure 9). The total carbohydrate concentration for FSP-E demonstrated an increasing trend from 0 to 360 rpm, followed by a drop from 360 to 390 rpm before a slight increase in the concentration when the stirring speed reached 420 rpm. For example, the carbohydrate concentration increased from 0.096 mg/mg biomass in the control to 0.117 mg/mg biomass when the stirring speed was increased to 360 rpm. Carbohydrate concentration decreased when the stirring speed was increased from 360 rpm (0.117 mg/mg biomass) to 390 rpm (0.076 mg/mg biomass). This was followed by a slight increase in carbohydrate concentration when the speed was increased from 390 rpm (0.076 mg/mL) to 420 rpm (0.087 mg/mg biomass). Raw data for the carbohydrates absorbance and fractions were list in Table S30-S31.

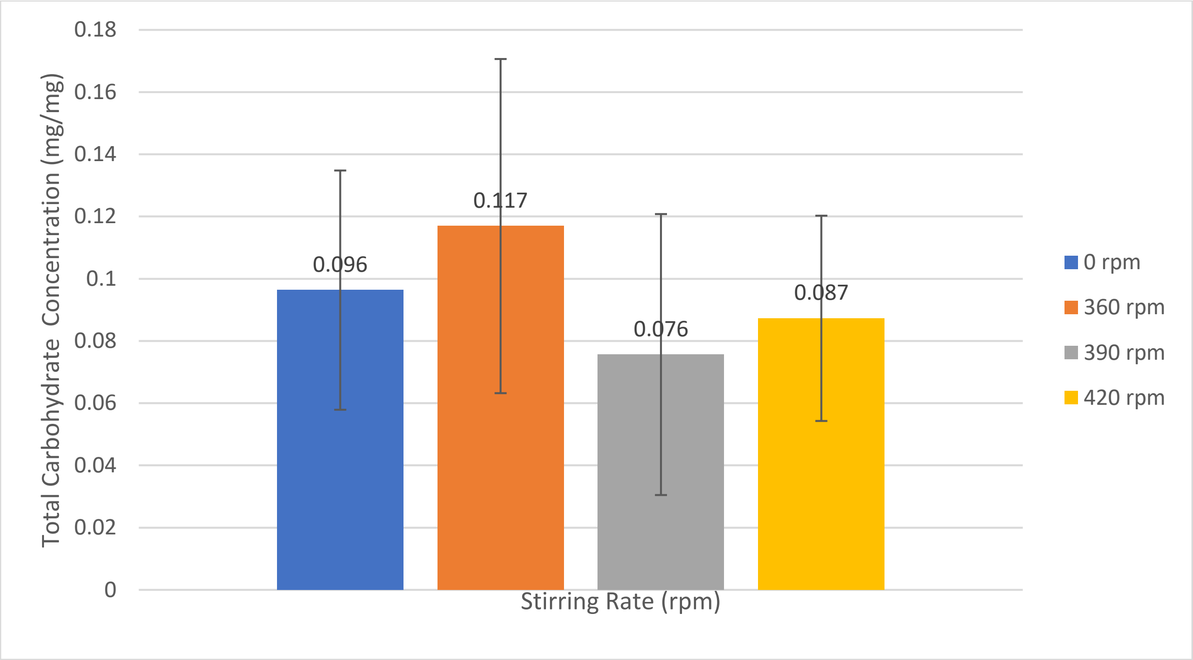

Figure 14. Total carbohydrate concentration at different stirring speeds

The increase in total carbohydrate concentration from 0 to 360 rpm was due to the mechanical stress imposed by the stirring motion, which induced hormetic responses from the FSP-E cells in an attempt to counter the impact, which is consistent with cells secreting reactive oxygen species (ROS) under stress. This indirectly promoted cell growth, leading to increased carbohydrate production and assimilation within cells. (Lau *et al.*, 2022b). However, a further increase in the stirring speed from 360 to 390 rpm demonstrated that the microalgal cell wall cannot withstand the larger shear stress caused by the stirring motion at 390 rpm. This larger shear force damaged the cell wall, eventually leading to its breakdown. Carbohydrate contents within microalgal cells were typically stored within the chloroplast and cytoplasm, among the cell's largest organelles (Cheng *et al.*, 2017). Breakdown of the cell wall led to leakage of the inner cell content, which mainly consists of the cytoplasm. This leakage of inner cell content resulted in cell death. For the surviving microalgal cells, the leakage of carbohydrates in the form of cytoplasm reduced the total carbohydrates within the cell. Although there was a slight increase in carbohydrate concentration from 390 to 420 rpm, the increase was relatively small compared to the total biomass.

5.2.4 Conclusion

Through theoretical modelling and experimentation, this work demonstrated that including a stirring motion in the cultivation system, which induced turbulence, allowed for better mass transfer between nutrients and air with the microalgal cells. This is well supported by the results obtained, where the increased stirring speed (0 rpm to 390 rpm) has led to increased biomass concentration (4.402 g/L to 6.157 g/L). On the other hand, although a stirring speed of 390 rpm provided better biomass concentration, it did not result in the highest protein and carbohydrate composition compared with a stirring speed of 360 rpm. These results indicate that the optimum stirring speed for microalgal cultivation is 360 rpm, at which the total carbohydrate and protein concentrations were at the highest values, along with an acceptable biomass concentration. The increase in all three parameters is mainly due to the defensive mechanisms of microalgal cells to counter the mechanical stress caused by stirring motion. This work also involves the use of SEM imaging of FSP-E cells to show that when the stirring rate reaches the range of 350–450 rpm, the fouling resistance within the system was reduced, and the shear stress resulted in deposit removal, which in turn increased the contact period between microalgae cells with nutrients and O_2.

However, it was noticeable that a further increase in the stirring motion decreased biomass and total carbohydrate concentrations but not protein concentration.

The findings' practical applications at an industrial scale were also discussed. Particular attention was paid to how the theoretical model and experimental results could be applied to an automated microalgae cultivation system with upstream and downstream integration.

Stirring in the bioreactor paves the way for more efficient microalgae cultivation. Still, more research on other aspects is necessary before AI automation in cultivation is feasible. This includes investigating the material and geometrical structure of the bioreactor that gives the most efficient microalgae production, and future research may suitably include investigations on growth interference of various materials and container specifications, particularly involving marine microalgae.

5.3 Effect of bubbling motion on microalgae growth

An increased bubbling rate indicates an increased CO_2 and air supply to FSP-E for perspiration and photosynthesis. The bubbling rate was set at 15 % (150 cc/min) of the cultivation volume (1 L) with 50 cc/min increments. The biomass weight increased from 5.2290 g to 5.9128 g from 150 cc/min to 200 cc/min, before slightly decreasing to 5.6644 g at 250 cc/min. It was noticeable that the bubble size increased with the bubbling rate.

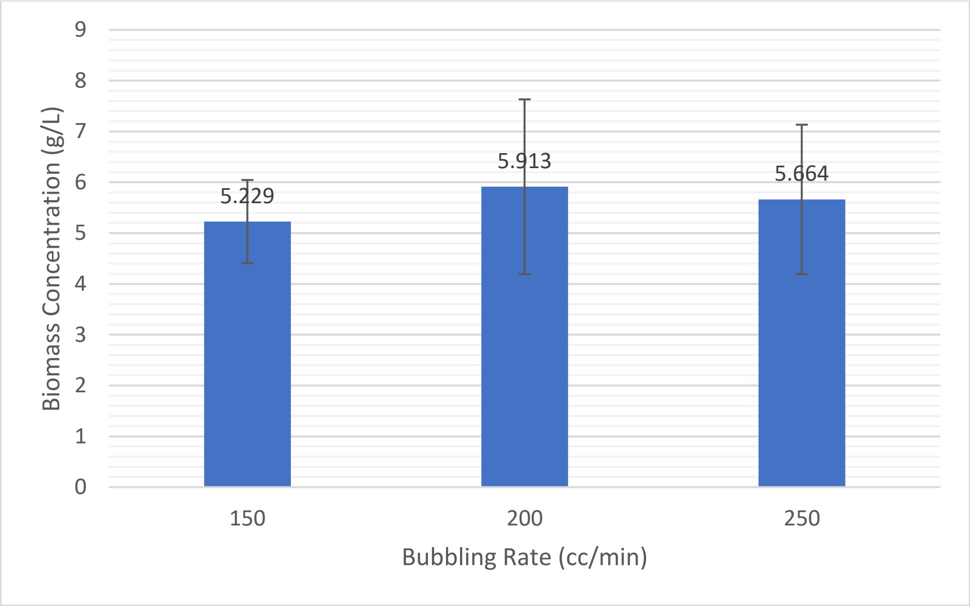

Figure 15. Biomass weight at different bubbling rates

Based on Figure 15, it was noticed that the biomass concentration increased from 150 to 200 cc/min at the highest point under constant stirring speed (390 rpm) before decreasing when the bubbling rate reached 250 cc/min. The optimal bubbling rate for FSP-E cultivation was 200 cc/min under constant stirring speed (390 rpm). This result was further supported by the absorbance recorded by the UV-vis spectrometer. The absorbance for FSP-E cultivation under the bubbling rate of 250 cc/min recorded the highest absorbance (~3.9) upon reaching maturity compared with other stirring speeds (150 cc/min, ~3.6; 250 cc/min, ~3.5). Raw data for the absorbance curves were list in Table S13-S21.

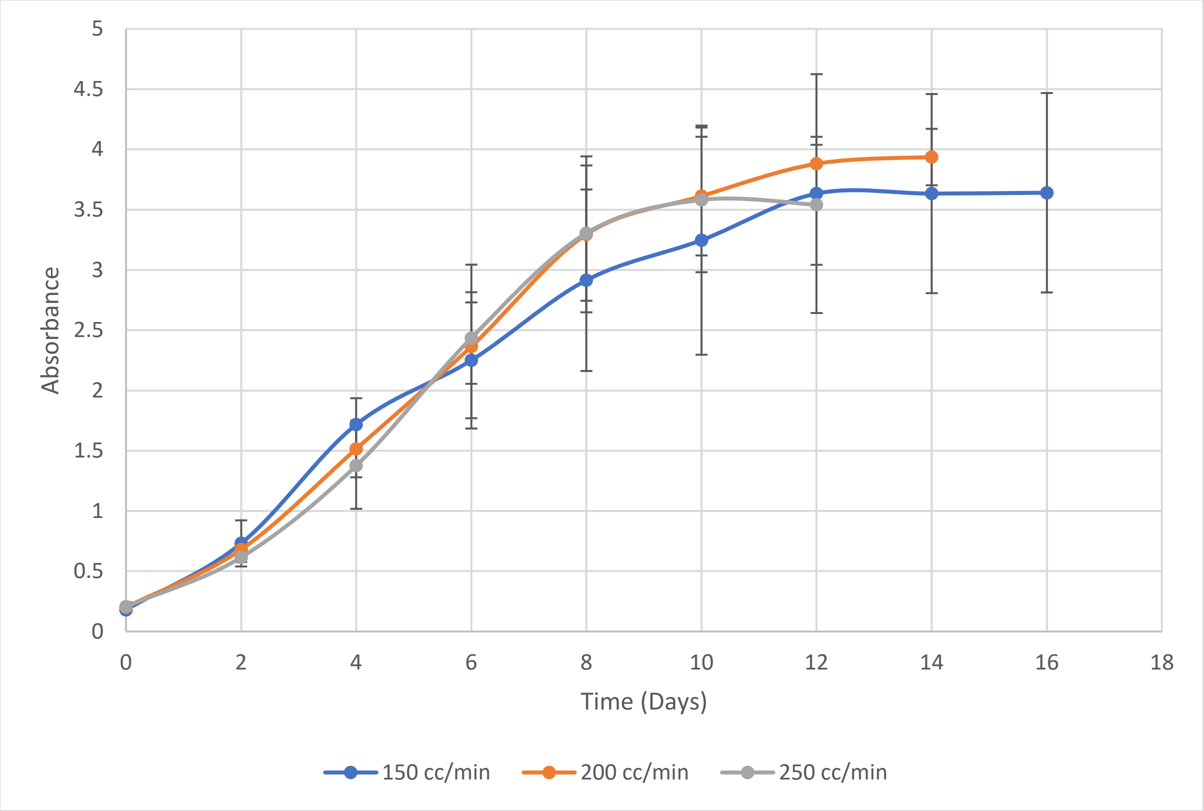

Figure 16. Microalgae absorbance over 16 days

The increase in biomass concentrations from 150 cc/min to 200 cc/min was due to the increased mass transfer rate between the nutrient medium and FSP-E cells. The higher bubbling rate induced greater turbulence and circulation within the cultivation medium, allowing more contact between nutrient particles and FSP-E cells, thus increasing the nutrient intake rate by FSP-E. However, there was a drop in microalgae concentration when the bubbling rate was increased to 250 cc/min. One of the reasons for this was probably due to the mass transfer limitation, whereby the nutrient intake by FSP-E cells reached its saturation, whereas excessive nutrient supplies could not be absorbed by FSP-E cells for growth. The increased bubbling rate was noted to have increased the bubble sizes, which, to a certain extent, reduced the surface-to-volume ratio between the gas bubbles and the microalgal cells. Moreover, the high bubbling rate indicated that the bubbles move up the column faster due to the increased fluid velocity. These factors reduced the contact time between gas bubbles and microalgal cells, resulting in lower mass transfer and thus lower microalgal growth rate.

5.4.1 Mathematical Modelling

From Lopez-Rosales et al (2017),

$$\frac{df}{dt} = \mu_{app} f \qquad (34)$$

where f is growth rate of microalgae, μ_{app} is the specific microalgae growth rate, and t is time. According to Lopez-Rosales et al (2017),

$$\mu_{app} = \frac{\mu_{max}[CO_2]}{K_{CO_2}+[CO_2]} \qquad (35)$$

where

$$[CO_2] = [CO_2]*[1 - exp(-k_L at)] \qquad (36)$$

where $[CO_2]$ is CO_2 concentration in bulk fluid, $[CO_2]*$ is solubility of CO_2 in the fluid, and $-k_L a$ is the overall mass transfer coefficient. Eq (35) gives the microalgae growth due to CO_2 aeration. As mentioned in Lopez-Rosales et al (2017), rising bubbles do not cause significant microalgae death rates, so this work ignores microalgae death due to bubbling.

Following up from our previous work on microalgae growth and death rate with centrifugation, the following differential equation is proposed.

$$A^{-1}\frac{df}{dt} + {\mu_{app}}^{-1}\frac{df}{dt} = f \qquad (37)$$

The first term of (37) is the normal growth rate of microalgae in Hondzo et al (2006), and the second term corresponds to the growth rate of microalgae due to carbon dioxide aeration, and hence the positive sign. Rearranging (37) gives

$$\left(A^{-1}+\mu_{app}\right)\frac{df}{dt}-f=0 \qquad (38)$$

We shall determine μ_{app} from experiments, and hence solve equation (8) to give a relationship between the growth rate of microalgae and the bubbling parameters.

For a minimal death rate due to stirring, equation (38) is solved to give

$$f(t)=e^{\mu_{app}t}+c \qquad (39)$$

where c is a constant. Equation (39) fits the experimental results, which are presented in Figure 17.

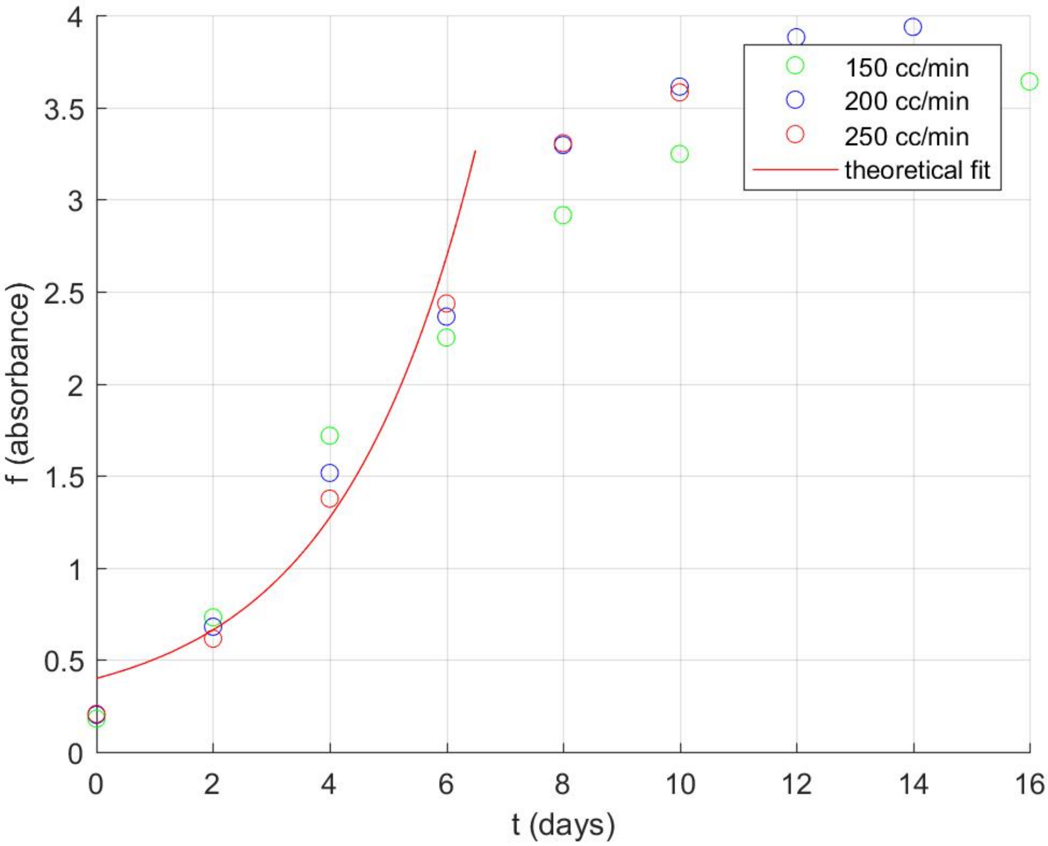

Figure 17. Fitting of theoretical results with experimental results.

Figure 17 shows that the theoretical result agrees with the experimental results for regions of graphs with accelerated growth. Values of parameters obtained from graph: $c=$

$-0.58, \mu^{app} = -1.662$, c is dimensionless constants to balance the choice of units, μ^{app} is in day^{-1}.

This is because the theoretical result does not consider the reduction in growth rate due to light blockage when the biomass reaches a critical value. In addition, based on the graph, it can be deduced that the specific microalgae growth rate is approximately 0.42.

The increase in biomass concentrations from 150 to 200 cc/min was due to increased mass transfer rates between the nutrient medium and FSP-E cells. Higher bubbling rates induced greater turbulence and circulation within the cultivation medium, allowing more contact between nutrient particles and FSP-E cells, thus increasing the nutrient intake rate by FSP-E. However, there was a drop in microalgae concentration when the bubbling rate is increased to 250 cc/min. One of the reasons for this was probably due to the mass transfer limitation, whereby the nutrient intake by FSP-E cells reached its saturation, whereas excessive nutrient supplies could not be absorbed by FSP-E cells for growth. The increased bubbling rate had reduced the bubble sizes, significantly increasing the surface-to-volume ratio between the gas bubbles and the microalgal cells. Moreover, a high bubbling rate indicated that the bubbles move up the column faster because of the increased fluid velocity. These factors reduced the contact time between gas bubbles and microalgal cells, resulting in lower mass transfer and thus lower microalgal growth rate. Furthermore, Sandesh (2016) reported that an increased bubbling rate would hinder cell growth by foaming, thereby hindering the mass transfer between gas bubbles and microalgal cells. The inclusion of stirring within the system also reduced the bubbling size at the bottom of the column before moving up the column (Walls *et al.*, 2017). These results explained why the biomass concentration increases when the bubbling rate increases from

150 to 200 cc/min, whereas at 250 cc/min, it can be explained that the impact of foaming due to the high bubbling rate has hindered the mass transfer, resulting in lower biomass production (Sandesh *et al.*, 2016).

5.4.2 Total protein content in microalgae

The total protein concentration of FSP-E exhibited an increasing trend. For example, the protein concentration decreased from 0.577 mg/mL at 150 cc/min to 0.553 mg/mg when the bubbling rate was increased to 200 cc/min. A spike in protein concentration was observed when the stirring speed was increased from 200 cc/min (0.553 mg/mg) to 250 cc/min (0.640 mg/mg). Raw data for the protein absorbance and fractions were list in Table S32-S33.

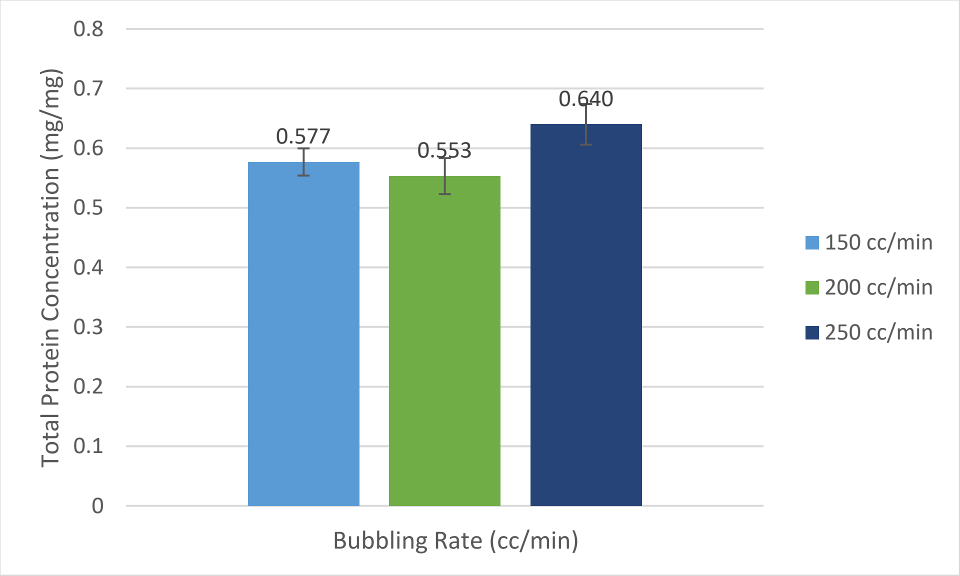

Figure 18. Total protein concentration at different bubbling rates

The total protein content did not show a similar trend to that of the microalgal growth graphs, nor did the biomass concentration showed a similar trend with the bubbling rate. Even though the increase in bubbling rate form 200 cc/min to 250 cc/min showed a decrease in biomass concentration, it was noticed that the fact that a lower mass transfer rate due to a larger surface-to-volume ratio for the gas bubbles, as well as the reduction of contact time, did not affect protein production and assimilation within the microalgal cell. Protein production was not affected by these factors.

5.4.3 Total carbohydrate content in microalgae

The total carbohydrate concentration graph showed similar trends to the microalgal growth and biomass concentration graphs. The total carbohydrate concentration for FSP-E showed a decreasing trend from 150 to 250 cc/min. For example, the carbohydrate concentration fraction decreased from 0.087 to 0.077 mg/mg before reaching 0.068 mg/mg. Raw data for the carbohydrates absorbance and fractions were list in Table S34-S35.

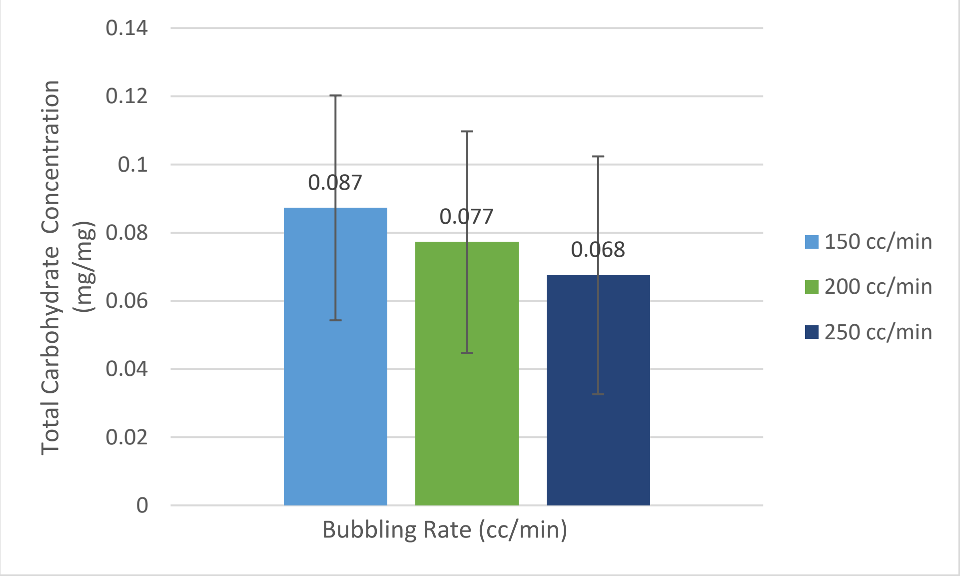

Figure 19. Total carbohydrate concentration at different bubbling rates

The total carbohydrate concentration from 150 to 250 cc/min showed a decreasing trend with increasing bubbling rate. In other words, carbohydrate production reached saturation at 150 cc/min, and further increases in the bubbling rate lead only to decreased carbohydrate concentration. A further increase in the bubbling rate to 250 cc/min led to a drop in the carbohydrate concentration. After 200 cc/min, the bubble size reached a certain extent at which the surface-to-volume ratio of the gas bubbles dropped significantly. Moreover, a high bubbling rate indicated that the bubbles move up the column faster because of the increased fluid velocity. These factors reduced the contact time between gas bubbles and microalgal cells, resulting in lower mass transfer and carbohydrate production.

5.4.4 Conclusion

Combining bubbling and stirring in a single system for microalgae cultivation still requires more research on whether the system is feasible to operate at a larger scale. Even though the stirring motion in this case creates turbulence, reducing the gas bubble sizes and allowing better contact for mass transfer, the stirring motion in an industrial-scale microalgae cultivation plant would require a large impeller, which would require high electrical energy consumption. This would increase the operating costs of microalgae cultivation. The inclusion of different bubbling rates affected microalgae growth. The increased bubbling rate indicates greater air bubbles in contact with the microalgal cells. On the other hand, it also increases gas bubble velocity as the column moves, reducing the possible contact time between gas bubbles and microalgal cells. The biomass mass increased when the bubbling rate increased from 150 to 200 cc/min (5.229 g/L to 5.913 g/L). For total protein case, there was a slight increase when the bubbling rate increases from 150 cc/min to 200 cc/min (0.577 mg/mg to 0.553 mg/mg), followed by an increase up to 0.640 mg/mg at 250 cc/min. The increase in the bubbling rate did not show a similar trend for the carbohydrate concentration, whereby the impact of the reduction of gas bubble contact time was not overcome by the increased substrate used for the microalgal growth, and the total protein concentration increased with the bubbling rate. Considering that the impact of the bubbling rate was noticeable at 150 cc/min, where the increase in biomass and total protein concentrations is considerably more significant, it was possible to deduce that the optimum bubbling rate for microalgae cultivation is 150 cc/min.

5.4 Cell disruption at different stirring speeds

The introduction of stirring motion into the system caused some disruption. The microalgal cells were generally intact for cultivation without stirring (control). However, with an increase in the stirring speed from 360 to 420 rpm, the impact of the motions was seen to have disrupted the microalgal cells, causing some cells to be slightly damaged and completely disrupted.

When the stirring speed increases, it was observed (see Figure 20) that there are some irregularities in the outer layer of the microalgal cells. The cell wall in microalgal cells maintained the shape of the cells while preventing the intracellular contents from being exposed and leaked to the outer surroundings (Zanette *et al.*, 2019). The irregularities (which is circled in red) in Figures 20A-D which were observed at stirring speeds 360 rpm to 420 rpm show a trend in increase of irregularities as stirring speed increases. Relatively more damaged cells were observed at 420 rpm than at other stirring speeds. The stirring motions were strong enough to damage biomass production and protein and carbohydrate concentrations. The irregularities observed in microalgal cells are possibly due to the breakdown of the cell wall. It was noticed that the biomass concentration and carbohydrate concentration showed a considerable drop when the stirring speed increased from 360 rpm to 420 rpm, from 6.1568 g /L to 5.2290 g/L and from 0.117 mg/mg to 0.087 mg/mg, respectively. This is supported by SEM imaging, which showed that microalgal cells cultivated at 420 rpm were more damaged than those cultivated at 390 rpm.

Furthermore, the microalgae cultivated at 360 rpm and 390 rpm achieved maturity on day 12, whereas the microalgae cultivated at 420 rpm achieved maturity on the 14th day. These observations indicated that longer stirring exposure and greater mechanical stress are imposed on the cells of microalgae cultivated at 420 rpm. Hence, this led to more severe cell disruption compared to that at other stirring speeds.

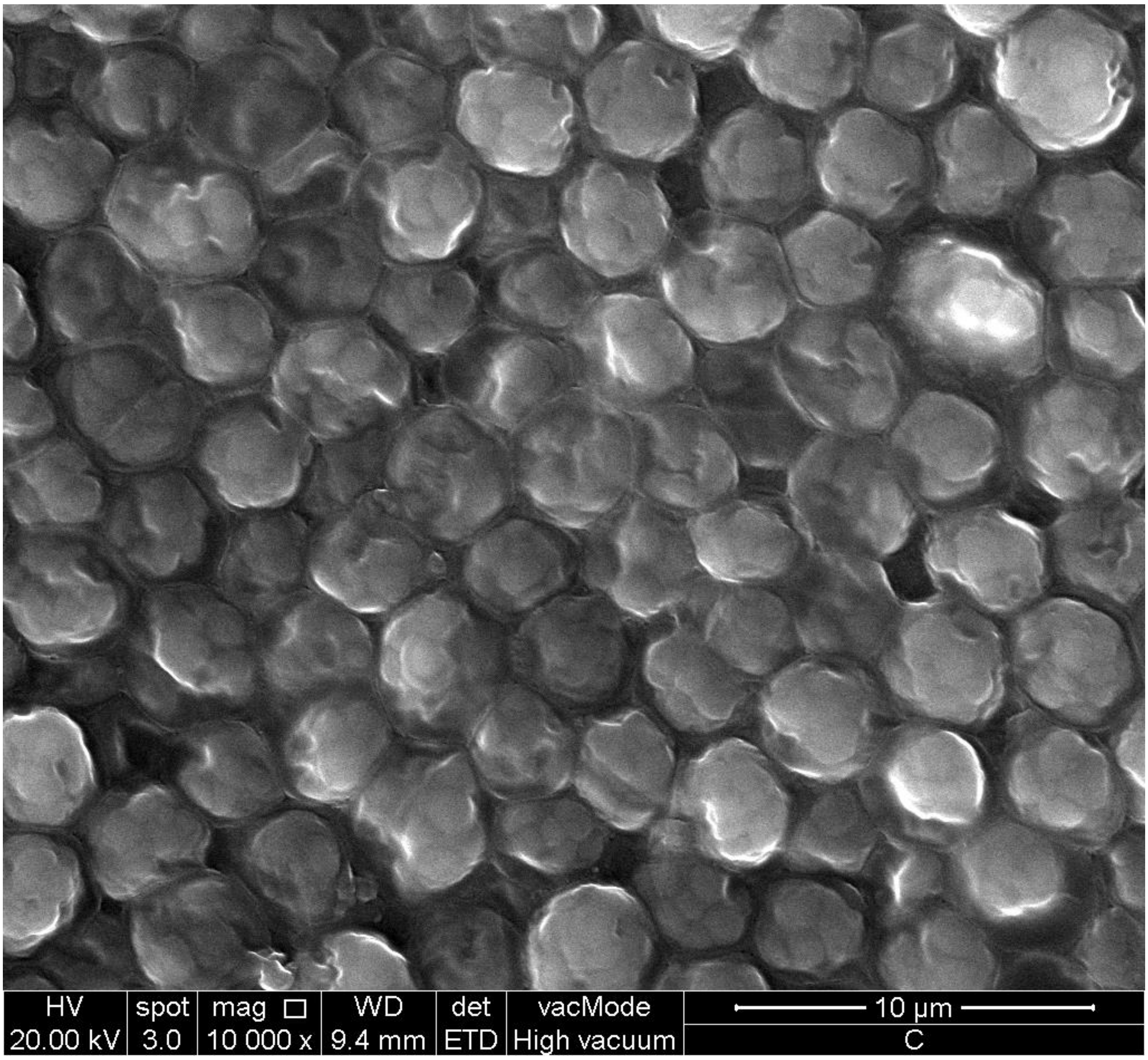

Figure 20A. SEM imaging of FSP-E cells cultivated under 0 rpm

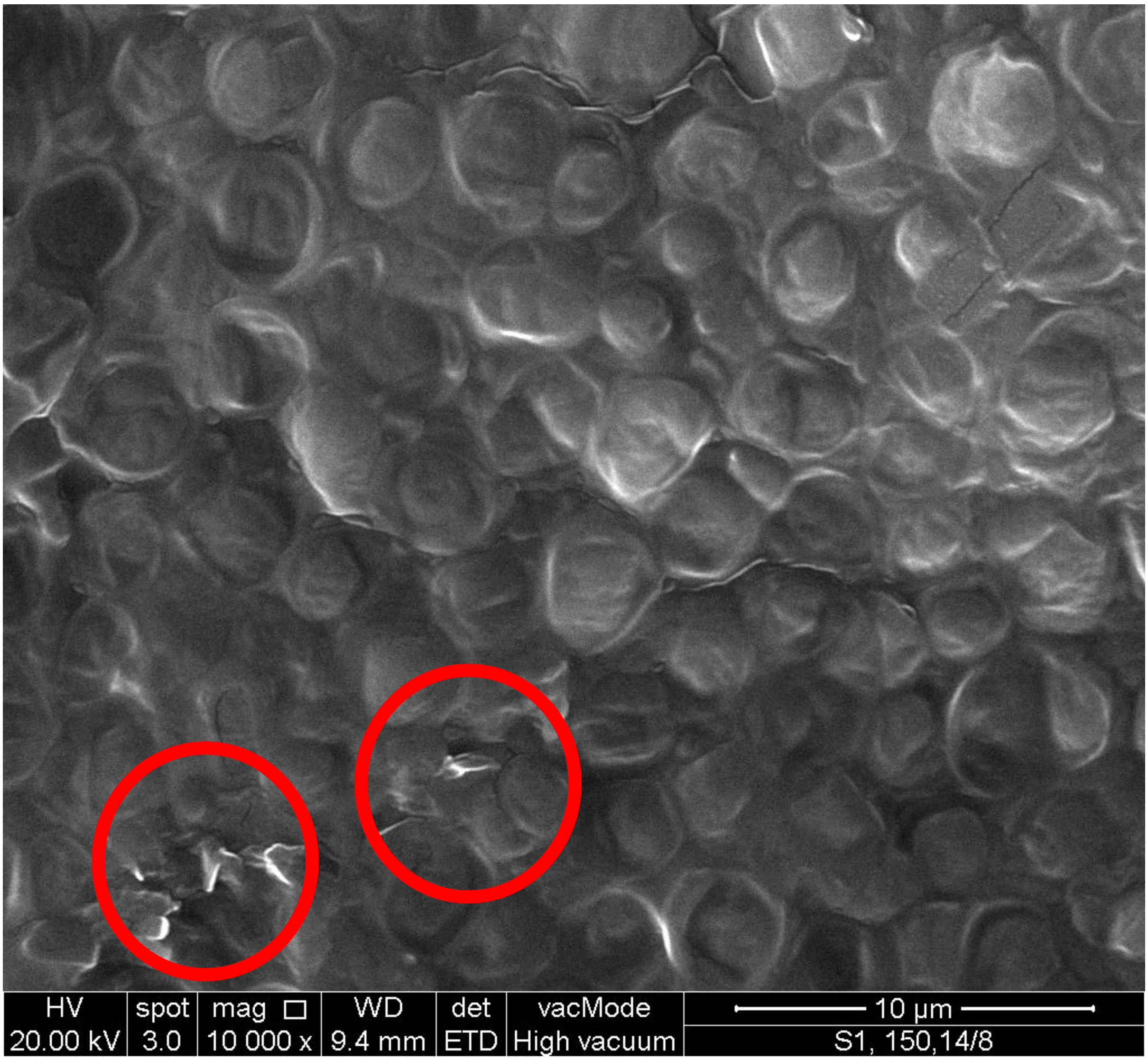

Figure 20B. SEM imaging of FSP-E cells cultivated under 360 rpm, the image circled in red is the damaged cells

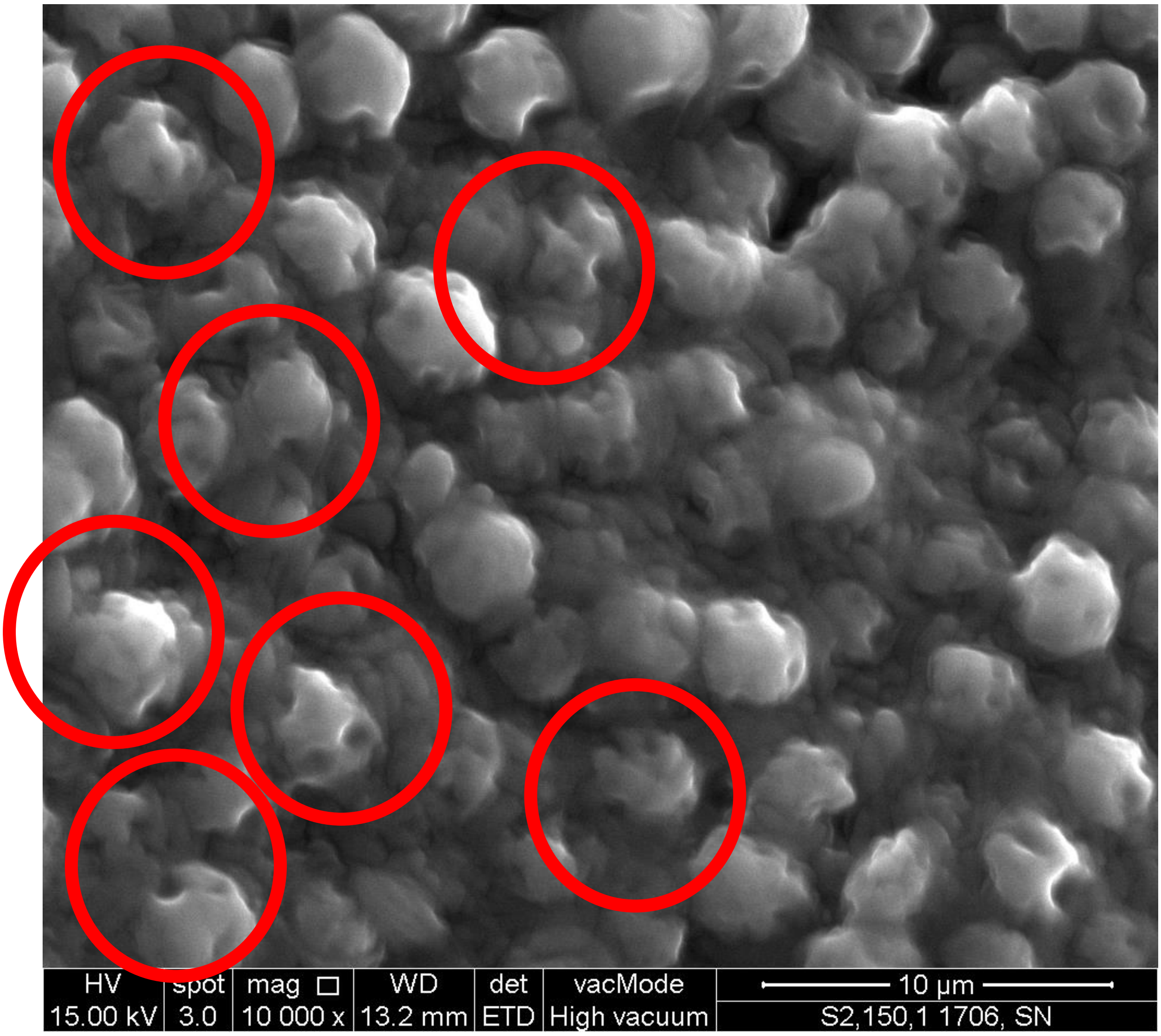

Figure 20C. SEM imaging of FSP-E cells cultivated under 390 rpm, the image circled in red is the damaged cells

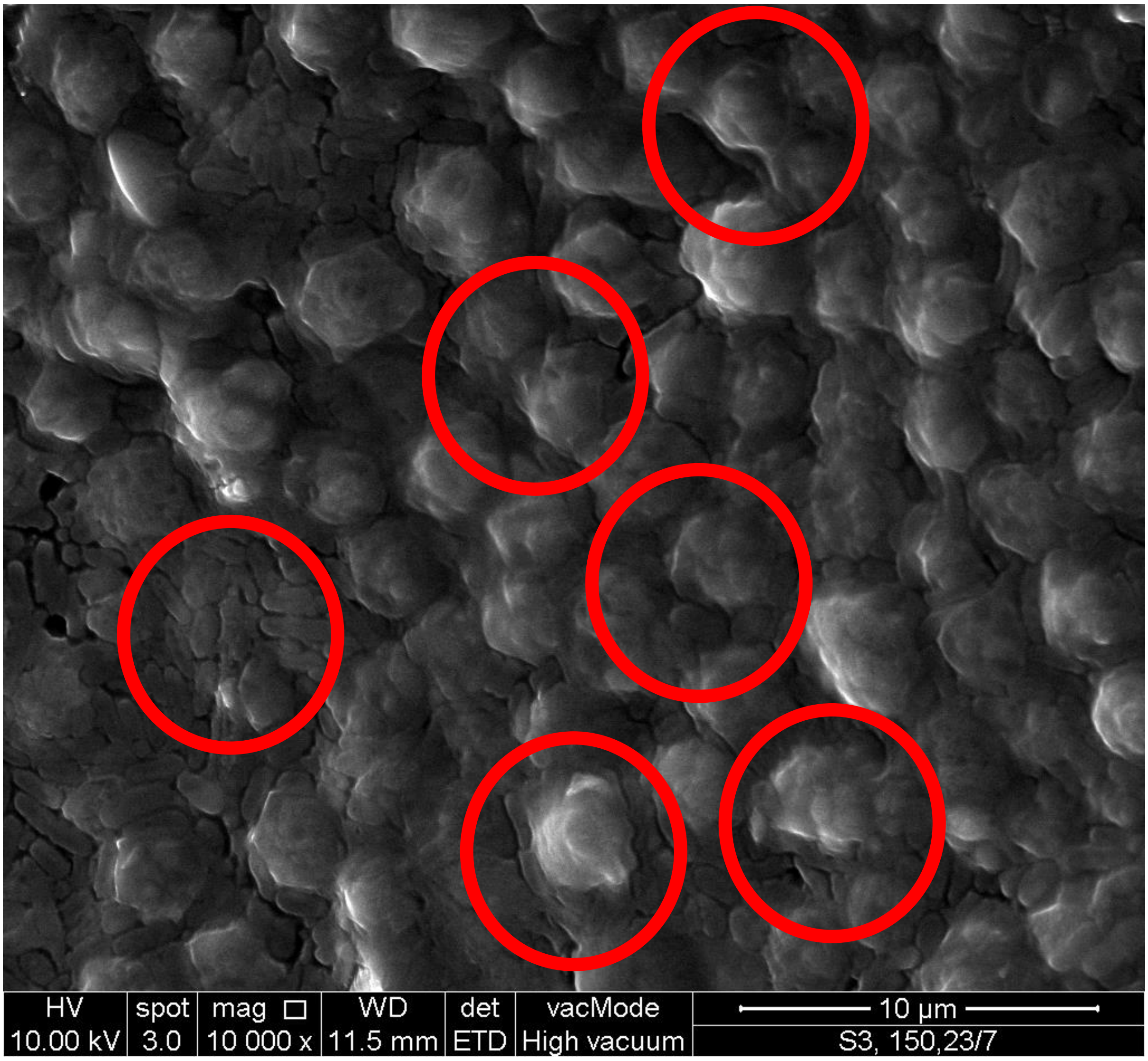

Figure 20D. SEM imaging of FSP-E cells cultivated under 420 rpm, the image circled in red is the damaged cells

These can mainly be broken down into three main types of damage due to ROS generation: oxidation damage and antioxidant defence mechanisms within the microalgal cells (Ali, Tyagi and Bae, 2003). Lipid peroxidation by ROS through hydrogen removal formed unsaturated chains of fatty acids that formed the membrane of microalgal cells and caused oxidation damage. For example, the ROS synthesised through lipid peroxidation were typically cytotoxic products such as malondialdehyde (MDA) and aldehydes, which were highly reactive and caused damage, especially to chloroplasts, which consist of polyunsaturated fatty acids-rich membranes. Moreover, ROS generation from mechanical stress also causeD protein oxidation. Disulfide bonds formed through ROS generation upon the formation of sulfur-containing amino acids altered their functions and led to changes within the protein structure. These changes then caused cellular dysfunction, which changed cell function. Furthermore, the generation of hydroxyl radicals through ROS caused DNA alterations, in which thymine and guanine in DNA can be hydroxylated and degraded, thereby impacting cell functions.

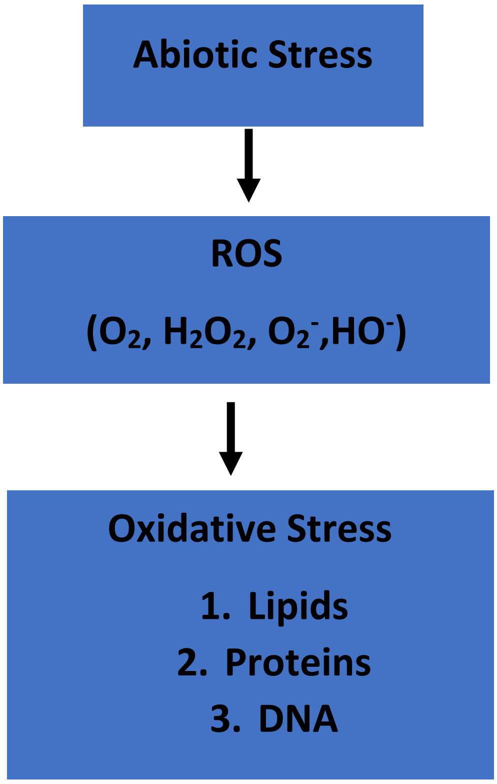

Figure 21. ROS-induced oxidation damage

5.5.1 Conclusion

The inclusion of stirring in the system disrupted microalgal cells. The stirring motion was seen to have exerted mechanical stress on the cells, causing cell irregularities. The increase in the stirring speed was seen to cause more severe damage to the cell, where cell damage was the highest when the stirring speed was at 420 rpm. On the other hand, this was very much in line with the biomass obtained at different stirring speeds. These results showed that mechanical stress imposes physical damage to microalgal cells, hindering cell growth. Moreover, these lowered microalgal cell growth can be coupled with the internal damages that are deduced due to possible oxidation damages with the ROS generation, as confirmed by Ali, Tyagi and Bae (2003), Lau et al. (2022a) and Rezayian, Niknam and Ebrahimzadeh (2019).

CHAPTER 6

UPSCALED FSP-E CULTIVATION SYSTEM

6. Upscaled FSP-E Cultivation System

Since the optimum stirring and bubbling conditions were obtained from previous experiments, it was unclear whether the biomass productivity could be emulated in a larger PBR system. Thus, a pilot upscaled PBR for FSP-E cultivation was required.

6.1 Design of large-scale photobioreactor

The purpose of a large-scale photobioreactor was to cultivate microalgae in larger volumes to increase the quantity of biomass obtained. The photobioreactor was designed based on a laboratory-scale photobioreactor typically cultivated in Schott bottles of different sizes. However, the sizes of the Scott bottles were only between 50 and 5 L, and their opening was relatively small and only able to accommodate a magnetic stirrer to impose stirring motion. The upper limit for magnetic stirring was relatively low (approximately below 650 rpm); thus, to run a combination of cultivating and harvesting in a single column, an additional overhead stirrer with a larger stirring range is required. In this case, the top opening of the photobioreactor must sufficiently be large enough to allow the stirring blade to be inserted.

6.1.1 Types of closed-system photobioreactor

There were several different types of photobioreactors, and the most common were airlift, plate, and tubular reactors. They often used airflow to generate turbulence to move microalgal cells, nutrients, and air around the culture medium, allowing great contact between them. To duplicate similar results from a smaller laboratory-scale photobioreactor on a larger scale, a similar photobioreactor must designed based on such results. Tubular photobioreactors were considerably identical to laboratory-scale photobioreactors; thus, the design of a customised photobioreactor must be able to duplicate similar results to laboratory-scale photobioreactors.

6.1.2 Common photobioreactor designs

Existing photobioreactors were typically correlated with each other. A tubular airlift photobioreactor was the shorter version of a tubular reactor, whereas a flat-plate photobioreactor was an airlift photobioreactor design with a thin plate instead of a tubular shape. These photobioreactors had distinctive features. For example, a tubular photobioreactor generally consisted of long tubular columns with small diameters arranged in different configurations (i.e. multiple bends, long straight or spiral tubes). These features created a larger surface area for light illumination and greater cultivation volume. An aeration system was used to induce turbulence in the cultivation media by circulating it within the system. The diameters of these PBRs were typically small and are between 10 and 60 mm, whereas the lengths were usually up from a few metres to several hundred metres (Huang *et al.*, 2017). However, tubular PBRs were limited to outdoor cultivation and sunlight illumination due to their long tubes. Moreover, these PBRs usually had larger diameters to accommodate larger cultivation volumes, leading to light illumination variation between the tube's centre and other parts, thereby restricting microalgal growth. Long tubes also indicated higher CO_2 and O_2 concentration differences between the entry and end parts of the tube, leading to fluctuating growth at both ends. The cleaning for this kind of PBR proved to be difficult because of the long tubes, and manual cleaning was insufficient to remove the residues for the next batch of experiments.

Figure 22. Tubular photobioreactor *(Posten, 2012)*

An airlift photobioreactor generally comprised of a tubular column with a height of less than 4 m and a diameter of less than 0.2 m (Huang *et al.*, 2017). The column height was limited to 4 m for structural reasons, as the strength of transparent materials was to be considered (Huang *et al.*, 2017). The airlift PBRs consisted of a gas sparger or orifice at the bottom of the column. This created aeration at the bottom of the column, inducing turbulence within the cultivation medium and circulating nutrients, air, and microalgae. This resulted in better contact between them, allowing greater mass transfer and promoting microalgal growth. In some cases, a draft tube was installed at the centre of the airlift PBR, allowing the gas bubbles to move up from the bottom through the draft tube, before circulating down upon exiting through the outside of the draft tube. This provided better fluid circulation than those without draft tubes.

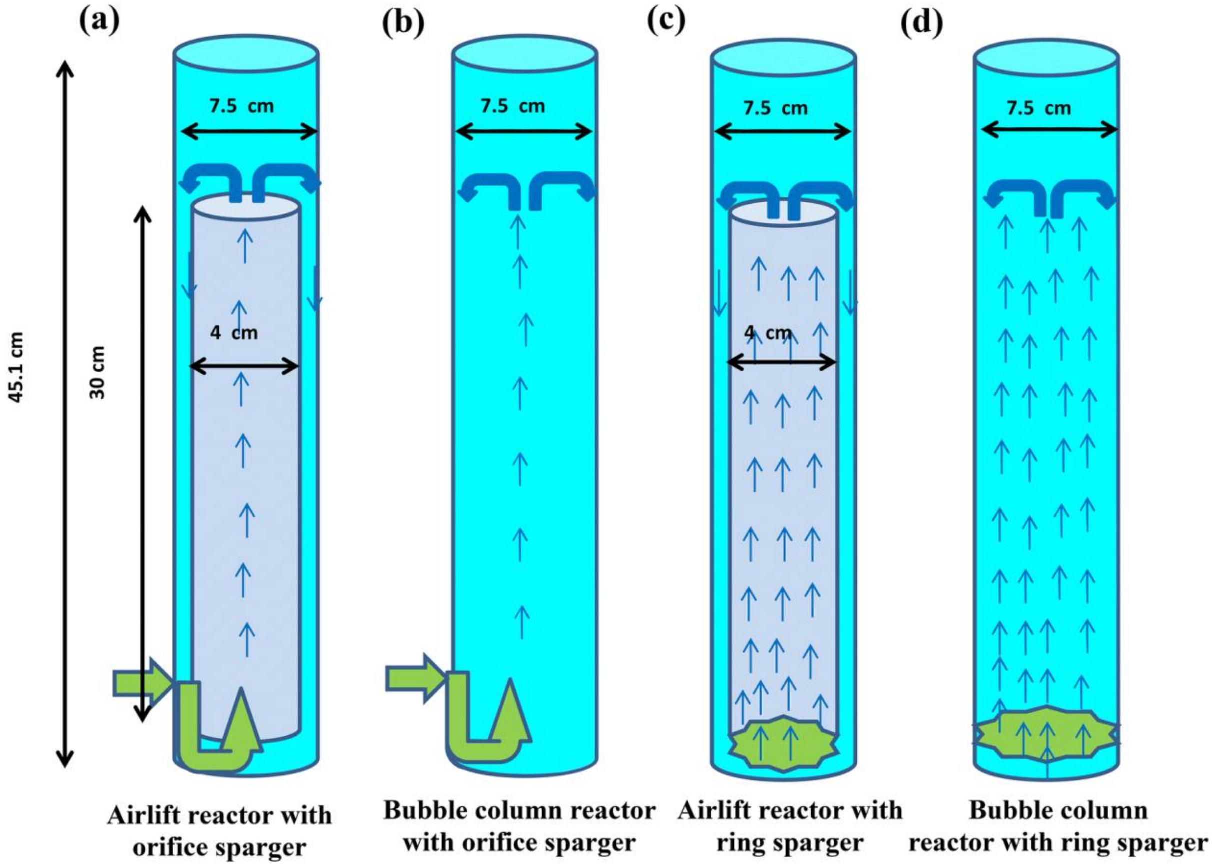

Figure 23. Airlift photobioreactor *(Banerjee* et al.*, 2020)*

Lastly, a flat-plate photobioreactor was a PBR that operates within a thin-plate layer. Some flat-plate PBRs consisted of a gas sparger located at the bottom of the flat plate, generating gas bubbles to create turbulence and circulation for the cultivation systems, while others had gas spargers installed vertically at the side of the flat plate. Additional baffles were also seen to be included in these PBRs to disrupt the free flow of the gas bubbles, thereby inducing greater fluid turbulence and enhancing fluid circulation. This type of PBR had advantages for both airlift PBRs and tubular PBRs. The larger surface area-to-volume ratio provided better exposure to light illuminations, allowing more uniform microalgal growth. In addition, the thin flat plate allowed better temperature control, where the high temperature at the plate surface due to light irradiation that was controlled by spraying water to lower the temperature. The well-defined circulation by flat-plate PBRs allowed a higher gas-liquid mass transfer rate through good mixing by fluid circulation. The high ratio of riser to downcomer surface area with a volume as high as 200 L helped to avoid cell sedimentation, clumping, and fouling on the illuminated PBR walls with high culture velocity (Huang *et al.*, 2017).

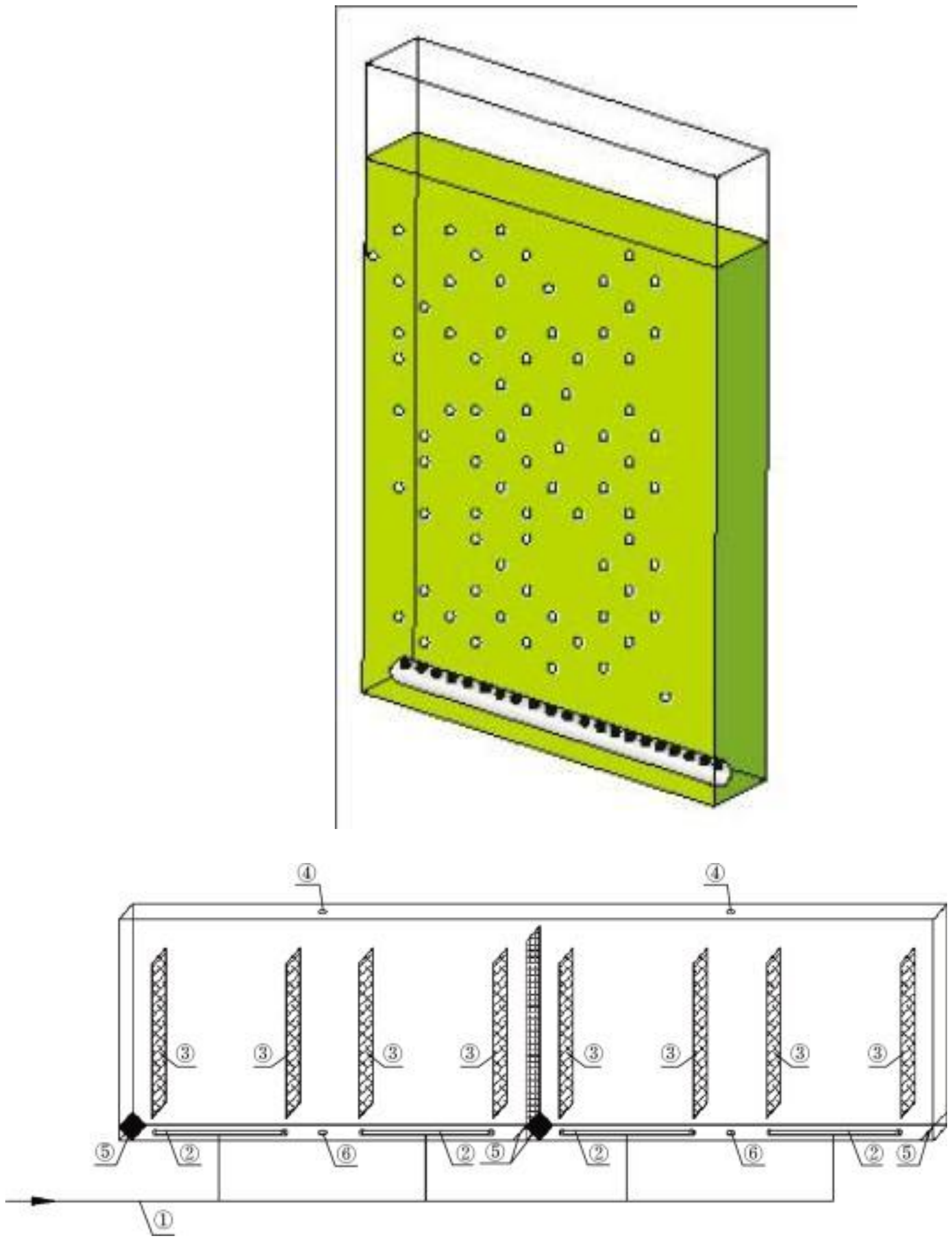

Figure 24. Flat-plate photobioreactor *(Posten, 2012; Huang* et al.*, 2017)*

6.1.3 Column design selection

To replicate a cultivation system similar to that of laboratory PBRs, the designed PBR must be identical in structure to laboratory PBRs. Since an overhead stirrer was to be included in the system, the PBRs must be able to allow the stirring motion to be performed smoothly, and the top of the opening must be large enough to insert the stirring blade. Current laboratory-scale PBRs ran at a cultivation volume of 1 L per batch, and it is suggested that scaled-up PBRs must be able to run five times the volume of the laboratory-scale cultivation volume, which is 5 L. The selection of the column material was based on material transparency, cost, and durability; thus, only glass and acrylic glass were considered at this stage. However, based on consideration of all three factors, the high durability and light weight of acrylic glass proved to be better than glass as a column wall material (Hagendijk, 2015). Even though the maximum limit for the column diameter of airlift PBRs was around 0.2 m, the inclusion of stirring motion within the system allows better circulation within the column than general airlift PBRs; thus, the diameter for the designed column was set at 0.2 m. The column height must not be too high to run the cultivation and perform cleaning easier. The column was set to run with a maximum operating volume of 10 L to allow future applications. Therefore, the actual total volume of the column was designed 30 % above the 10 L maximum operating volume (approximately 13 L). The standard cylinder volume formula is,

$$V = \pi r^2 h \qquad (40)$$

Where V is the total volume of the cylinder (m^3), r is the radius of the cylinder (m), and h is the height of the cylinder (m). Rearranging equation 40 will give,

$h = \frac{V}{\pi r^2}$ (41)

Thus, rounding off this value gave a cylinder height of approximately 0.45 m. The wall thickness of the cylinder was chosen based on the minimal thickness (3 mm) available for a given diameter of 0.2 m by the supplier. Two additional outlets were included at the bottom of the column to ease the collection of samples and for draining purposes.

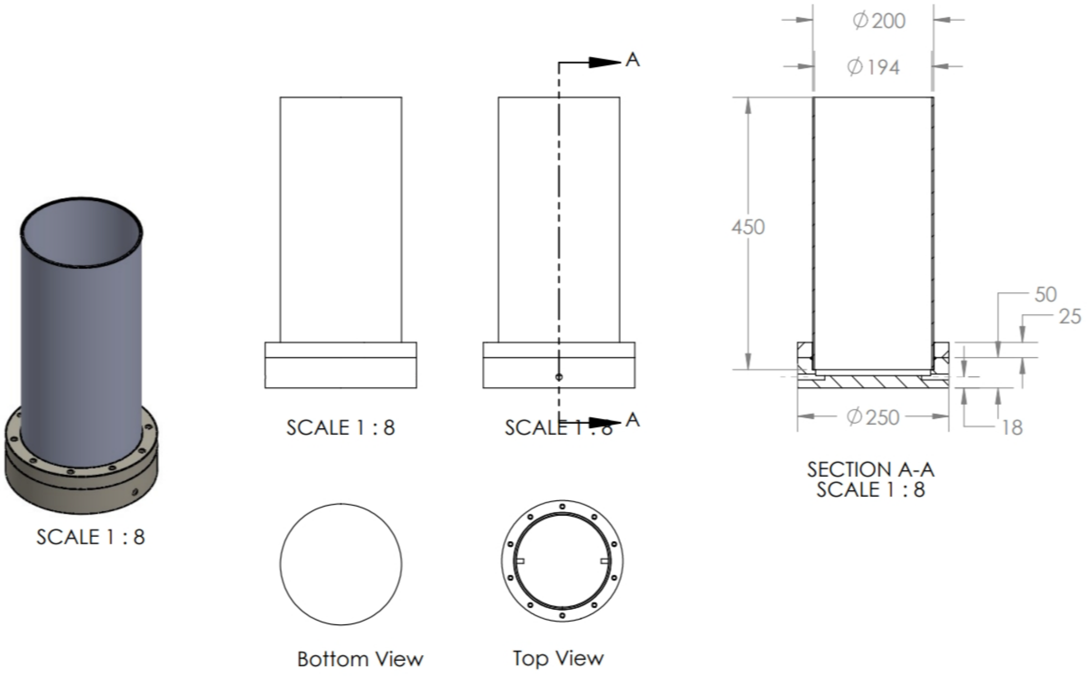

Figure 25. Designed photobioreactor

6.2 Operating conditions for the designed PBR

Based on the conducted experiment, the following optimum operating conditions were established:

1. The stirring speed should be between 360 and 390 rpm, consistent with the literature.

2. Bubbling rate should be set at 15 % of the total volume of the cultivation system.

To better imitate upscaled industrial microalgae cultivation and to ease better control of the stirring speed, the stirring speed for upscale cultivation was set at a rounded value of 350 and 400 rpm. Figure 26 showed the setup of the upscale cultivation system.

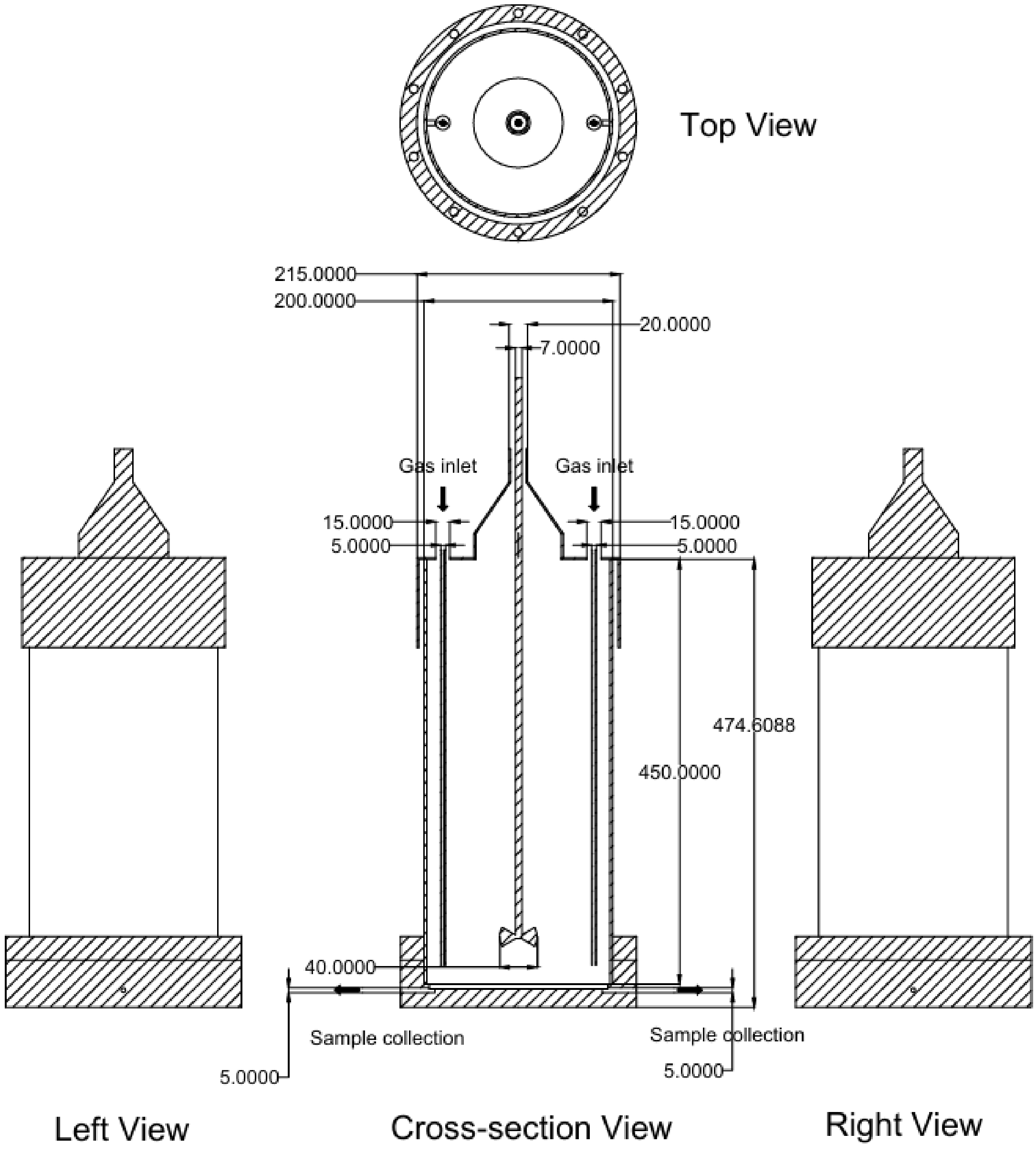

Figure 26. Upscaled cultivation setup

6.2.1 Results and discussions

The FSP-E cultivation at 350 rpm and 750 cc/min matured at an absorbance range of 1.6–1.8, whereas the cultivation at 400 rpm and 750 cc/min matured at an absorbance range of 1.4–1.6. These values align with the biomass obtained where the average biomass weight for 350 rpm and 750 cc/min is 28.920 mg and 26.801 for 400 rpm and 750 cc/min, respectively. Raw data for the absorbance curves were list in Table S22-S27.

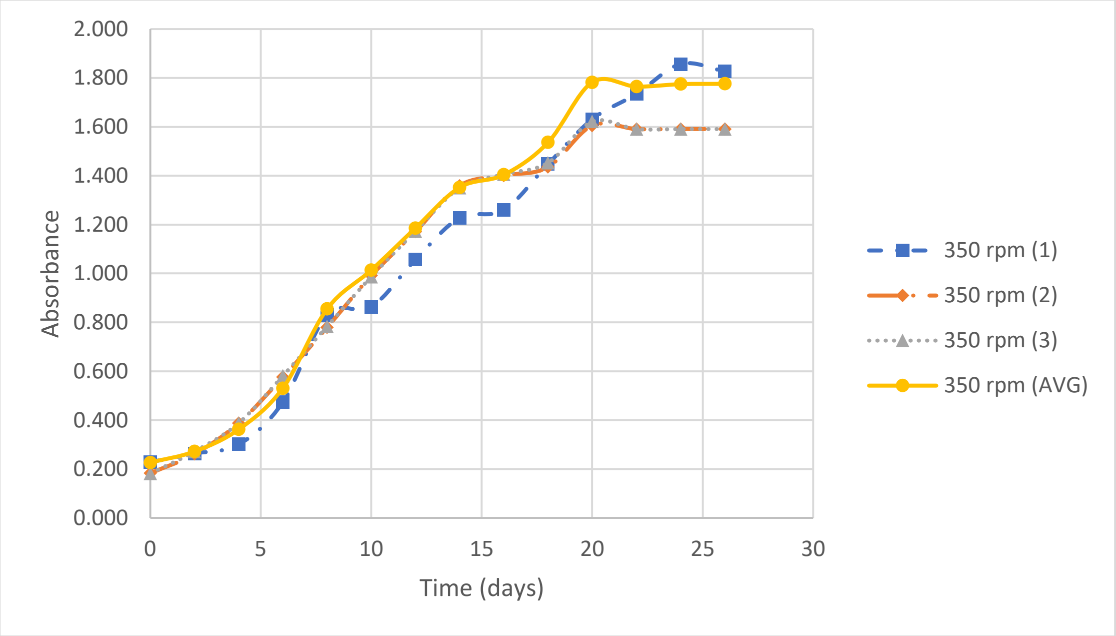

Figure 27. Microalgae absorbance over 26 days

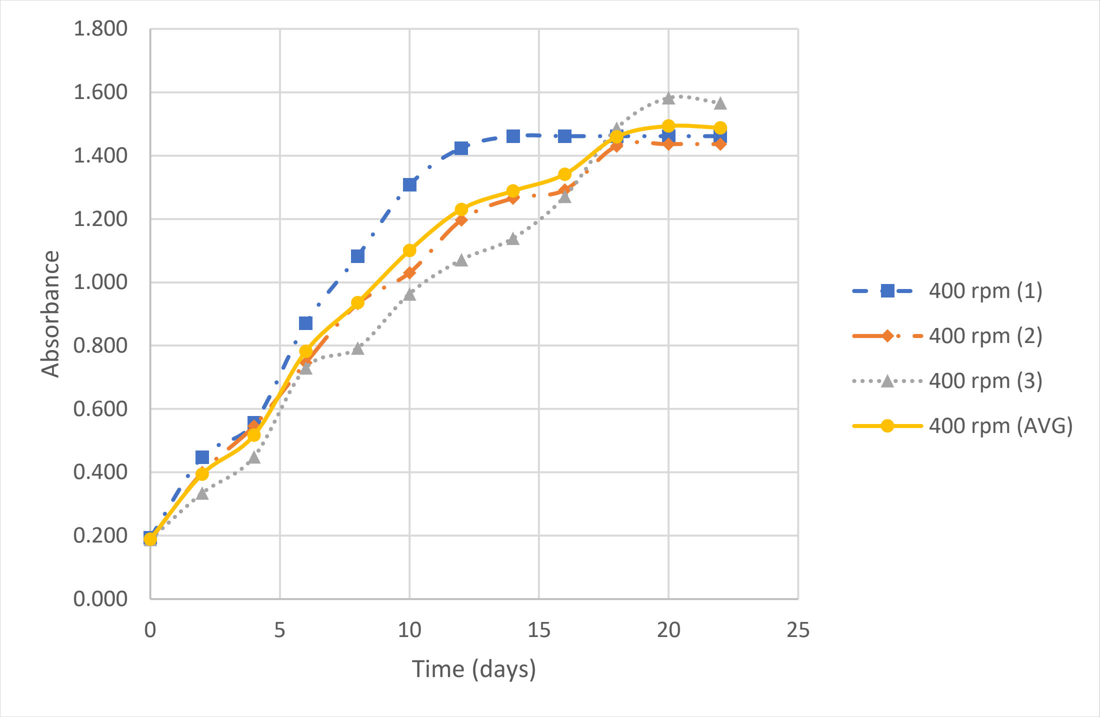

Figure 28. Microalgae absorbance over 22 days

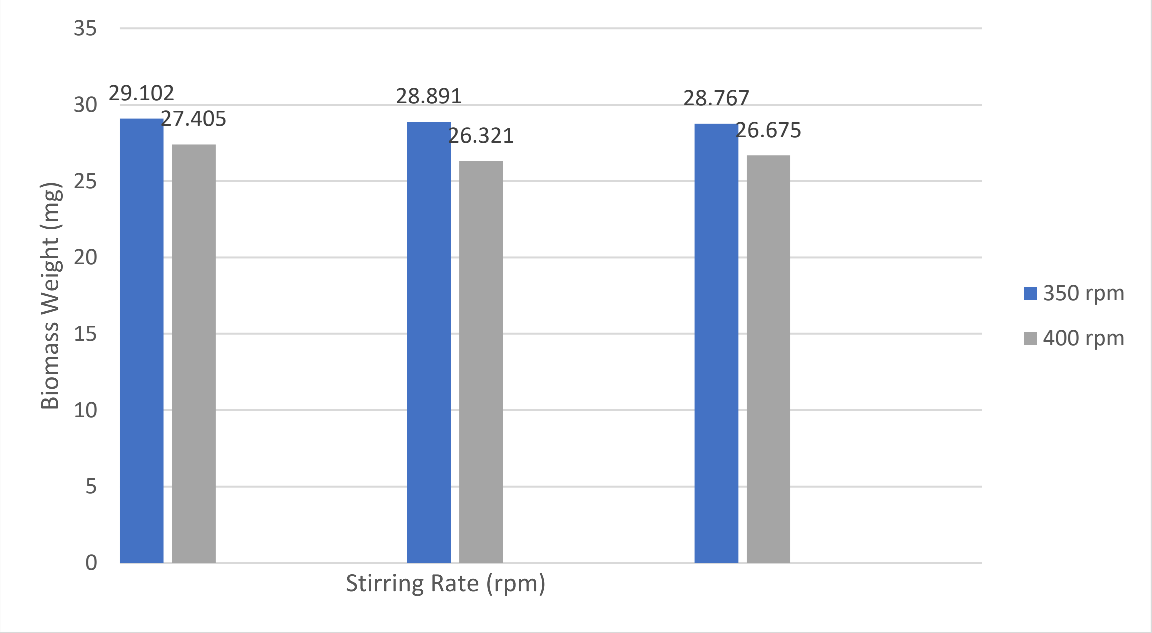

Figure 29. Biomass weight at different stirring speeds

Moreover, the protein and carbohydrate contents were lower at 350 rpm than at 400 rpm, which agrees with the experiment conducted in section 5. Although the carbohydrate and protein mass fractions at 350 rpm were lower than those at 400 rpm, the actual mass for both contents was still higher at 350 rpm than at 400 rpm. The biomass mass was approximately five times the biomass produced under 1 L PBR.

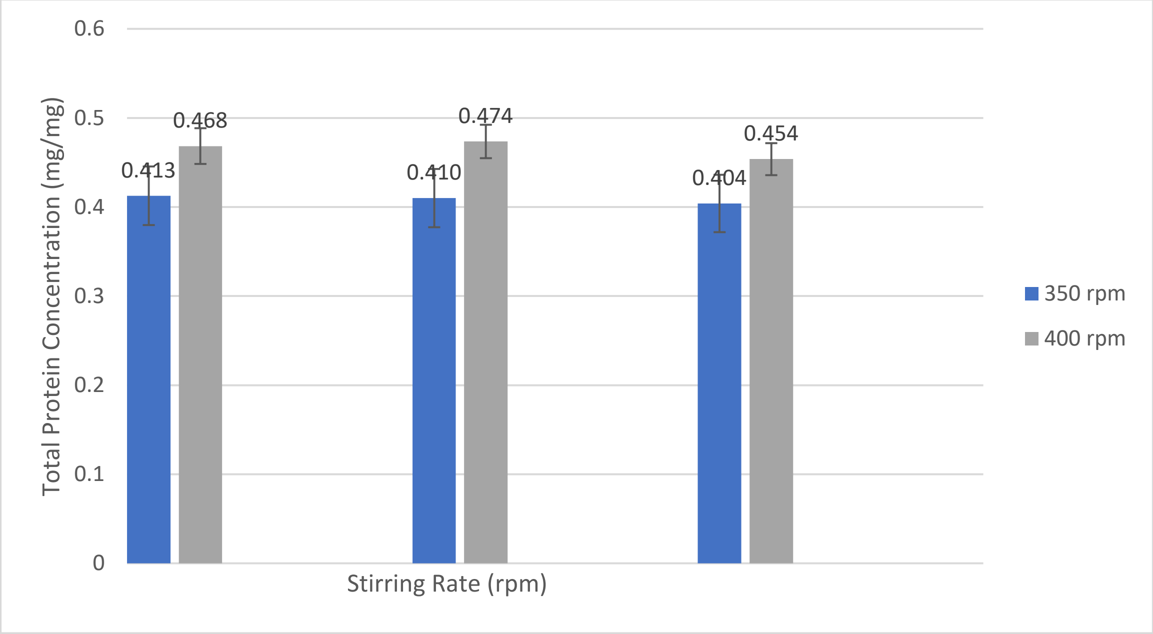

Figure 30. Protein concentration at different *stirring speeds*

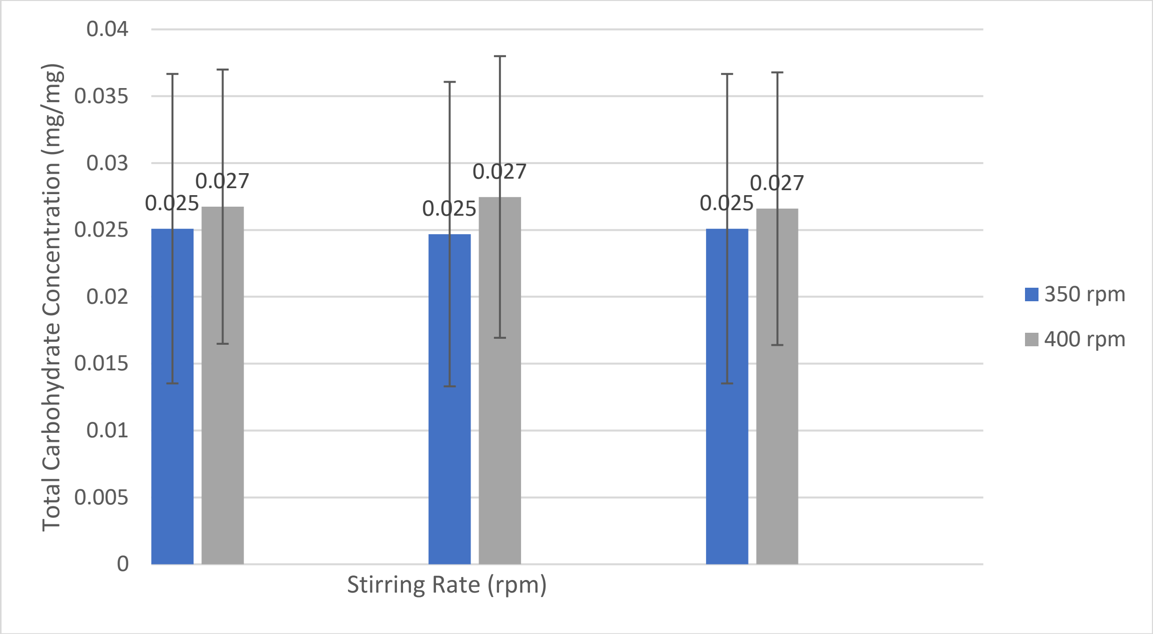

Figure 31. Carbohydrate concentration at different stirring speeds

6.2.2 Conclusion

The purpose of the combined system with both stirring and bubbling mechanisms was to enhance existing microalgae cultivation systems. This strategy increased the yield and production of microalgal biomass with improved efficiency. The selected bubbling rate was set at 1.5% of the total cultivation volume, as determined by the experiment conducted in section 4. The stirring speed was set at a rounded-off value of 350 or 400 rpm to allow better control of the stirring within the system, imitating an industrial-scale system. The target of obtaining at least 5 times the biomass of the laboratory-scaled production under a similar cultivation period is studied. The results show that the upscaled cultivation was able to reach approximately 5 times the average biomass weight of a laboratory-scale photobioreactor (5.283 g/L to 27.860 g/L).

CHAPTER 7

PROPOSED IMPROVEMENTS FOR CURRENT MICROALGAE CULTIVATION

7. Proposed Improvements for Current Microalgae cultivation

7.1 Stirring and Bubbling in a Closed System

Stirring and bubbling in microalgae cultivation enable the integration of upstream and downstream processes within a closed system. This allows for more efficient microalgae cultivation and harvesting free of human intervention, translating into more efficient automation with minimal uncertainties in modelling and ML. The following sections focus on ML in the automation of microalgae cultivation.

7.2 Machine Learning (ML) in Microalgae Cultivation

The current section aims to categorise and summarise how machine learning has been used in microalgae cultivation. More detailed reviews have covered this topic under slightly different contexts, including in combination with the Internet of Things, multi-omics, AI in general, circular economy, and spectroscopy (Teng *et al.*, 2020; Liu, Zeng and Ren, 2021; Chen *et al.*, 2022; Helmy *et al.*, 2022; Lim *et al.*, 2022; Wang *et al.*, 2022).

In brief and rough terms, Machine Learning (ML) is a branch of Artificial Intelligence (AI) that attempts to emulate human intelligence by providing the machine with examples of “solutions”, typically embodied in the form of an offline dataset. ML is at the core of the modern AI revolution, especially in deep learning, a type of ML inspired by the structure and function of biological neural systems. This revolution manifests in the many applications that have achieved or surpassed human intelligence. This explains and justifies the significant interest that different industries have shown in ML, including the microalgae industry. An important point to consider in this context is that ML covers a vast array of algorithms and applies to an equally extensive and diverse set of problems. As such, and given limited space, it is infeasible to review these algorithms and applications thoroughly; instead, this section aims to categorise several key types of ML problems and briefly discuss some key microalgae-related works within each category.

ML approaches can be categorised according to different sets of criteria. Here we categorise approaches in terms of the high-level problems they are trying to solve, namely: (1) classification, (2) estimation and/or prediction, (3) control, and (4) analysis. The following sub-sections are structured along this categorisation.

7.3 Classification

ML approaches in this category are concerned with classifying entities into different discrete categories. Classification is arguably one of the most popular problems addressed by ML solutions. The microalgae domain can benefit from the automated classification of many other entities or states, e.g., the identification of microalgae species, and the determination of a cell's metabolic state.

The automated identification and classification of microalgae was recently achieved by Zhuo et al. (2022), by applying Linear Discriminant Analysis (LDA) and two different types of Support Vector Machines (SVMs) to polarised light scattering data. Thirty-five different categories of marine microalgae were successfully classified by a non-linear SVM with an accuracy of more than 80%. Despite the generally positive result, the authors suggest that given the diversity and complexity of marine microalgae, the classification problem is still challenging and requires further systematic comparison of ML approaches and large amounts of polarisation data to improve accuracy levels further.

Apart from species classification, many works have found it helpful to identify whether microalgae cells are dead or alive, since this parameter contributes useful information for improving cultivation processes. Reimann et al.(2020) compared explainable ML techniques, using fluorescence microscopy data, to classify *Chlorella vulgaris* cells into alive/dead categories, and found that random forests provided the best accuracy (i.e. 86%). The authors also experimented with the following ML techniques: naive Bayes, k-nearest neighbours, quadratic discriminant analysis, decision trees, adaptive boosting, and artificial neural networks. Wang et al.(2021) also experimented with ML techniques applied to the problem of identifying living/dead microalgae cells but instead used digital holography microscopy in a label-free approach. Overall, 12 different ML conditions were compared based on the following techniques: decision trees, discriminant analysis, logistic regression, support vector machines (SVMs), and k-nearest neighbours, where SVM conditions obtained the highest accuracy level (i.e. 94.8%).

The screening of cells can also be done in terms of their ability to produce different bioactive compounds such as lipids, proteins, luteins, and others (Lim *et al.*, 2022). For example, Guo et al. (2017) used machine learning to screen *Euglena gracilis* cells that exhibited a stronger ability to produce lipids. Moreover, the classification was done based on optofluidic time-stretch quantitative phase microscope data. The full pipeline included image segmentation, the extraction of 200 features from intensity and phase images, and an SVM for classification purposes, resulting in error rates as low as 2.15%.

7.4 Estimation and Prediction

The domain of microalgae cultivation involves many variables whose estimation and/or prediction are essential for monitoring different processes (e.g., pH and nitrogen concentration), maximising yield (e.g., biomass), minimising different kinds of issues (e.g., toxicity), and general decision-making. In ML terms, these problems typically fall into the general category of regression. The microalgae ML literature is rich with many examples of regression-based solutions.

Using decision trees, Noguchi et al. (Supriyanto et al., 2018) conducted early work on estimating microalgae growth rate in an open raceway pond from a subset of key environmental parameters (i.e. temperature and solar radiation). The model was built from a dataset based on a separate pilot plant, and obtained accuracy levels measured by a correlation coefficient of 0.89. Sakurai et al. (2019) described a neural network approach for estimating microalgae polycultures in an open raceway pond in a related paper. In Le-Thi-Thu et al. (2022), the authors used IoT and ML to predict microalgae biomass. Levasseur et al. (2021) conducted a meta-analysis, extracting key data and applying several ML algorithms (e.g. multilinear model and random forest) to determine the relationship between light regime and the growth of green microalgae. Salmi et al. (2022) used convolutional neural networks to estimate microalgae species and biomass, based on spectral images, thus contributing to automated biomass assessment. The estimation of microalgae cell concentration was also conducted based on spectroscopic information by Liu et al. (2021).

As can be extrapolated from the above papers, many other variables can be estimated or predicted. Hossain et al. (2022) used a modelling and multi-objective optimisation approach to investigate the impact of temperature, light-dark cycles, and nitrogen-phosphorus ratios on biomass productivity and CO_2 bio-fixation, both of which are key variables in microalgae cultivation. The estimation of CO_2 fixation was also studied by Kushwaha et al. (2023), through the adoption of an adaptive neuro-fuzzy inference system (ANFIS) and genetic algorithms. Chlorophyll content is another critical variable that can be estimated. Tang et al. (2023) estimated chlorophyll content in microalgae from colour models by adopting linear regression and artificial neural networks. Cell viability is another parameter that can be defined and estimated in different ways, including flow cytometry (2020). Here, the authors used label-free ghost cytometry (LFGC) coupled with machine learning, applied to cell morphology information, and succeeded in developing functionality on the quality control of cell products whilst avoiding the costs associated with labelling approaches that use antibodies/reagents.

As mentioned, estimating or predicting different variables can serve multiple functions. One crucial function involves estimating parameters for optimising various aspects of microalgae cultivation (e.g. biomass yield, combustion performance of downstream fuels, and others). The paper by Singh and Mishra (2022) provides a good example of this effort, where the authors evaluated the impact of different variables on the biomass yield of two microalgae classes, namely, Trebouxiophyceae and Chlorophyceae. The study was motivated primarily by optimising the efficiency of wastewater treatment and the efficacy of biomass production. Decision trees were used to estimate variables on wastewater treatment efficiency and biomass production, from different cultivation parameters (e.g. temperature, pH, CO_2 content, light intensity, and others), and this estimation ability was then used to achieve the above-mentioned optimisation goals.

Estimation problems are often easily converted into prediction problems, and vice versa; therefore, the efforts in one category tend to be relevant to the efforts in the other. Other examples of longer-term or larger-scale prediction problems in this area include biomass production forecasting and the prediction of environmental impacts (Handler *et al.*, 2012; Solimeno and Garc\'\ia, 2019).

7.5 Control

Control can briefly be defined as the problem of continually deciding how to act in the world, based on sensed dynamic conditions, to optimise some performance goal. From the ML perspective, the issue of control is most commonly associated with reinforcement learning (RL), which is concerned with mapping states to actions to maximise the expected long-term reward. In other words, in RL, an agent is concerned with learning how to act given that it finds itself in a particular state, in an environment which is typically complex and dynamic, to maximise its average long-term reward as a result of a proper selection of actions. This framework is helpful in microalgae cultivation since all of the key aspects of this domain (e.g. spectral information, paddle speed, and biomass growth) can be naturally interpreted as key elements of the RL framework (i.e., states, actions, and rewards).

Interestingly, in spite of almost one decade of deep reinforcement learning successes, whose beginning can arguably be marked by the achievements of AlphaGo, this approach to control has yet to be fully exploited in the microalgae cultivation domain (Silver *et al.*, 2016; Li, 2017). As an example of this pending opportunity, Zhu et al. (2022) report on a very interesting study in which they automate the speed of a mixing paddle in an open pond context, to maintain biomass yield whilst minimising the paddle's energy consumption. The mixing speed control was implemented via a programmable logic controller (PLC) based on sunlight intensity and culture temperature. Despite its early effectiveness, the solution reported in the paper has the potential to be improved further by adopting ML (and RL), as pointed out by the authors themselves.

Doan et al. (2021) have put forth one of the rare works on applying RL to microalgae cultivation. More specifically, the authors applied RL combined with Long Short-Term Memory (LSTM) recurrent neural networks to cultivate Spirulina sp. HH and as a result increased the biomass yield by 17% relative to more traditional methods. The state space of the solution was based on light levels as captured by BH1750 sensors, the action space consisted of 4 different actions (namely, (1) doing nothing, (2) closing a sunshade, (3) switching on a 200-W light, and (4) switching on a 300-W light), and the reward consisted of biomass dry weight. The specific RL algorithm consisted of a modification inspired by Q-Learning.

Given the scarcity of RL papers in the domain of microalgae cultivation, it is helpful to cross-reference RL applications in closely related areas, e.g. the control of microbial co-cultures in bioreactors (Treloar *et al.*, 2020a). The automated control of microbial cultures consisting of multiple species is in dire need due to the advantages afforded by these co-cultures, and the associated complexities of maintaining them. Treloar et al. (2020a) applied Neural Fitted Q-learning to maintain target population levels for different microbial sub-populations, and in the context of a simulated environment model. The state, action and reward spaces were based on microbial population sizes, the control of auxotrophic nutrient concentrations in the bioreactor, and the distance between current and target states, respectively. Although the paper demonstrates the usefulness of deep RL in controlling microbial sub-populations specifically in simulated bioreactors, it also provides strong support for the extrapolation to real environments, including those involved in microalgae cultivation.

7.6 Analysis

The analysis category subsumes the previous categories and includes additional approaches, resulting in the broadest and most varied category. The overall aim of works in this category is to use different ML techniques to generate novel insights and a deeper understanding of the systems under investigation. As such, it can include techniques on classification, estimation, prediction, control, clustering, outlier detection, and others, as they contribute towards generating new insights. The field of microalgae cultivation can significantly benefit from novel insights into the physical underpinnings of cultivation systems, from low-level genetics to high-level relationships between light regimes and growth dynamics, since these insights can be capitalised to optimise different aspects of the cultivation system (e.g. yield maximisation).

Helmy et al. (2022) provided a helpful review on how the combination of multi-omics and ML could bring the potential of microalgae as an alternative food source to fruition. The paper discusses how ML and other tools can contribute to the mining and analysis of multi-omics data to synthesise a more profound and hence more useful systems-level understanding of microalgae biology. For example, ML tools can be used to discover new relationships between transcriptome and protein structure information, and relationships between proteomics and metabolomics, which can then lead to insights and predictive capabilities, both of which can directly benefit cultivation processes. The paper also mentions how bio-simulation can be used to accelerate the progress of this scientific endeavour. At the same time, the usefulness of ML in simulations is increasingly being recognised in terms of increasing the speed and accuracy of simulations. Table 4 in the review paper by Teng et al. (2020) provides a very useful overview of the applicability of ML to many different types of microalgae cultivation tasks, including analytical ones on genome sequencing and gene editing.

7.7 Complexity

The scale of complexity of the photobioreactor must be kept at a minimum to ensure that the machine learning can concentrate on the analysis of the internal factors, such as temperature, pH level and light intensity, rather than external factors attributed to human interference and the environment. It would thus be ideal to have a fully enclosed system free from human interference and with little environmental impact. The enclosed environment allows the AI unit to simplify the model to exclude any external influences, making the analysis faster and more efficient. A plausible approach is to integrate the upstream with the downstream processes so that both processes occur in the same chamber to ensure the system is free from external influence. This helps to reduce the amount of uncertainty and helps make the models built by the AI unit more accurate.

The feasibility of the integration has been explored in one of our works (Treloar *et al.*, 2020b), where a model involves microalgae being subjected to stirring in the upstream process and harvesting is done via bubbling in the downstream process. This model conducts both the upstream and downstream processes in the same chamber. It was reported in this work that the time needed to extract microalgae scales with the square of the height of the photobioreactor. Thus, the height of the photobioreactor should be a significant factor in the photobioreactor design: doubling the height translates into quadrupling the time needed for harvesting, increasing the time and energy costs in the downstream process. A possible approach would be first to consider the minimum height required to grow the microalgae, and proceed to design the photobioreactor to be no more than twice of this minimum height, as this helps to ensure that the increase in height and hence amount of microalgae does not bring about lengthening of the harvesting time by a few times.

This integrated design also has the added efficiency benefit as labour cost is reduced by interfacing the upstream process with the downstream process. In addition, the reduced exposure of the photobioreactor to the environment lowers environmental pollution and water contamination.

7.8 Conclusion

This section has provided an overview of the diversity of both ML approaches and microalgae problems, and the usefulness of ML as applied to microalgae cultivation through the lens of the types of high-level issues being addressed, i.e., classification, estimation, prediction, control, and analysis. It is hoped that the overview has demonstrated the usefulness of ML, its feasibility in light of the existing research works, and its potential in light of the microalgae areas still waiting for ML applications or further improvements. In other words, the problems of classification, estimation, prediction, control, and analysis in microalgae cultivation are still ripe for new and improved forms of machine learning research and development.

CHAPTER 8 CONCLUSION AND FUTURE WORK

8. Conclusion and Future Work

The increasing demands and interest on microalgae in terms of bio-diesel and possible food stock have created the requirement of producing a more efficient, sustainable and economically friendly cultivation system. Different sets of stirring speeds and bubbling rate would be applied simultaneously within the proposed PBR. The microalgae biomass is analysed in terms of valuable nutrients, and it will be set as the standard for the efficiency of the cultivation system. The review on NMs in microalgae growth has shown great potential in terms of promoting cell growth, enhancing the biomass yield and the essential nutrient contents. However, this is only valid for low NMs concentration exposure on microalgae and high NMs concentration may still lead to irreversible cell damages. Both bubbling and stirring mechanisms showed different impact on microalgae growth. For stirring, the results obtained where the increase in stirring speed (0 rpm to 390 rpm) has led to the increase in biomass concentration (4.402 g/L to 6.157 g/L). On the other hand, although a stirring speed of 390 rpm provided better biomass concentration, it did not result in the highest protein and carbohydrate composition compared with a stirring speed of 360 rpm. These results indicate that the optimum stirring speed for microalgal cultivation is 360 rpm, at which the total carbohydrate concentration and total protein concentration are at the highest values along with the acceptable biomass concentration. On the other hand, the biomass mass increased when the bubbling rate increased from 150 to 200 cc/min (5.229 g/L to 5.913 g/L). For total protein case, there is a slight increase when the bubbling rate increased from 150 cc/min to 200 cc/min (0.577 mg/mg to 0.553 mg/mg), this is then followed with an increase up to 0.640 mg/mg at 250 cc/min. The increase in the bubbling rate did not show a similar trend for the carbohydrate concentration, whereby the impact of the reduction of gas bubble contact time was not overcome by the increased substrate used for the microalgal growth, and the total protein concentration increased with the bubbling rate. Considering the increase in biomass and total protein concentrations is considerably more significant in 150 cc/min, it is possible to deduce that the optimum bubbling rate for microalgae cultivation is 150 cc/min. Upscaling of the 1 L PBRs to 5 L did show success where the upscaled cultivation were able to obtain at approximately 5 times of the laboratory-scale systems (5.283 g/L to 27.860 g/L).

As discussed in the final chapter, the study on stirring and bubbling mechanisms in this work can be adapted to the development of an automated closed system. ML for the automated system was also discussed. In particular, the feasibility and potential of ML approaches on microalgae cultivation have been reviewed, where the usefulness of the methods are studied. An AI automated system in microalgae cultivation can reduce potential human errors, allowing for faster and more accurate alterations to maintain optimum conditions for cultivation. Such approaches allow direct changes through a series of cell classifications. This is followed by estimation and prediction of the problem faced and possible mitigation methods before any alteration can be made to the control. Large quantities of high-quality real-life industrial data are required for proper training of AI for automation via ML. Future work may suitably involve training of the AI of the automated closed system with feedback from the industries.

Acknowledgements

This study is supported by the Fundamental Research Grant Scheme (Malaysia, FRGS/1/2020/STG01/UNIM/02/2), the Ministry of Higher Education.

References

Agathokleous, E. *et al.* (2019) 'The two faces of nanomaterials: A quantification of hormesis in algae and plants', *Environment International*, 131(July). Available at: https://doi.org/10.1016/j.envint.2019.105044.

Ali, S., Tyagi, A. and Bae, H. (2003) 'ROS interplay between plant growth and stress biology: Challenges and future perspectives', *Plant Physiology and Biochemistry*, 203(108032).

Babiak, W. and Krzemińska, I. (2021) 'Extracellular polymeric substances (EPS) as microalgal bioproducts: A review of factors affecting EPS synthesis and application in flocculation processes', *Energies*, 14(13). Available at: https://doi.org/10.3390/en14134007.

Banerjee, S. *et al.* (2020) 'Influence of photobioreactor configuration on microalgal biomass production', *Bioprocess and Biosystems Engineering*, 43(8), pp. 1487–1497. Available at: https://doi.org/10.1007/s00449-020-02342-4.

Bhuvaneshwari, M. *et al.* (2015) 'Cytotoxicity of ZnO NPs towards fresh water algae Scenedesmus obliquus at low exposure concentrations in UV-C , visible and dark conditions', *Aquatic Toxicology*, 162, pp. 29–38. Available at: https://doi.org/10.1016/j.aquatox.2015.03.004.

Chai, W.S. *et al.* (2021) 'Microalgae and ammonia: A review on inter-relationship', *Fuel*, 303, p. 121303. Available at: https://doi.org/10.1016/j.fuel.2021.121303.

Chan, S.S. *et al.* (2022) 'Recent advances biodegradation and biosorption of organic compounds from wastewater: Microalgae-bacteria consortium - A review', *Bioresource Technology*, 344, p. 126159. Available at: https://doi.org/10.1016/j.biortech.2021.126159.

Cheah, W.Y. *et al.* (2020) 'Enhancing microalga Chlorella sorokiniana CY-1 biomass and lipid production in palm oil mill effluent (POME) using novel-designed photobioreactor', *Bioengineered*, 11(1), pp. 61–69. Available at: https://doi.org/10.1080/21655979.2019.1704536.

Chen, F. *et al.* (2019a) 'Algae response to engineered nanoparticles: Current understanding, mechanisms and implications', *Environmental Science: Nano*, 6(4), pp. 1026–1042. Available at: https://doi.org/10.1039/c8en01368c.

Chen, F. *et al.* (2019b) 'Algae response to engineered nanoparticles: Current understanding, mechanisms and implications', *Environmental Science: Nano*, 6(4), pp. 1026–1042. Available at: https://doi.org/10.1039/c8en01368c.

Chen, J. *et al.* (2022) 'Enhanced sustainable integration of CO2 utilization and wastewater treatment using microalgae in circular economy concept', *Bioresource Technology*, p. 128188.

Cheng, D. *et al.* (2017) ‘Improving carbohydrate and starch accumulation in Chlorella sp. AE10 by a novel two-stage process with cell dilution’, *Biotechnology for Biofuels*, 10(1), pp. 1–14. Available at: https://doi.org/10.1186/s13068-017-0753-9.

Cheng, S.Y. *et al.* (2019) ‘New Prospects for Modified Algae in Heavy Metal Adsorption’, *Trends in Biotechnology*, 37(11), pp. 1255–1268. Available at: https://doi.org/10.1016/j.tibtech.2019.04.007.

Déniel, M. *et al.* (2019) ‘Current methods to monitor microalgae-nanoparticle interaction and associated effects’, *Aquatic Toxicology*, 217. Available at: https://doi.org/10.1016/j.aquatox.2019.105311.

Ding, Y.D. *et al.* (2016) ‘Effect of CO2 bubbles behaviors on microalgal cells distribution and growth in bubble column photobioreactor’, *International Journal of Hydrogen Energy*, 41(8), pp. 4879–4887. Available at: https://doi.org/10.1016/j.ijhydene.2015.11.050.

Doan, Y.T.-T. *et al.* (2021) ‘Optimization of Spirulina sp. cultivation using reinforcement learning with state prediction based on LSTM neural network’, *Journal of Applied Phycology*, 33(5), pp. 2733–2744.

Dolganyuk, V. *et al.* (2020) ‘Microalgae: A promising source of valuable bioproducts’, *Biomolecules*, 10(8), pp. 1–24. Available at: https://doi.org/10.3390/biom10081153.

Du, S. *et al.* (2016) ‘Reduced graphene oxide induces cytotoxicity and inhibits photosynthetic performance of the green alga Scenedesmus obliquus’, *Chemosphere*, 164, pp. 499–507. Available at: https://doi.org/10.1016/j.chemosphere.2016.08.138.

Duan, H., Ren, Y. and Zhang, L. (2018) ‘Effects of Interphase Forces on Fluid Flow in Gas-Stirred Steel Ladles Using the Eulerian – Lagrangian Multiphase Approach’, *The Minerals, Metals & Material Society* [Preprint]. Available at: https://doi.org/10.1007/s11837-018-3045-3.

DuBois, Michel. *et al.* (1956) ‘Colorimetric Method for Determination of Sugars and Related Substances’, *Analytical Chemistry*, 28(3), pp. 350–356. Available at: https://doi.org/10.1021/ac60111a017.

Fazelian, N., Yousefzadi, M. and Movafeghi, A. (2020) ‘Algal Response to Metal Oxide Nanoparticles: Analysis of Growth, Protein Content, and Fatty Acid Composition’, *Bioenergy Research*, 13(3), pp. 944–954. Available at: https://doi.org/10.1007/s12155-020-10099-7.

Genevière, A.M. *et al.* (2020) ‘Responses to iron oxide and zinc oxide nanoparticles in echinoderm embryos and microalgae: uptake, growth, morphology, and transcriptomic analysis’, *Nanotoxicology*, 14(10), pp. 1342–1361. Available at: https://doi.org/10.1080/17435390.2020.1827074.

Ghorbanpour, M. and Fahimirad, S. (2017) ‘Plant nanobionics a novel approach to overcome the environmental challenges’, *Medicinal Plants and Environmental Challenges*, pp. 247–257. Available at: https://doi.org/10.1007/978-3-319-68717-9_14.

Giraldo, J.P. *et al.* (2014a) ‘Plant nanobionics approach to augment photosynthesis and biochemical sensing’, *Nature Materials*, 13, pp. 400–408. Available at: https://doi.org/10.1038/nmat3947.

Giraldo, J.P. *et al.* (2014b) ‘Plant nanobionics approach to augment photosynthesis and biochemical sensing’, *Nature Materials*, 13, pp. 400–408. Available at: https://doi.org/10.1038/nmat3947.

Guo, B. *et al.* (2017) ‘High-throughput, label-free, single-cell, microalgal lipid screening by machine-learning-equipped optofluidic time-stretch quantitative phase microscopy’, *Cytometry Part A*, 91(5), pp. 494–502.

Hagendijk, A.J. (2015) ‘Design of an optimal photobioreactor’, (March).

Handler, R.M. *et al.* (2012) ‘Evaluation of environmental impacts from microalgae cultivation in open-air raceway ponds: Analysis of the prior literature and investigation of wide variance in predicted impacts’, *Algal Research*, 1(1), pp. 83–92.

Hashemi, E. *et al.* (2014) ‘Cyto and genotoxicities of graphene oxide and reduced graphene oxide sheets on spermatozoa’, *RSC Advances*, 4(52), pp. 27213–27223. Available at: https://doi.org/10.1039/c4ra01047g.

Hazeem, L.J. *et al.* (2015a) ‘Effect of magnetic iron oxide (Fe3O4) nanoparticles on the growth and photosynthetic pigment content of Picochlorum sp.’, *Environmental Science and Pollution Research International*, 22(15), pp. 11728–11739. Available at: https://doi.org/10.1007/s11356-015-4370-5.

Hazeem, L.J. *et al.* (2015b) ‘Effect of magnetic iron oxide (Fe3O4) nanoparticles on the growth and photosynthetic pigment content of Picochlorum sp.’, *Environmental Science and Pollution Research International*, 22(15), pp. 11728–11739. Available at: https://doi.org/10.1007/s11356-015-4370-5.

Helmy, M. *et al.* (2022) ‘Perspective: multi-omics and machine learning help unleash the alternative food potential of microalgae’, *Advances in Nutrition* [Preprint].

Hondzo, M.M., Kapur, A. and Lembi, C.A. (1998) ‘The effect of small-scale fluid motion on the green alga’, *Hydrobiologia*, 364, pp. 1–11.

Hossain, S.M.Z. *et al.* (2022) ‘Modeling and multi-objective optimization of microalgae biomass production and CO2 biofixation using hybrid intelligence approaches’, *Renewable and Sustainable Energy Reviews*, 157, p. 112016.

Hou, J. *et al.* (2018) ‘Toxic effects of different types of zinc oxide nanoparticles on algae, plants, invertebrates, vertebrates and microorganisms’, *Chemosphere*, 193, pp. 852–860. Available at: https://doi.org/10.1016/j.chemosphere.2017.11.077.

Huang, Q. *et al.* (2017) ‘Design of Photobioreactors for Mass Cultivation of Photosynthetic Organisms’, *Engineering*, 3(3), pp. 318–329. Available at: https://doi.org/10.1016/J.ENG.2017.03.020.

Hund-Rinke, K. and Simon, M. (2006) ‘Ecotoxic effect of photocatalytic active nanoparticles (TiO2) on algae and daphnids’, *Environmental Science and Pollution Research*, 13, pp. 225–232. Available at: https://doi.org/10.1065/espr2006.06.311.

Isiya, D.A. and Sani, M. (2020) ‘Effects of Different Stirring Rates on the Chlorella Vulgaris Growth for Wastewater Treatment Systems’, *International Journal of Engineering Applied Sciences and Technology*, 04(11), pp. 454–460. Available at: https://doi.org/10.33564/ijeast.2020.v04i11.081.

Kim, S., Agca, C. and Agca, Y. (2013) ‘Effects of various physical stress factors on mitochondrial function and reactive oxygen species in rat spermatozoa’, *Reproduction, Fertility and Development*, 25(7), pp. 1051–1064. Available at: https://doi.org/10.1071/RD12212.

Koyande, A.K. *et al.* (2019) ‘Microalgae: A potential alternative to health supplementation for humans’, *Food Science and Human Wellness*, 8(1), pp. 16–24. Available at: https://doi.org/10.1016/j.fshw.2019.03.001.

Książyk, M. *et al.* (2015) ‘Toxic effect of silver and platinum nanoparticles toward the freshwater microalga Pseudokirchneriella subcapitata’, *Bulletin of Environmental Contamination and Toxicology*, 94, pp. 554–558. Available at: https://doi.org/10.1007/s00128-015-1505-9.

Kushwaha, O.S., Uthayakumar, H. and Kumaresan, K. (2023) 'Modeling of carbon dioxide fixation by microalgae using hybrid artificial intelligence (AI) and fuzzy logic (FL) methods and optimization by genetic algorithm (GA)', *Environmental Science and Pollution Research*, 30(10), pp. 24927–24948.

Kwak, S.Y. *et al.* (2017) 'A Nanobionic Light-Emitting Plant', *Nano Letters*, 17(12), pp. 7951–7961. Available at: https://doi.org/10.1021/acs.nanolett.7b04369.

Kwok, K.W. *et al.* (2010) 'Chronic toxicity of double-walled carbon nanotubes to three marine organisms: influence of different dispersion methods', *Nanomedicine*, 5(6), pp. 951–961. Available at: https://doi.org/10.2217/nnm.10.59.

de la Noüe, J. *et al.* (1984) 'Influence of agitation and aeration modes on biomass production by Oocystis sp. grown on wastewaters', *Biomass*, 4(1), pp. 43–58. Available at: https://doi.org/10.1016/0144-4565(84)90034-9.

Lambreva, M.D. *et al.* (2015) 'Potential of carbon nanotubes in algal biotechnology', *Photosynthesis Research*, 125(3), pp. 451–471. Available at: https://doi.org/10.1007/s11120-015-0168-z.

Lau, Z.L. *et al.* (2022a) 'A review on the diverse interactions between microalgae and nanomaterials: Growth variation, photosynthetic performance and toxicity', *Bioresource Technology*, 351. Available at: https://doi.org/10.1016/j.biortech.2022.127048.

Lau, Z.L. *et al.* (2022b) 'A review on the diverse interactions between microalgae and nanomaterials: Growth variation, photosynthetic performance and toxicity', *Bioresource Technology*, 351.

Lee, W.M. and An, Y.J. (2013) 'Effects of zinc oxide and titanium dioxide nanoparticles on green algae under visible, UVA, and UVB irradiations: No evidence of enhanced algal toxicity under UV pre-irradiation', *Chemosphere*, 91(4), pp. 536–544. Available at: https://doi.org/10.1016/j.chemosphere.2012.12.033.

Le-Thi-Thu, N., Nguyen-Van-Duong, T. and Doan-Van, T. (2022) 'Combining Artificial Intelligence with the Internet of Things in Microalgae Cultivation', in *International Conference on Intelligence of Things*, pp. 156–166.

Levasseur, W., Pozzobon, V. and Perré, P. (2021) 'Green microalgae in intermittent light: a meta-analysis assisted by machine learning', *Journal of Applied Phycology*, pp. 1–24.

Lew, T.T.S. *et al.* (2021) 'Plant Nanobionic Sensors for Arsenic Detection', *Advanced Materials*, 33(1), pp. 1–11. Available at: https://doi.org/10.1002/adma.202005683.

Li, X. *et al.* (2011) 'Biosynthesis of nanoparticles by microorganisms and their applications', *Journal of Nanomaterials*, 2011. Available at: https://doi.org/10.1155/2011/270974.

Li, X. *et al.* (2020) 'Enhanced Photosynthesis of Carotenoids in Microalgae Driven by Light-Harvesting Gold Nanoparticles', *ACS Sustainable Chemistry and Engineering*, 8(20), pp. 7600–7608. Available at: https://doi.org/10.1021/acssuschemeng.0c00315.

Li, Y. *et al.* (2013) 'Graphene microsheets enter cells through spontaneous membrane penetration at edge asperities and corner sites', *Proceedings of the National Academy of Sciences of the United States of America*, 110(30), pp. 12295–12300. Available at: https://doi.org/10.1073/pnas.1222276110.

Li, Y. (2017) 'Deep reinforcement learning: an overview', *Morgan & Claypool: Synthesis Lectures in Artificial Intelligence and Machine Learning* [Preprint].

Lim, H.R. *et al.* (2022) ‘Smart microalgae farming with internet-of-things for sustainable agriculture’, *Biotechnology Advances*, 57, p. 107931.

Lin, M., Tseng, Y.H. and Huang, C. (2015) ‘Interactions between nano-TiO 2 particles and algal cells at moderate particle concentration’, 9(2), pp. 242–257. Available at: https://doi.org/10.1007/s11705-015-1513-7.

Liu, B.L. *et al.* (2020) ‘Evaluation of dynamic binding performance of C-phycocyanin and allophycocyanin in Spirulina platensis algae by aminated polyacrylonitrile nanofiber membrane’, *Biochemical Engineering Journal*, 161(May), p. 107686. Available at: https://doi.org/10.1016/j.bej.2020.107686.

Liu, J.-Y., Zeng, L.-H. and Ren, Z.-H. (2021) ‘The application of spectroscopy technology in the monitoring of microalgae cells concentration’, *Applied Spectroscopy Reviews*, 56(3), pp. 171–192.

Liu, S. *et al.* (2011) ‘Antibacterial activity of graphite, graphite oxide, graphene oxide, and reduced graphene oxide: Membrane and oxidative stress’, *ACS Nano*, 5(9), pp. 6971–6980. Available at: https://doi.org/10.1021/nn202451x.

López-Rosales, L. *et al.* (2017) ‘Modeling shear-sensitive dinoflagellate microalgae growth in bubble column photobioreactors’, *Bioresource Technology*, 245, pp. 250–257. Available at: https://doi.org/10.1016/j.biortech.2017.08.161.

Low, S.S. *et al.* (2021) ‘Microalgae Cultivation in Palm Oil Mill Effluent (POME) Treatment and Biofuel Production’, *Sustainability*, 13(6), p. 3247. Available at: https://doi.org/10.3390/su13063247.

Melegari, S.P. *et al.* (2013a) ‘Evaluation of toxicity and oxidative stress induced by copper oxide nanoparticles in the green alga Chlamydomonas reinhardtii’, *Aquatic Toxicology*, 142–143, pp. 431–440. Available at: https://doi.org/10.1016/j.aquatox.2013.09.015.

Melegari, S.P. *et al.* (2013b) ‘Evaluation of toxicity and oxidative stress induced by copper oxide nanoparticles in the green alga Chlamydomonas reinhardtii’, *Aquatic Toxicology*, 142–143, pp. 431–440. Available at: https://doi.org/10.1016/j.aquatox.2013.09.015.

Middepogu, A. *et al.* (2018a) ‘Effect and mechanism of TiO2 nanoparticles on the photosynthesis of Chlorella pyrenoidosa’, *Ecotoxicology and Environmental Safety*, 161, pp. 497–506. Available at: https://doi.org/10.1016/j.ecoenv.2018.06.027.

Middepogu, A. *et al.* (2018b) ‘Effect and mechanism of TiO2 nanoparticles on the photosynthesis of Chlorella pyrenoidosa’, *Ecotoxicology and Environmental Safety*, 161, pp. 497–506. Available at: https://doi.org/10.1016/j.ecoenv.2018.06.027.

Miller, R.J. *et al.* (2017) ‘Photosynthetic efficiency predicts toxic effects of metal nanomaterials in phytoplankton’, *Aquatic Toxicology*, 183, pp. 85–93. Available at: https://doi.org/10.1016/j.aquatox.2016.12.009.

Moreno-Garrido, I., Pérez, S. and Blasco, J. (2015) ‘Toxicity of silver and gold nanoparticles on marine microalgae’, *Marine Environmental Research*, 111, pp. 60–73. Available at: https://doi.org/10.1016/j.marenvres.2015.05.008.

Mubarak, M., Shaija, A. and Prashanth, P. (2019) ‘Bubble column photobioreactor for Chlorella pyrenoidosa cultivation and validating gas hold up and volumetric mass transfer coefficient’, *Energy Sources, Part A: Recovery, Utilization and Environmental Effects*, 00(00), pp. 1–15. Available at: https://doi.org/10.1080/15567036.2019.1680769.

Najjar, Y.S.H. and Abu-Shamleh, A. (2020) ‘Harvesting of microalgae by centrifugation for biodiesel production: A review’, *Algal Research*, 51(July), p. 102046. Available at: https://doi.org/10.1016/j.algal.2020.102046.

Ochiai, H. *et al.* (2020) ‘Application of machine learning-driven label-free flow cytometry to analyze T cell products’, *Cytotherapy*, 22(5), pp. S132--S133.

Ojha, A. (2016) *Advancing microalgae culturing via bubble dynamics, mass transfer, and dynamic gr , and dynamic growth inv owth investigations estigations*, *Doctoral Dissertations*.

Pham, T.L. (2019) ‘Effect of Silver Nanoparticles on Tropical Freshwater and Marine Microalgae’, *Journal of Chemistry*, 2019. Available at: https://doi.org/10.1155/2019/9658386.

Phong, W.N. *et al.* (2018) ‘Improving cell disruption efficiency to facilitate protein release from microalgae using chemical and mechanical integrated method’, *Biochemical Engineering Journal*, 135, pp. 83–90. Available at: https://doi.org/10.1016/j.bej.2018.04.002.

Pleissner, D. *et al.* (2013) ‘Food waste as nutrient source in heterotrophic microalgae cultivation’, *Bioresource Technology*, 137, pp. 139–146. Available at: https://doi.org/10.1016/j.biortech.2013.03.088.

Posten, C. (2012) ‘Design and Performance Parameters of Photobioreactors’, *TATuP - Zeitschrift für Technikfolgenabschätzung in Theorie und Praxis*, 21(1), pp. 38–45. Available at: https://doi.org/10.14512/tatup.21.1.38.

Pulido-Reyes, G. *et al.* (2015) ‘Untangling the biological effects of cerium oxide nanoparticles: The role of surface valence states’, *Scientific Reports*, 5, pp. 1–14. Available at: https://doi.org/10.1038/srep15613.

Rahman, A., Kumar, S. and Nawaz, T. (2019) *Biosynthesis of nanomaterials using algae*, *Microalgae Cultivation for Biofuels Production*. Elsevier Inc. Available at: https://doi.org/10.1016/B978-0-12-817536-1.00017-5.

Reimann, R. *et al.* (2020) ‘Classification of dead and living microalgae Chlorella vulgaris by bioimage informatics and machine learning’, *Algal research*, 48, p. 101908.

Rezayian, M., Niknam, V. and Ebrahimzadeh, H. (2019) ‘Oxidative damage and antioxidative system in algae’, *Toxicology Reports*. Elsevier Inc., pp. 1309–1313. Available at: https://doi.org/10.1016/j.toxrep.2019.10.001.

Rhiem, S. *et al.* (2015) ‘Interactions of multiwalled carbon nanotubes with algal cells: Quantification of association, visualization of uptake, and measurement of alterations in the composition of cells’, *Environmental Pollution*, 196, pp. 431–439. Available at: https://doi.org/10.1016/j.envpol.2014.11.011.

Sandesh, K. *et al.* (2016) ‘Design and Fabrication of Miniature Bubble Column Bioreactor for Plant Cell Culture’, in P. B. D., S.N. Gummadi, and P. V Vadlani (eds) *Biotechnology and Biochemical Engineering: Select Proceedings of ICACE 2015*. Singapore: Springer Singapore, pp. 163–169. Available at: https://doi.org/10.1007/978-981-10-1920-3_18.

Saxena, P., Sangela, V. and Harish (2020) ‘Toxicity evaluation of iron oxide nanoparticles and accumulation by microalgae Coelastrella terrestris’, *Environmental Science and Pollution Research*, 27(16), pp. 19650–19660. Available at: https://doi.org/10.1007/s11356-020-08441-9.

Schwab, F. *et al.* (2011) 'Are carbon nanotube effects on green algae caused by shading and agglomeration?', *Environmental Science and Technology*, 45(14), pp. 6136–6144. Available at: https://doi.org/10.1021/es200506b.

Silver, D. *et al.* (2016) 'Mastering the game of Go with deep neural networks and tree search', *nature*, 529(7587), pp. 484–489.

Singh, V. and Mishra, V. (2022) 'Evaluation of the effects of input variables on the growth of two microalgae classes during wastewater treatment', *Water Research*, 213, p. 118165.

Solimeno, A. and Garc\'\ia, J. (2019) 'Microalgae and bacteria dynamics in high rate algal ponds based on modelling results: Long-term application of BIO_ALGAE model', *Science of the total environment*, 650, pp. 1818–1831.

Stephen, A.J. *et al.* (2019) 'Platinum and palladium bio-synthesized nanoparticles as sustainable fuel cell catalysts', *Frontiers in Energy Research*, 7(JUL), pp. 1–13. Available at: https://doi.org/10.3389/fenrg.2019.00066.

Tang, D.Y.Y. *et al.* (2023) 'Application of regression and artificial neural network analysis of Red-Green-Blue image components in prediction of chlorophyll content in microalgae', *Bioresource technology*, 370, p. 128503.

Tang, Y. *et al.* (2017) 'The Toxicity of Nanoparticles to Algae', in *Bioactivity of Engineered Nanoparticles, Nanomedicine and Nanotoxicology*, pp. 1–20. Available at: https://doi.org/10.1007/978-981-10-5864-6.

Tao, F. *et al.* (2019) 'Simulation study on gas holdup of large and small bubbles in a high pressure gas-liquid bubble column', *Processes*, 7(9). Available at: https://doi.org/10.3390/pr7090594.

Teng, S.Y. *et al.* (2020) 'Microalgae with artificial intelligence: A digitalized perspective on genetics, systems and products', *Biotechnology advances*, 44, p. 107631.

Torres, R., Diz, V.E. and Lagorio, M.G. (2018) 'Effects of gold nanoparticles on the photophysical and photosynthetic parameters of leaves and chloroplasts', *Photochemical and Photobiological Sciences*, 17(4), pp. 505–516. Available at: https://doi.org/10.1039/c8pp00067k.

Treloar, N.J. *et al.* (2020a) 'Deep reinforcement learning for the control of microbial co-cultures in bioreactors', *PLoS computational biology*, 16(4), p. e1007783.

Treloar, N.J. *et al.* (2020b) 'Deep reinforcement learning for the control of microbial co-cultures in bioreactors', *PLoS computational biology*, 16(4), p. e1007783.

Vale, M.A. *et al.* (2020) 'CO2 capture using microalgae', *Advances in Carbon Capture*, pp. 381–405. Available at: https://doi.org/10.1016/b978-0-12-819657-1.00017-7.

Walls, P.L.L. *et al.* (2017) 'Quantifying the potential for bursting bubbles to damage suspended cells.', *Scientific reports*, 7(1), p. 15102. Available at: https://doi.org/10.1038/s41598-017-14531-5.

Wang, F. *et al.* (2019) 'Effects of nanoparticles on algae: Adsorption, distribution, ecotoxicity and fate', *Applied Sciences (Switzerland)*, 9(8), pp. 1–14. Available at: https://doi.org/10.3390/app9081534.

Wang, J. and Wang, W. (2014) ‘Significance of physicochemical and uptake kinetics in controlling the toxicity of metallic nanomaterials to aquatic organisms *’, 15(8), pp. 573–592. Available at: https://doi.org/10.1631/jzus.A1400109.

Wang, K. *et al.* (2022) ‘How does the Internet of Things (IoT) help in microalgae biorefinery?’, *Biotechnology advances*, 54, p. 107819.

Wang, S., Lv, J. and Zhang, S. (2016) ‘Cellular Internalization and Intracellular Biotransformation of Silver Nanoparticles in Chlamydomonas Reinhardtii’, *Nanotoxicology*, 5390(April). Available at: https://doi.org/10.1080/17435390.2016.1179809.

Wang, Y. *et al.* (2021) ‘Identification of living and dead microalgae cells with digital holography and verified in the East China Sea’, *Marine Pollution Bulletin*, 163, p. 111927.

Warnaars, T.A. and Hondzo, M. (2006) ‘Small-scale fluid motion mediates growth and nutrient uptake of Selenastrum capricornutum’, *Freshwater Biology*, 51(6), pp. 999–1015. Available at: https://doi.org/10.1111/j.1365-2427.2006.01546.x.

Wei, L. *et al.* (2010) ‘Cytotoxicity effects of water dispersible oxidized multiwalled carbon nanotubes on marine alga , Dunaliella tertiolecta’, *Aquatic Toxicology*, 100(2), pp. 194–201. Available at: https://doi.org/10.1016/j.aquatox.2010.07.001.

Wong, M.H. *et al.* (2017) ‘Nitroaromatic detection and infrared communication from wild-type plants using plant nanobionics’, *Nature Materials*, 16(2), pp. 264–272. Available at: https://doi.org/10.1038/nmat4771.

Xia, B. *et al.* (2015) ‘Interaction of TiO2 nanoparticles with the marine microalga Nitzschia closterium: Growth inhibition, oxidative stress and internalization’, *Science of the Total Environment*, 508, pp. 525–533. Available at: https://doi.org/10.1016/j.scitotenv.2014.11.066.

Xu, L. *et al.* (2009) ‘Microalgal bioreactors: Challenges and opportunities’, *Engineering in Life Sciences*, 9(3), pp. 178–189. Available at: https://doi.org/10.1002/elsc.200800111.

Yin, J. *et al.* (2020) ‘Toxicity of reduced graphene oxide modified by metals in microalgae: Effect of the surface properties of algal cells and nanomaterials’, *Carbon*, 169, pp. 182–192. Available at: https://doi.org/10.1016/j.carbon.2020.07.057.

Yue, Y. *et al.* (2017) ‘Interaction of silver nanoparticles with algae and fish cells: A side by side comparison’, *Journal of Nanobiotechnology*, 15(1), pp. 1–11. Available at: https://doi.org/10.1186/s12951-017-0254-9.

Zanette, C.M. *et al.* (2019) ‘Microalgae mixotrophic cultivation for β-galactosidase production’, *Journal of Applied Phycology*, 31(3), pp. 1597–1606. Available at: https://doi.org/10.1007/s10811-018-1720-y.

Zhang, C. *et al.* (2020) ‘An overlooked effect induced by surface modification: different molecular response of: Chlorella pyrenoidosa to graphitized and oxidized nanodiamonds’, *Environmental Science: Nano*, 7(8), pp. 2302–2312. Available at: https://doi.org/10.1039/d0en00444h.

Zhang, H. *et al.* (2021) ‘Experimental study of the quantitative impact of flow turbulence on algal growth’, *Water (Switzerland)*, 13(5). Available at: https://doi.org/10.3390/w13050659.

Zhang, M. *et al.* (2018) ‘Pristine carbon dots boost the growth of Chlorella vulgaris by enhancing photosynthesis’, *Apllied Bio Material* [Preprint]. Available at: https://doi.org/10.1021/acsabm.8b00319.

Zhao, J. *et al.* (2016) ‘Interactions of CuO nanoparticles with the algae Chlorella pyrenoidosa: adhesion, uptake, and toxicity’, *Nanotoxicology*, 10(9), pp. 1297–1305. Available at: https://doi.org/10.1080/17435390.2016.1206149.

Zhao, J. *et al.* (2017) ‘Mechanistic understanding toward the toxicity of graphene-family materials to freshwater algae’, *Water Research* [Preprint]. Available at: https://doi.org/10.1016/j.watres.2016.12.037.

Zhu, C. *et al.* (2022) ‘A smart and precise mixing strategy for efficient and cost-effective microalgae production in open ponds’, *Science of The Total Environment*, 852, p. 158515.

Table S1: FSP-E absorbance in 14 days under 0 rpm stirring speed – Control (1)

Day	Absorbance									
	Dilution factor = 0			Dilution factor = 5			Dilution factor = 10			Average
	1	2	3	1	2	3	1	2	3	
0	0.209	0.209	0.209	0.042	0.042	0.042	0.023	0.023	0.023	0.217
2	0.635	0.635	0.635	0.123	0.123	0.123	0.061	0.061	0.061	0.620
4	1.745	1.745	1.745	0.438	0.438	0.438	0.190	0.190	0.191	1.946
6	2.194	2.194	2.194	0.537	0.537	0.537	0.236	0.236	0.236	2.412
8	2.227	2.227	2.227	0.517	0.517	0.517	0.228	0.228	0.228	2.363
10	2.227	2.227	2.227	0.517	0.517	0.517	0.228	0.228	0.228	2.363
12	2.227	2.227	2.227	0.517	0.517	0.517	0.228	0.228	0.228	2.363
14	2.227	2.227	2.227	0.517	0.517	0.517	0.228	0.228	0.228	2.363

Table S2: FSP-E absorbance in 14 days under 0 rpm stirring speed – Control (2)

Day	Absorbance									
	Dilution factor = 0			Dilution factor = 5			Dilution factor = 10			Average
	1	2	3	1	2	3	1	2	3	
0	0.213	0.213	0.213	0.053	0.053	0.053	0.029	0.029	0.029	0.256
2	0.430	0.430	0.430	0.084	0.084	0.085	0.040	0.040	0.040	0.417
4	1.437	1.437	1.438	0.291	0.291	0.291	0.153	0.153	0.153	1.475
6	2.252	2.252	2.252	0.479	0.479	0.479	0.252	0.252	0.252	2.389
8	2.586	2.586	2.586	0.585	0.585	0.585	0.262	0.262	0.262	2.711
10	2.496	2.497	2.497	0.609	0.609	0.609	0.315	0.315	0.315	2.896
12	2.496	2.497	2.497	0.609	0.609	0.609	0.315	0.315	0.315	2.896
14	2.496	2.497	2.497	0.609	0.609	0.609	0.315	0.315	0.315	2.896

Table S3: FSP-E absorbance in 14 days under 0 rpm stirring speed – Control (3)

Day	Absorbance									
	Dilution factor = 0			Dilution factor = 5			Dilution factor = 10			Average
	1	2	3	1	2	3	1	2	3	
0	0.141	0.141	0.141	0.030	0.030	0.030	0.017	0.017	0.017	0.152
2	0.441	0.441	0.441	0.084	0.084	0.084	0.045	0.045	0.045	0.436
4	1.185	1.185	1.185	0.235	0.235	0.235	0.112	0.112	0.112	1.160
6	1.822	1.822	1.822	0.429	0.429	0.429	0.199	0.199	0.199	1.988
8	2.431	2.431	2.432	0.527	0.527	0.527	0.286	0.286	0.286	2.641
10	2.838	2.838	2.838	0.596	0.596	0.596	0.309	0.309	0.309	2.969
12	3.085	3.085	3.085	0.761	0.761	0.761	0.414	0.414	0.414	3.676
14	3.182	3.182	3.182	0.750	0.750	0.750	0.380	0.380	0.380	3.578

Table S4: FSP-E absorbance in 14 days under 360 rpm stirring speed (1)

Day	Absorbance									
	Dilution factor = 0			Dilution factor = 5			Dilution factor = 10			Average
	1	2	3	1	2	3	1	2	3	
0	0.197	0.197	0.197	0.042	0.042	0.042	0.023	0.023	0.023	0.211
2	0.628	0.628	0.628	0.132	0.132	0.132	0.067	0.067	0.067	0.651
4	1.777	1.777	1.777	0.391	0.391	0.391	0.203	0.203	0.203	1.922
6	2.523	2.523	2.523	0.588	0.588	0.588	0.294	0.294	0.294	2.802
8	3.205	3.205	3.205	0.792	0.792	0.792	0.398	0.398	0.398	3.716
10	3.409	3.409	3.409	0.874	0.874	0.874	0.462	0.462	0.462	4.133
12	3.791	3.791	3.791	0.989	0.989	0.989	0.486	0.488	0.488	4.536
14	3.803	3.803	3.803	0.980	0.980	0.980	0.511	0.512	0.512	4.606

Table S5: FSP-E absorbance in 14 days under 360 rpm stirring speed (2)

Day	Absorbance									
	Dilution factor = 0			Dilution factor = 5			Dilution factor = 10			Average
	1	2	3	1	2	3	1	2	3	
0	0.183	0.183	0.183	0.037	0.037	0.037	0.017	0.017	0.017	0.178
2	0.590	0.590	0.590	0.117	0.117	0.117	0.053	0.053	0.053	0.567
4	1.255	1.255	1.255	0.241	0.241	0.241	0.142	0.142	0.142	1.294
6	1.788	1.788	1.788	0.366	0.366	0.366	0.198	0.198	0.198	1.866
8	2.372	2.372	2.372	0.555	0.556	0.556	0.250	0.250	0.250	2.551
10	2.639	2.639	2.639	0.645	0.645	0.645	0.305	0.305	0.305	2.971
12	2.751	2.751	2.751	0.672	0.672	0.672	0.295	0.295	0.295	3.018
14	2.751	2.751	2.751	0.672	0.672	0.672	0.295	0.295	0.295	3.018

Table S6: FSP-E absorbance in 14 days under 360 rpm stirring speed (3)

Day	Absorbance									
	Dilution factor = 0			Dilution factor = 5			Dilution factor = 10			Average
	1	2	3	1	2	3	1	2	3	
0	0.208	0.208	0.208	0.046	0.046	0.047	0.029	0.029	0.029	0.242
2	0.513	0.513	0.513	0.098	0.098	0.098	0.055	0.056	0.056	0.519
4	1.277	1.277	1.277	0.263	0.263	0.263	0.131	0.131	0.131	1.302
6	2.064	2.064	2.064	0.463	0.463	0.463	0.246	0.246	0.246	2.280
8	2.365	2.365	2.365	0.484	0.485	0.485	0.275	0.275	0.275	2.511
10	2.510	2.510	2.510	0.527	0.527	0.528	0.284	0.284	0.284	2.662
12	2.729	2.729	2.729	0.605	0.605	0.605	0.315	0.316	0.316	2.969
14	2.829	2.829	2.829	0.661	0.661	0.661	0.298	0.298	0.299	3.039

Table S7: FSP-E absorbance in 14 days under 390 rpm stirring speed (1)

Day	Absorbance									
	Dilution factor = 0			Dilution factor = 5			Dilution factor = 10			Average
	1	2	3	1	2	3	1	2	3	
0	0.174	0.174	0.174	0.039	0.039	0.039	0.026	0.026	0.026	0.209
2	0.691	0.691	0.691	0.146	0.146	0.146	0.079	0.079	0.079	0.736
4	1.876	1.876	1.876	0.425	0.425	0.425	0.222	0.222	0.222	2.073
6	2.679	2.679	2.679	0.626	0.626	0.626	0.326	0.326	0.326	3.024
8	3.271	3.271	3.271	0.796	0.796	0.796	0.408	0.408	0.408	3.778
10	3.473	3.473	3.473	0.882	0.882	0.882	0.482	0.482	0.482	4.233
12	3.581	3.581	3.581	0.934	0.935	0.935	0.481	0.481	0.481	4.354
14	3.340	3.340	3.340	0.859	0.860	0.860	0.442	0.442	0.442	4.018

Table S8: FSP-E absorbance in 14 days under 390 rpm stirring speed (2)

Day	Absorbance									
	Dilution factor = 0			Dilution factor = 5			Dilution factor = 10			Average
	1	2	3	1	2	3	1	2	3	
0	0.196	0.196	0.196	0.047	0.047	0.047	0.027	0.027	0.027	0.235
2	0.528	0.528	0.528	0.112	0.112	0.113	0.068	0.068	0.068	0.589
4	1.394	1.394	1.394	0.291	0.291	0.291	0.165	0.165	0.165	1.499
6	2.196	2.196	2.196	0.491	0.491	0.491	0.240	0.240	0.240	2.349
8	2.759	2.759	2.760	0.671	0.671	0.671	0.336	0.336	0.336	3.156
10	3.126	3.126	3.126	0.721	0.721	0.721	0.336	0.336	0.336	3.362
12	3.318	3.318	3.318	0.746	0.746	0.746	0.431	0.431	0.431	3.787
14	3.422	3.422	3.422	0.875	0.875	0.875	0.461	0.461	0.461	4.136

Table S9: FSP-E absorbance in 14 days under 390 rpm stirring speed (3)

Day	Absorbance									
	Dilution factor = 0			Dilution factor = 5			Dilution factor = 10			Average
	1	2	3	1	2	3	1	2	3	
0	0.205	0.205	0.205	0.049	0.049	0.049	0.026	0.026	0.026	0.237
2	0.673	0.673	0.673	0.138	0.138	0.138	0.067	0.067	0.067	0.677
4	2.058	2.058	2.058	0.443	0.443	0.443	0.207	0.207	0.207	2.113
6	2.893	2.893	2.893	0.662	0.662	0.662	0.298	0.298	0.298	3.061
8	3.444	3.444	3.444	0.820	0.820	0.820	0.435	0.435	0.435	3.965
10	3.673	3.673	3.673	0.922	0.922	0.922	0.462	0.462	0.462	4.302
12	3.690	3.690	3.690	1.022	1.022	1.022	0.441	0.441	0.441	4.403
14	3.574	3.574	3.574	1.021	1.021	1.021	0.515	0.515	0.515	4.609

Table S10: FSP-E absorbance in 16 days under 420 rpm stirring speed (1)

Day	Absorbance									
	Dilution factor = 0			Dilution factor = 5			Dilution factor = 10			Average
	1	2	3	1	2	3	1	2	3	
0	0.149	0.149	0.149	0.032	0.032	0.032	0.019	0.019	0.019	0.166
2	0.663	0.663	0.663	0.145	0.145	0.145	0.074	0.074	0.074	0.710
4	1.403	1.403	1.404	0.303	0.303	0.303	0.154	0.154	0.154	1.486
6	1.912	1.912	1.912	0.435	0.435	0.435	0.217	0.217	0.218	2.087
8	2.142	2.142	2.142	0.494	0.494	0.494	0.254	0.254	0.254	2.383
10	2.191	2.191	2.191	0.532	0.533	0.533	0.277	0.277	0.277	2.540
12	2.455	2.455	2.455	0.562	0.562	0.563	0.295	0.296	0.296	2.741
14	2.408	2.408	2.410	0.595	0.596	0.596	0.292	0.292	0.292	2.770
16	2.408	2.408	2.410	0.595	0.596	0.596	0.292	0.292	0.292	2.770

Table S11: FSP-E absorbance in 16 days under 420 rpm stirring speed (2)

Day	Absorbance									
	Dilution factor = 0			Dilution factor = 5			Dilution factor = 10			Average
	1	2	3	1	2	3	1	2	3	
0	0.140	0.140	0.140	0.034	0.034	0.034	0.020	0.020	0.020	0.170
2	0.425	0.425	0.426	0.118	0.118	0.118	0.064	0.064	0.064	0.551
4	1.762	1.762	1.763	0.388	0.388	0.388	0.206	0.206	0.206	1.919
6	2.575	2.575	2.576	0.594	0.593	0.593	0.283	0.283	0.283	2.791
8	3.292	3.292	3.292	0.785	0.785	0.785	0.411	0.411	0.411	3.776
10	3.658	3.658	3.658	0.982	0.982	0.982	0.442	0.442	0.442	4.328
12	3.873	3.873	3.873	1.058	1.058	1.058	0.494	0.494	0.494	4.699
14	3.837	3.837	3.837	0.936	0.936	0.936	0.473	0.473	0.473	4.415
16	3.837	3.837	3.837	0.936	0.936	0.936	0.473	0.473	0.473	4.415

Table S12: FSP-E absorbance in 16 days under 420 rpm stirring speed (3)

Day	Absorbance									
	Dilution factor = 0			Dilution factor = 5			Dilution factor = 10			Average
	1	2	3	1	2	3	1	2	3	
0	0.192	0.192	0.192	0.042	0.042	0.042	0.022	0.022	0.022	0.207
2	0.871	0.871	0.871	0.190	0.190	0.190	0.097	0.097	0.097	0.932
4	1.643	1.643	1.643	0.370	0.370	0.370	0.175	0.175	0.175	1.748
6	1.889	1.889	1.889	0.399	0.399	0.399	0.173	0.173	0.173	1.873
8	2.311	2.311	2.311	0.586	0.586	0.586	0.251	0.251	0.251	2.585
10	2.700	2.701	2.701	0.595	0.595	0.595	0.294	0.294	0.295	2.874
12	3.047	3.047	3.047	0.802	0.802	0.802	0.332	0.332	0.332	3.460
14	3.227	3.227	3.227	0.813	0.814	0.814	0.385	0.385	0.385	3.715
16	3.233	3.234	3.234	0.844	0.845	0.845	0.375	0.376	0.376	3.737

Table S13: FSP-E absorbance in 16 days under 150 cc/min bubbling rate (1)

Day	Absorbance									
	Dilution factor = 0			Dilution factor = 5			Dilution factor = 10			Average
	1	2	3	1	2	3	1	2	3	
0	0.149	0.149	0.149	0.032	0.032	0.032	0.019	0.019	0.019	0.166
2	0.663	0.663	0.663	0.145	0.145	0.145	0.074	0.074	0.074	0.710
4	1.403	1.403	1.404	0.303	0.303	0.303	0.154	0.154	0.154	1.486
6	1.912	1.912	1.912	0.435	0.435	0.435	0.217	0.217	0.218	2.087
8	2.142	2.142	2.142	0.494	0.494	0.494	0.254	0.254	0.254	2.383
10	2.191	2.191	2.191	0.532	0.533	0.533	0.277	0.277	0.277	2.540
12	2.455	2.455	2.455	0.562	0.562	0.563	0.295	0.296	0.296	2.741
14	2.408	2.408	2.410	0.595	0.596	0.596	0.292	0.292	0.292	2.770
16	2.408	2.408	2.410	0.595	0.596	0.596	0.292	0.292	0.292	2.770

Table S14: FSP-E absorbance in 16 days under 150 cc/min bubbling rate (2)

Day	Absorbance									
	Dilution factor = 0			Dilution factor = 5			Dilution factor = 10			Average
	1	2	3	1	2	3	1	2	3	
0	0.140	0.140	0.140	0.034	0.034	0.034	0.020	0.020	0.020	0.170
2	0.425	0.425	0.426	0.118	0.118	0.118	0.064	0.064	0.064	0.551
4	1.762	1.762	1.763	0.388	0.388	0.388	0.206	0.206	0.206	1.919
6	2.575	2.575	2.576	0.594	0.593	0.593	0.283	0.283	0.283	2.791
8	3.292	3.292	3.292	0.785	0.785	0.785	0.411	0.411	0.411	3.776
10	3.658	3.658	3.658	0.982	0.982	0.982	0.442	0.442	0.442	4.328
12	3.873	3.873	3.873	1.058	1.058	1.058	0.494	0.494	0.494	4.699
14	3.837	3.837	3.837	0.936	0.936	0.936	0.473	0.473	0.473	4.415
16	3.837	3.837	3.837	0.936	0.936	0.936	0.473	0.473	0.473	4.415

Table S15: FSP-E absorbance in 16 days under 150 cc/min bubbling rate (3)

Day	Absorbance									
	Dilution factor = 0			Dilution factor = 5			Dilution factor = 10			Average
	1	2	3	1	2	3	1	2	3	
0	0.192	0.192	0.192	0.042	0.042	0.042	0.022	0.022	0.022	0.207
2	0.871	0.871	0.871	0.190	0.190	0.190	0.097	0.097	0.097	0.932
4	1.643	1.643	1.643	0.370	0.370	0.370	0.175	0.175	0.175	1.748
6	1.889	1.889	1.889	0.399	0.399	0.399	0.173	0.173	0.173	1.873
8	2.311	2.311	2.311	0.586	0.586	0.586	0.251	0.251	0.251	2.585
10	2.700	2.701	2.701	0.595	0.595	0.595	0.294	0.294	0.295	2.874
12	3.047	3.047	3.047	0.802	0.802	0.802	0.332	0.332	0.332	3.460
14	3.227	3.227	3.227	0.813	0.814	0.814	0.385	0.385	0.385	3.715
16	3.233	3.234	3.234	0.844	0.845	0.845	0.375	0.376	0.376	3.737

Table S16: FSP-E absorbance in 14 days under 200 cc/min bubbling rate (1)

Day	Absorbance									
	Dilution factor = 0			Dilution factor = 5			Dilution factor = 10			Average
	1	2	3	1	2	3	1	2	3	
0	0.178	0.178	0.178	0.037	0.037	0.037	0.023	0.023	0.023	0.198
2	0.566	0.566	0.566	0.123	0.123	0.123	0.064	0.064	0.064	0.608
4	1.172	1.172	1.173	0.251	0.251	0.251	0.136	0.136	0.136	1.262
6	1.578	1.578	1.578	0.323	0.323	0.323	0.190	0.190	0.190	1.699
8	2.320	2.320	2.320	0.574	0.574	0.574	0.272	0.272	0.272	2.637
10	2.734	2.734	2.734	0.630	0.630	0.630	0.336	0.336	0.336	3.080
12	2.977	2.977	2.977	0.867	0.867	0.867	0.357	0.357	0.357	3.628
14	3.151	3.151	3.151	0.742	0.743	0.743	0.414	0.414	0.414	3.667

Table S17: FSP-E absorbance in 14 days under 200 cc/min bubbling rate (2)

Day	Absorbance									
	Dilution factor = 0			Dilution factor = 5			Dilution factor = 10			Average
	1	2	3	1	2	3	1	2	3	
0	0.174	0.174	0.174	0.039	0.039	0.039	0.020	0.020	0.020	0.190
2	0.679	0.679	0.679	0.130	0.130	0.130	0.086	0.086	0.086	0.730
4	1.500	1.500	1.500	0.325	0.325	0.325	0.155	0.155	0.155	1.557
6	2.123	2.123	2.123	0.521	0.521	0.521	0.228	0.229	0.229	2.337
8	2.857	2.857	2.857	0.728	0.728	0.728	0.346	0.346	0.346	3.319
10	3.312	3.312	3.312	0.782	0.782	0.782	0.389	0.390	0.390	3.706
12	3.439	3.439	3.439	0.851	0.851	0.851	0.420	0.420	0.420	3.963
14	3.486	3.486	3.486	0.864	0.864	0.864	0.446	0.447	0.447	4.091

Table S18: FSP-E absorbance in 14 days under 200 cc/min bubbling rate (3)

Day	Absorbance									
	Dilution factor = 0			Dilution factor = 5			Dilution factor = 10			Average
	1	2	3	1	2	3	1	2	3	
0	0.202	0.202	0.202	0.040	0.041	0.041	0.025	0.025	0.025	0.219
2	0.718	0.718	0.718	0.142	0.142	0.142	0.068	0.068	0.068	0.704
4	1.662	1.662	1.663	0.330	0.330	0.330	0.187	0.187	0.187	1.727
6	2.808	2.808	2.808	0.641	0.642	0.642	0.315	0.316	0.316	3.057
8	3.520	3.520	3.520	0.825	0.825	0.826	0.414	0.414	0.414	3.930
10	3.609	3.609	3.609	0.829	0.829	0.829	0.440	0.440	0.440	4.052
12	3.609	3.609	3.609	0.829	0.829	0.829	0.440	0.440	0.440	4.052
14	3.609	3.609	3.609	0.829	0.829	0.829	0.440	0.440	0.440	4.052

Table S19: FSP-E absorbance in 12 days under 250 cc/min bubbling rate (1)

Day	Absorbance									
	Dilution factor = 0			Dilution factor = 5			Dilution factor = 10			Average
	1	2	3	1	2	3	1	2	3	
0	0.153	0.153	0.153	0.035	0.035	0.035	0.018	0.018	0.018	0.170
2	0.535	0.536	0.536	0.113	0.113	0.113	0.061	0.061	0.061	0.570
4	1.646	1.647	1.647	0.366	0.367	0.367	0.184	0.184	0.184	1.772
6	2.595	2.595	2.596	0.580	0.580	0.580	0.305	0.305	0.305	2.847
8	3.225	3.225	3.225	0.767	0.767	0.767	0.478	0.478	0.478	3.947
10	3.561	3.561	3.561	0.882	0.882	0.882	0.473	0.473	0.473	4.234
12	3.695	3.695	3.695	0.953	0.953	0.953	0.369	0.369	0.369	4.048

Table S20: FSP-E absorbance in 12 days under 250 cc/min bubbling rate (2)

Day	Absorbance									
	Dilution factor = 0			Dilution factor = 5			Dilution factor = 10			Average
	1	2	3	1	2	3	1	2	3	
0	0.235	0.235	0.235	0.056	0.056	0.056	0.021	0.021	0.021	0.242
2	0.607	0.607	0.607	0.141	0.141	0.141	0.060	0.060	0.060	0.638
4	1.027	1.027	1.027	0.221	0.221	0.221	0.109	0.109	0.109	1.075
6	1.946	1.946	1.946	0.444	0.445	0.445	0.213	0.213	0.213	2.098
8	2.629	2.629	2.630	0.613	0.613	0.613	0.303	0.303	0.303	2.907
10	2.843	2.843	2.843	0.627	0.628	0.628	0.318	0.318	0.318	3.053
12	2.843	2.843	2.843	0.627	0.628	0.628	0.318	0.318	0.318	3.053

Table S21: FSP-E absorbance in 12 days under 250 cc/min bubbling rate (3)

Day	Absorbance									
	Dilution factor = 0			Dilution factor = 5			Dilution factor = 10			Average
	1	2	3	1	2	3	1	2	3	
0	0.201	0.202	0.202	0.039	0.039	0.039	0.023	0.023	0.023	0.208
2	0.706	0.706	0.706	0.129	0.129	0.129	0.057	0.057	0.057	0.639
4	1.280	1.280	1.280	0.234	0.234	0.235	0.139	0.139	0.139	1.281
6	2.198	2.198	2.198	0.443	0.443	0.443	0.267	0.267	0.267	2.360
8	2.691	2.691	2.691	0.607	0.607	0.607	0.346	0.346	0.346	3.062
10	3.075	3.076	3.076	0.696	0.696	0.696	0.381	0.381	0.381	3.457
12	3.216	3.217	3.217	0.800	0.800	0.800	0.334	0.334	0.334	3.519

Table S22: FSP-E absorbance in 26 days under 350 rpm, 750 cc/min (1)

Day	No dilution				Dilution factor - 5 (1:4,S:W)				Dilution factor - 10 (1:9,S:W)				Final
	1	2	3	Average	1	2	3	Average	1	2	3	Average	
0	0.174	0.174	0.174	0.174	0.047	0.047	0.047	0.233	0.028	0.028	0.028	0.279	0.228
2	0.229	0.229	0.229	0.229	0.052	0.052	0.052	0.258	0.030	0.030	0.030	0.303	0.263
4	0.273	0.273	0.273	0.273	0.053	0.053	0.053	0.264	0.036	0.036	0.037	0.364	0.301
6	0.519	0.519	0.519	0.519	0.096	0.096	0.096	0.481	0.042	0.042	0.042	0.421	0.474
8	0.762	0.762	0.762	0.762	0.152	0.152	0.152	0.759	0.097	0.097	0.097	0.972	0.831
10	0.814	0.814	0.814	0.814	0.168	0.168	0.168	0.841	0.093	0.093	0.093	0.934	0.863
12	1.039	1.039	1.039	1.039	0.203	0.203	0.203	1.017	0.111	0.111	0.111	1.114	1.057
14	1.175	1.175	1.176	1.175	0.246	0.247	0.247	1.232	0.128	0.128	0.128	1.276	1.228
16	1.224	1.225	1.225	1.225	0.260	0.260	0.260	1.298	0.126	0.126	0.126	1.256	1.259
18	1.328	1.328	1.328	1.328	0.289	0.289	0.289	1.443	0.157	0.157	0.157	1.572	1.447
20	1.518	1.518	1.518	1.518	0.313	0.313	0.313	1.566	0.181	0.181	0.181	1.810	1.631
22	1.617	1.617	1.617	1.617	0.335	0.335	0.335	1.677	0.191	0.191	0.191	1.908	1.734
24	1.733	1.733	1.733	1.733	0.380	0.380	0.380	1.900	0.194	0.194	0.194	1.938	1.857
26	1.691	1.691	1.691	1.691	0.370	0.370	0.370	1.850	0.194	0.194	0.194	1.942	1.828

Table S23: FSP-E absorbance in 26 days under 350 rpm, 750 cc/min (2)

Day	No dilution				Dilution factor - 5 (1:4,S:W)				Dilution factor - 10 (1:9,S:W)				Final
	1	2	3	Average	1	2	3	Average	1	2	3	Average	
0	0.172	0.172	0.173	0.172	0.035	0.035	0.035	0.176	0.020	0.020	0.020	0.201	0.183
2	0.251	0.251	0.251	0.251	0.056	0.056	0.056	0.281	0.025	0.025	0.025	0.251	0.261
4	0.412	0.412	0.412	0.412	0.077	0.077	0.077	0.385	0.037	0.037	0.037	0.367	0.388
6	0.592	0.592	0.592	0.592	0.110	0.110	0.110	0.551	0.059	0.059	0.059	0.585	0.576
8	0.780	0.780	0.780	0.780	0.151	0.151	0.151	0.756	0.080	0.080	0.080	0.801	0.779
10	0.964	0.964	0.964	0.964	0.189	0.189	0.189	0.946	0.106	0.106	0.106	1.064	0.991
12	1.126	1.126	1.126	1.126	0.233	0.233	0.233	1.164	0.122	0.122	0.122	1.222	1.171
14	1.230	1.230	1.230	1.230	0.292	0.292	0.292	1.461	0.139	0.139	0.139	1.386	1.359
16	1.333	1.333	1.333	1.333	0.279	0.279	0.280	1.397	0.147	0.147	0.147	1.472	1.401
18	1.370	1.370	1.371	1.370	0.284	0.284	0.284	1.420	0.152	0.152	0.152	1.515	1.435
20	1.434	1.434	1.435	1.434	0.321	0.321	0.321	1.605	0.177	0.178	0.178	1.775	1.605
22	1.431	1.431	1.431	1.431	0.330	0.330	0.330	1.650	0.169	0.169	0.169	1.691	1.591
24	1.431	1.431	1.431	1.431	0.330	0.330	0.330	1.650	0.169	0.169	0.169	1.691	1.591
26	1.431	1.431	1.431	1.431	0.330	0.330	0.330	1.650	0.169	0.169	0.169	1.691	1.591

Table S24: FSP-E absorbance in 26 days under 350 rpm, 750 cc/min (3)

Day	No dilution				Dilution factor - 5 (1:4,S:W)				Dilution factor - 10 (1:9,S:W)				Final
	1	2	3	Average	1	2	3	Average	1	2	3	Average	
0	0.173	0.173	0.173	0.173	0.035	0.035	0.035	0.173	0.020	0.020	0.020	0.200	0.182
2	0.262	0.262	0.262	0.262	0.058	0.058	0.058	0.290	0.026	0.026	0.026	0.261	0.271
4	0.421	0.421	0.421	0.421	0.077	0.078	0.078	0.387	0.035	0.035	0.036	0.355	0.388
6	0.601	0.601	0.601	0.601	0.111	0.111	0.111	0.556	0.059	0.059	0.059	0.586	0.581
8	0.799	0.799	0.799	0.799	0.152	0.152	0.152	0.761	0.079	0.079	0.079	0.791	0.784
10	0.970	0.970	0.961	0.967	0.190	0.190	0.190	0.950	0.104	0.104	0.104	1.043	0.987
12	1.132	1.132	1.132	1.132	0.233	0.233	0.233	1.164	0.122	0.122	0.122	1.222	1.173
14	1.241	1.241	1.241	1.241	0.283	0.283	0.283	1.415	0.139	0.140	0.140	1.395	1.350
16	1.334	1.334	1.334	1.334	0.280	0.280	0.280	1.401	0.148	0.148	0.148	1.482	1.406
18	1.380	1.380	1.380	1.380	0.291	0.291	0.292	1.457	0.152	0.152	0.152	1.521	1.452
20	1.451	1.451	1.451	1.451	0.330	0.330	0.330	1.651	0.176	0.176	0.176	1.762	1.621
22	1.431	1.431	1.431	1.431	0.329	0.329	0.330	1.647	0.169	0.169	0.170	1.694	1.591
24	1.431	1.431	1.431	1.431	0.329	0.329	0.330	1.647	0.169	0.169	0.170	1.694	1.591
26	1.431	1.431	1.431	1.431	0.329	0.329	0.330	1.647	0.169	0.169	0.170	1.694	1.591

Table S25: FSP-E absorbance in 22 days under 400 rpm, 750 cc/min (1)

Day	No dilution				Dilution factor - 5 (1:4,S:W)				Dilution factor - 10 (1:9,S:W)				Final
	1	2	3	Average	1	2	3	Average	1	2	3	Average	
0	0.182	0.182	0.182	0.182	0.041	0.041	0.041	0.204	0.019	0.019	0.019	0.193	0.193
2	0.422	0.422	0.422	0.422	0.089	0.089	0.089	0.444	0.048	0.048	0.048	0.478	0.448
4	0.572	0.572	0.572	0.572	0.113	0.113	0.113	0.566	0.053	0.053	0.053	0.530	0.556
6	0.790	0.790	0.790	0.790	0.181	0.181	0.181	0.905	0.091	0.091	0.092	0.914	0.870
8	0.984	0.984	0.984	0.984	0.199	0.199	0.199	0.994	0.127	0.127	0.127	1.269	1.082
10	1.201	1.201	1.201	1.201	0.259	0.259	0.259	1.295	0.143	0.143	0.143	1.426	1.307
12	1.346	1.346	1.346	1.346	0.303	0.303	0.303	1.515	0.141	0.141	0.141	1.411	1.424
14	1.392	1.393	1.393	1.392	0.284	0.284	0.284	1.421	0.157	0.157	0.157	1.571	1.461
16	1.392	1.393	1.393	1.392	0.284	0.284	0.284	1.421	0.157	0.157	0.157	1.571	1.461
18	1.392	1.393	1.393	1.392	0.284	0.284	0.284	1.421	0.157	0.157	0.157	1.571	1.461
20	1.392	1.393	1.393	1.392	0.284	0.284	0.284	1.421	0.157	0.157	0.157	1.571	1.461
22	1.392	1.393	1.393	1.392	0.284	0.284	0.284	1.421	0.157	0.157	0.157	1.571	1.461

Table S26: FSP-E absorbance in 22 days under 400 rpm, 750 cc/min (2)

Day	No dilution				Dilution factor - 5 (1:4,S:W)				Dilution factor - 10 (1:9,S:W)				Final
	1	2	3	Average	1	2	3	Average	1	2	3	Average	
0	0.180	0.180	0.180	0.180	0.039	0.039	0.039	0.196	0.019	0.019	0.019	0.186	0.187
2	0.366	0.366	0.366	0.366	0.085	0.085	0.085	0.424	0.041	0.041	0.041	0.409	0.399
4	0.526	0.526	0.526	0.526	0.116	0.116	0.116	0.578	0.054	0.054	0.054	0.535	0.546
6	0.710	0.710	0.710	0.710	0.163	0.163	0.163	0.816	0.071	0.071	0.071	0.713	0.746
8	0.924	0.924	0.924	0.924	0.198	0.198	0.198	0.990	0.088	0.088	0.088	0.884	0.933
10	1.053	1.053	1.053	1.053	0.213	0.213	0.213	1.066	0.097	0.097	0.097	0.971	1.030
12	1.117	1.117	1.117	1.117	0.220	0.220	0.220	1.099	0.137	0.137	0.137	1.372	1.196
14	1.227	1.228	1.228	1.227	0.231	0.231	0.231	1.153	0.142	0.142	0.142	1.415	1.265
16	1.293	1.293	1.293	1.293	0.265	0.265	0.265	1.325	0.126	0.126	0.126	1.258	1.292
18	1.330	1.330	1.330	1.330	0.292	0.292	0.292	1.461	0.150	0.150	0.150	1.501	1.430
20	1.375	1.375	1.375	1.375	0.276	0.276	0.276	1.380	0.155	0.155	0.155	1.553	1.436
22	1.375	1.375	1.375	1.375	0.276	0.276	0.276	1.380	0.155	0.155	0.155	1.553	1.436

Table S27: FSP-E absorbance in 22 days under 400 rpm, 750 cc/min (3)

Day	No dilution				Dilution factor - 5 (1:4,S:W)				Dilution factor - 10 (1:9,S:W)				Final
	1	2	3	Average	1	2	3	Average	1	2	3	Average	
0	0.185	0.185	0.185	0.185	0.035	0.035	0.035	0.177	0.020	0.020	0.020	0.203	0.188
2	0.331	0.331	0.331	0.331	0.069	0.069	0.069	0.344	0.033	0.033	0.033	0.328	0.334
4	0.494	0.494	0.494	0.494	0.089	0.089	0.089	0.445	0.041	0.041	0.041	0.409	0.449
6	0.706	0.706	0.706	0.706	0.142	0.142	0.142	0.709	0.078	0.078	0.078	0.776	0.730
8	0.794	0.794	0.794	0.794	0.156	0.156	0.156	0.780	0.080	0.080	0.080	0.804	0.793
10	0.931	0.931	0.931	0.931	0.187	0.187	0.187	0.934	0.103	0.103	0.103	1.026	0.964
12	1.038	1.038	1.038	1.038	0.217	0.218	0.218	1.087	0.109	0.109	0.109	1.087	1.071
14	1.169	1.169	1.169	1.169	0.229	0.229	0.229	1.144	0.110	0.110	0.110	1.104	1.139
16	1.250	1.250	1.250	1.250	0.247	0.247	0.247	1.234	0.133	0.133	0.133	1.329	1.271
18	1.358	1.358	1.358	1.358	0.282	0.282	0.282	1.411	0.169	0.169	0.169	1.692	1.487
20	1.433	1.433	1.433	1.433	0.300	0.300	0.300	1.502	0.181	0.181	0.181	1.811	1.582
22	1.450	1.450	1.450	1.450	0.292	0.292	0.292	1.461	0.179	0.179	0.179	1.788	1.566

Table S28: Protein content absorbance for different stirring speed

Speed	0			360			390			420		
Bubbling	150.000											
Protein Absorbance	0.922	0.804	0.696	0.910	0.770	0.781	1.031	0.886	1.017	0.958	1.056	0.971
	0.922	0.804	0.696	0.910	0.770	0.781	1.031	0.886	1.017	0.958	1.056	0.971
	0.922	0.804	0.696	0.910	0.770	0.781	1.031	0.886	1.017	0.958	1.056	0.971
	0.953	0.811	0.704	0.904	0.770	0.775	1.037	0.910	0.907	0.962	1.026	0.940
	0.953	0.811	0.704	0.904	0.770	0.775	1.037	0.910	0.907	0.962	1.026	0.940
	0.954	0.811	0.704	0.904	0.770	0.775	1.037	0.910	0.907	0.962	1.026	0.940
	0.916	0.758	0.703	0.912	0.767	0.774	1.028	0.881	0.938	0.969	1.041	0.988
	0.916	0.758	0.703	0.912	0.767	0.774	1.028	0.881	0.938	0.969	1.041	0.988
	0.916	0.758	0.703	0.912	0.767	0.774	1.028	0.881	0.938	0.969	1.041	0.988
Average	0.930	0.791	0.701	0.908	0.769	0.777	1.032	0.892	0.954	0.963	1.041	0.966
Final Average	0.807			0.818			0.959			0.990		
Concentration	2.460			2.493			2.923			3.016		

Table S29: Protein content fraction for different stirring speed

Speed	0			360			390			420		
Bubbling	150.000											
Protein Fraction	0.638	0.557	0.482	0.639	0.541	0.549	0.510	0.439	0.503	0.558	0.615	0.566
	0.638	0.557	0.482	0.639	0.541	0.549	0.510	0.439	0.503	0.558	0.615	0.566
	0.638	0.557	0.482	0.639	0.541	0.549	0.510	0.439	0.503	0.558	0.615	0.566
	0.660	0.561	0.487	0.635	0.541	0.544	0.513	0.450	0.449	0.561	0.598	0.548
	0.660	0.561	0.487	0.635	0.541	0.545	0.513	0.450	0.449	0.561	0.598	0.548
	0.660	0.562	0.487	0.635	0.541	0.545	0.513	0.450	0.449	0.561	0.598	0.548
	0.634	0.525	0.486	0.641	0.539	0.544	0.509	0.436	0.464	0.564	0.607	0.576
	0.634	0.525	0.486	0.641	0.539	0.544	0.509	0.436	0.464	0.564	0.607	0.576
	0.634	0.525	0.486	0.641	0.539	0.544	3.132	2.684	2.857	0.564	0.607	0.576
Average	0.559			0.575			0.744			0.577		
Standard Deviation	0.068			0.046			0.777			0.023		
Biomass	4.402			4.335			6.157			5.229		
Actual Protein Mass	2.460			2.493			4.580			3.016		

Table S30: Carbohydrate content absorbance for different stirring speed

Speed	0			360			390			420		
Bubbling	150.000											
Carbohydrate Absorbance	0.562	0.770	2.128	2.323	1.564	0.698	1.546	1.810	1.554	1.144	1.460	2.005
	0.562	0.770	2.128	2.323	1.564	0.699	1.547	1.810	1.554	1.145	1.461	2.010
	0.562	0.770	2.128	2.323	1.564	0.699	1.547	1.789	1.554	1.145	1.462	2.010
	0.889	1.154	1.971	2.017	1.566	0.460	1.150	1.153	2.418	0.855	0.549	2.086
	0.889	1.155	1.971	2.017	1.566	0.460	1.150	1.157	2.418	0.857	0.550	2.086
	0.889	1.155	1.971	2.017	1.566	0.460	1.150	1.153	2.418	0.859	0.553	2.086
	1.015	1.531	1.301	2.307	1.911	0.683	1.420	2.452	1.838	0.915	1.322	1.830
	1.015	1.531	1.301	2.307	1.911	0.683	1.420	2.452	1.838	0.916	1.326	1.832
	1.015	1.531	1.301	2.307	1.911	0.684	1.204	2.453	1.840	0.916	1.329	1.834
Average	0.822	1.152	1.800	2.216	1.680	0.614	1.348	1.803	1.937	0.972	1.112	1.975
Final Average	1.258			1.503			1.696			1.353		
Concentration	0.424			0.507			0.572			0.456		

Table S31: Carbohydrate fraction for different stirring speed

Speed	0			360			390			420		
Bubbling	150.000											
Carbohydrate Fraction	0.014	0.020	0.054	0.060	0.041	0.018	0.028	0.000	0.028	0.025	0.031	0.043
	0.014	0.020	0.054	0.060	0.041	0.018	0.028	0.000	0.028	0.025	0.031	0.043
	0.014	0.020	0.054	0.060	0.041	0.018	0.028	0.000	0.028	0.025	0.031	0.043
	0.023	0.029	0.050	0.052	0.041	0.012	0.021	0.021	0.044	0.018	0.012	0.045
	0.023	0.029	0.050	0.052	0.041	0.012	0.021	0.021	0.044	0.018	0.012	0.045
	0.023	0.029	0.050	0.052	0.041	0.012	0.021	0.021	0.044	0.018	0.012	0.045
	0.026	0.039	0.033	0.060	0.050	0.018	0.000	0.045	0.034	0.020	0.028	0.039
	0.026	0.039	0.033	0.060	0.050	0.018	0.000	0.045	0.034	0.020	0.028	0.039
	0.026	0.039	0.033	0.060	0.050	0.018	0.000	0.045	0.034	0.020	0.029	0.039
Average	0.032			0.039			0.025			0.029		
Standard Deviation	0.013			0.018			0.016			0.011		
Biomass	4.402			4.335			6.157			5.229		
Actual Carbohydrate Mass	0.141			0.169			0.151			0.152		

Table S32: Protein content absorbance for different bubbling rate

Speed	420			420			420		
Bubbling	150.000			200.000			250.000		
Protein Absorbance	0.958	1.056	0.971	1.124	1.003	1.105	1.151	1.189	1.280
	0.958	1.056	0.971	1.124	1.003	1.106	1.151	1.189	1.280
	0.958	1.056	0.971	1.124	1.003	1.106	1.151	1.189	1.280
	0.962	1.026	0.940	1.097	0.985	1.088	1.148	1.135	1.266
	0.962	1.026	0.940	1.097	0.985	1.088	1.148	1.135	1.266
	0.962	1.026	0.940	1.097	0.985	1.088	1.148	1.135	1.266
	0.969	1.041	0.988	1.153	1.001	1.105	1.134	1.127	1.278
	0.969	1.041	0.988	1.153	1.001	1.105	1.134	1.127	1.278
	0.969	1.041	0.988	1.153	1.001	1.105	1.134	1.127	1.278
Average	0.963	1.041	0.966	1.125	0.996	1.100	1.144	1.150	1.274
Final Average	0.990			1.073			1.190		
Concentration	3.016			3.271			3.625		

Table S33: Protein fraction for different bubbling rate

Speed	420			420			420		
Bubbling	150.000			200.000			250.000		
Protein Fraction	0.558	0.615	0.566	0.579	0.517	0.570	0.619	0.639	0.689
	0.558	0.615	0.566	0.579	0.517	0.570	0.619	0.639	0.689
	0.558	0.615	0.566	0.579	0.517	0.570	0.619	0.639	0.689
	0.561	0.598	0.548	0.565	0.507	0.561	0.618	0.611	0.681
	0.561	0.598	0.548	0.565	0.507	0.561	0.618	0.611	0.681
	0.561	0.598	0.548	0.565	0.507	0.561	0.618	0.611	0.681
	0.564	0.607	0.576	0.594	0.516	0.570	0.610	0.606	0.687
	0.564	0.607	0.576	0.594	0.516	0.570	0.610	0.606	0.687
	0.564	0.607	0.576	0.594	0.516	0.570	0.610	0.606	0.687
Average	0.577			0.553			0.640		
Standard Deviation	0.023			0.030			0.034		
Biomass	5.229			5.913			5.664		
Actual Protein Mass	3.016			3.271			3.625		

Table S34: Carbohydrate content absorbance for different bubbling rate

Speed	420			420			420		
Bubbling	150.000			200.000			250.000		
Carbohydrate Absorbance	1.144	1.460	2.005	1.849	0.556	0.610	0.630	0.984	1.404
	1.145	1.461	2.010	1.851	0.558	0.611	0.650	0.986	1.405
	1.145	1.462	2.010	1.856	0.559	0.612	0.640	0.988	1.405
	0.855	0.549	2.086	1.934	1.254	0.806	0.321	1.445	1.582
	0.857	0.550	2.086	1.938	1.255	0.807	0.321	1.446	1.583
	0.859	0.553	2.086	1.938	1.256	0.809	0.321	1.446	1.583
	0.915	1.322	1.830	2.204	1.676	1.285	0.958	1.939	1.501
	0.916	1.326	1.832	2.208	1.677	1.286	0.959	1.939	1.501
	0.916	1.329	1.834	2.208	1.677	1.287	0.959	1.939	1.505
Average	0.972	1.112	1.975	1.998	1.163	0.901	0.640	1.457	1.497
Final Average	1.353			1.354			1.198		
Concentration	0.456			0.457			0.404		

Table S35: Carbohydrate fraction for different bubbling rate

Speed	420			420			420		
Bubbling	150.000			200.000			250.000		
Carbohydrate Fraction	0.025	0.031	0.043	0.035	0.011	0.012	0.012	0.019	0.027
	0.025	0.031	0.043	0.035	0.011	0.012	0.012	0.019	0.027
	0.025	0.031	0.043	0.035	0.011	0.012	0.012	0.019	0.027
	0.018	0.012	0.045	0.037	0.024	0.015	0.006	0.027	0.030
	0.018	0.012	0.045	0.037	0.024	0.015	0.006	0.027	0.030
	0.018	0.012	0.045	0.037	0.024	0.015	0.006	0.027	0.030
	0.020	0.028	0.039	0.042	0.032	0.024	0.018	0.037	0.029
	0.020	0.028	0.039	0.042	0.032	0.024	0.018	0.037	0.029
	0.020	0.029	0.039	0.042	0.032	0.024	0.018	0.037	0.029
Average	0.029			0.026			0.023		
Standard Deviation	0.011			0.011			0.009		
Biomass	5.229			5.913			5.664		
Actual Carbohydrate Mass	0.152			0.152			0.129		

Table S36: p-values for statistical analysis

p-values for Each Data Set	
Biomass for stirring experiments	0.029216993
Protein fraction for stirring experiments	1.6699E-10
Carbohydrates fraction for stirring experiments	0.074648511
Biomass for bubbling experiments	0.834653235
Protein fraction for bubbling experiments	2.51816E-14
Carbohydrates fraction for bubbling experiments	0.038332564

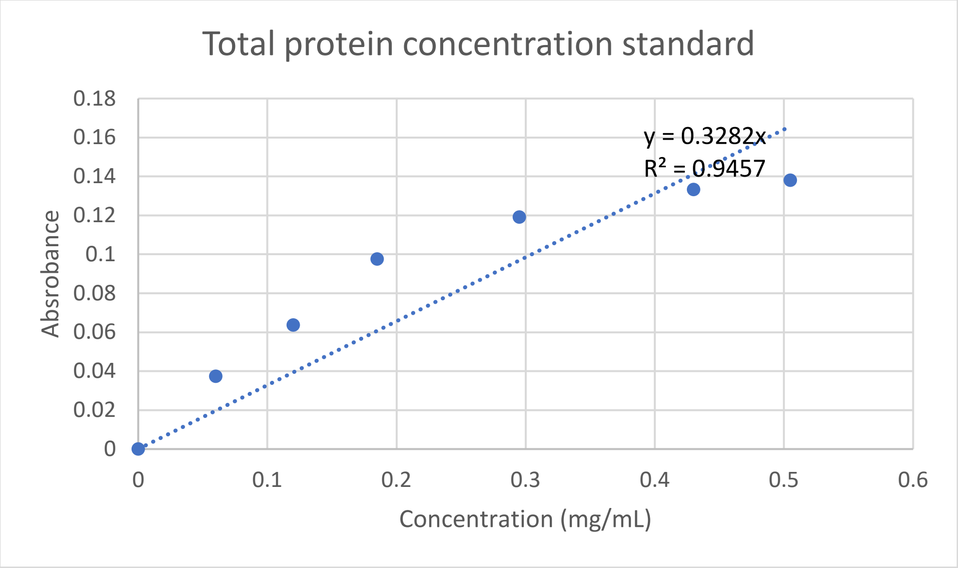

Figure S1: Protein concentration standard curve

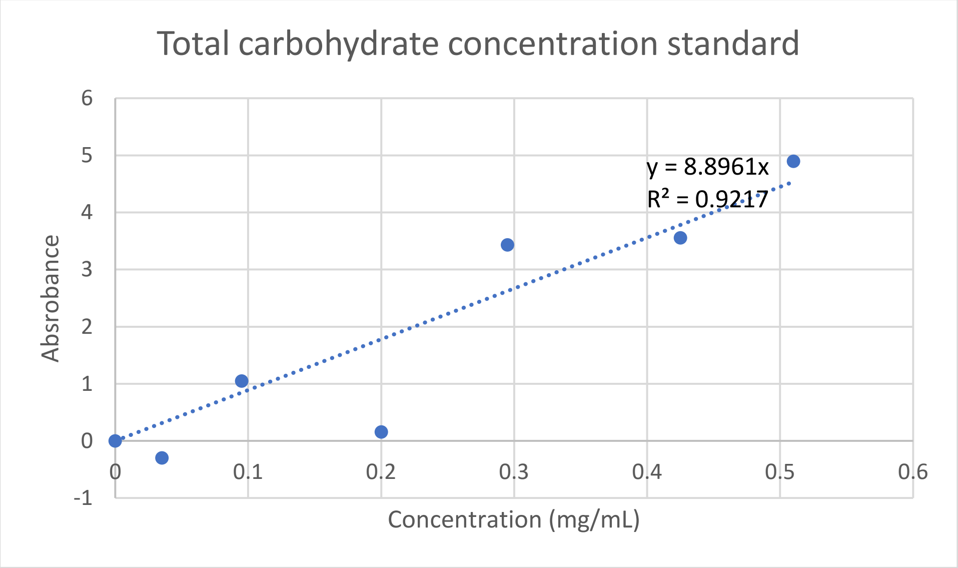

Figure S2: Carbohydrate concentration standard curve